The Dissertation Committee for Sean Michael McClure certifies that this is the approved version of the following dissertation:

Transport Mechanisms in Nanoscale Amorphous Solid Water Films

Committee:

C. Buddie Mullins, Supervisor

Thomas M. Truskett

Gyeong S. Hwang

Greg O. Sitz

Graeme Henkelman

Transport Mechanisms in Nanoscale Amorphous Solid Water Films

by

Sean Michael McClure, B.S.

Dissertation

Presented to the Faculty of the Graduate School of

The University of Texas at Austin

in Partial Fulfillment

of the Requirements

for the Degree of

Doctor of Philosophy

The University of Texas at Austin

May 2006

Dedication

To Mom, Dad, Shannon, Sarah and Jen

Acknowledgements

I would like to thank my advisor, Buddie Mullins, for giving me the opportunity to work in his research lab. In addition to being a good friend, his advice and assistance over the past five years have helped me to become a better scientist, and for that I am very thankful. I would also like to thank Dr. Tom Truskett for his involvement and genuine interest in the dissertation project. Dr. Truskett's help and guidance over the past several years have been much appreciated.

Over the course of my time in the Mullins lab I have been able to work alongside and develop friendships with some great people. During those days when experiments were not working out as planned, it was nice to have co-workers there to lighten the mood and enjoy some afternoon breaks at the Crown and Anchor. I would especially like to thank James Stiehl and Tae Kim for their help and assistance during my first years at the lab.

I would especially like to thank my Mom, Dad and family for all their love and encouragement during college, both in Iowa City and here in Austin. I couldn't have asked for better parents, and I certainly would not have been able to accomplish this without your support over the past several years. Thanks for helping me to stay positive during those times I thought things weren't going so well.

Finally, I would like to thank Jen for her love and support during my time at graduate school. I have been truly grateful for your constant support and encouragement, even during those times I was probably not much fun to be around. I love you very much.

Transport Mechanisms in Nanoscale Amorphous Solid Water Films

Publication No._____

Sean Michael McClure, Ph.D.

The University of Texas at Austin, 2006

Supervisor: Charles B. Mullins

Amorphous solid water (ASW) is a disordered, glassy form of water, which upon heating above T~135-140 K, crystallizes to cubic ice. Despite much interest and research, many properties of this glassy water phase remain contentious. Particular controversy surrounds the location of its glass transition temperature (T_g) and details regarding relaxation dynamics (viscosity, diffusivity) as water is heated and/or cooled through T_g.

In this dissertation, transport mechanisms in layered, isotopically-labeled ($H_2^{18}O$, $H_2^{16}O$) nanoscale ASW films (~ 10-100 nm) are investigated via temperature programmed desorption (TPD) techniques. ASW films are known to fracture during crystallization, presumably due to stresses generated within the film during the nucleation and growth process. This fracturing produces pathways for vapor-phase transport of desorbing molecules within the film. Translational motion of H_2O is, in all cases, observed coincident with crystallization (and hence film fracture) during heating and desorption of layered ASW films. Comparison with a *bulk* diffusion model illustrates that the observed intermixing is inconsistent with a bulk diffusion mechanism. Through

the use of hydrophobic, diffusion "barrier" layers (CCl_4, $CHCl_3$) I have been able to demonstrate that bulk diffusion in ASW is likely very small prior to crack/fracture formation.

Transport properties of dilute, glassy nitric acid films (0 - 2.2 mol % HNO_3) are also investigated. Results demonstrate that the presence of dilute amounts of HNO_3 dramatically reduce crystallization-induced film fracture. Intermixing experiments using structured films of dilute $HNO_3/H_2^{16}O$ and labeled water ($H_2^{18}O$) demonstrate that water intermixing during crystallization is substantially reduced.

Combined, the experimental results suggest that the intermixing observed in thin ASW films during crystallization is due to a porosity-mediated transport mechanism. This implies that the ASW bulk self-diffusivity near crystallization is not 'fragile' in nature, in contrast with previous results. Instead, these results suggest that ASW is likely either (i) a glass or (ii) a strong liquid prior to T~160 K. The latter case (ii) would require a change in water dynamics from its known 'fragile' behavior at higher temperatures (T~231-273 K) to 'strong' behavior at low temperatures (T<160 K).

Table of Contents

List of Tables

List of Figures

Chapter 1: Introduction

Amorphous solid water[1] (ASW), a glassy, solid form of water, has recently become the subject of intense interest and research. This has been, in large part, motivated by the applications of this material in understanding the nature and behavior supercooled liquid water.[2] It is believed that a better understanding of the nature of glassy water phases will aid in developing a complete, comprehensive picture of liquid water physics, a goal that has so far remained elusive. Though many interesting investigations[2-5] *(and references therein)* have been conducted to elucidate the properties and behavior of this substance, many fundamental questions, such as **(1)** the location of water's glass transition temperature (T_g) and **(2)** the temperature dependence of relaxation processes ("fragility") upon heating and cooling through T_g, remain unresolved. In this dissertation, I investigate the transport properties of ASW prior to crystallization (T ~ 160 K) to attempt to gain further insights into these two unresolved issues. Ahead of discussing these subjects, it serves useful to review some background regarding glassy water and why the study of relaxation processes (such as viscosity and diffusion) in glassy water phases can prove informative.

Amorphous Solid Water and Supercooled Liquid Water

When water is vapor deposited onto a cold (T < 130 K) substrate, it can form a disordered, glassy solid known as amorphous solid water (ASW).[1] Glassy water phases can also be formed via different routes, such as pressure amorphization of crystalline ice (high density amorphous, HDA)[6-7], rapid cooling of water droplets (hyperquenched glassy water, HGW) [8-9] and electron beam induced amorphization of crystalline ice

(HDA).[10-11] These glassy phases of water are metastable with respect to the corresponding crystalline phase, and when heated crystallize rapidly to form crystalline ice at temperatures near T ~ 150 - 160 K. Understanding the nature of this transition (glassy water to crystalline ice) and the relationships between this glassy phase and supercooled liquid water at higher temperatures (T ~ 230 K) has been an area of research with much controversy and many unresolved questions.

The glass transition temperature, T_g, of water has been a point of particular contention. The glass transition temperature (T_g) of a material is, generally speaking, defined as the temperature at which a material begins to exhibit molecular relaxations on an experimental timescale [i.e. when the structural relaxation time of a material becomes comparable to the experimental timescale[2]]. This characteristic time scale is usually taken to be $\tau \sim 10^2$ sec.[2,5] The molecular relaxations associated with T_g can be related to the bulk diffusivity (D) and viscosity (μ) of the material, and hence these properties can be regarded as important indicators of the glass transition and the onset of fluidity within a material. However, near T_g, typical values of the viscosity (10^{13} Poise) and diffusivity (~ 10^{-18}-10^{-20} cm^2/s) corresponding to a characteristic relaxation time of $\tau \sim 10^2$ sec, preclude direct measurement of these properties using bulk samples on reasonable timescale. [For example, with D~10^{-18}cm^2/s, an molecule would require >10^{10} years to move 1 cm]. Hence, techniques such as differential scanning calorimetry (DSC) and dielectric spectroscopy (DS) are often employed to locate the glass transition of a material, as indicated by the heat capacity change during the glass-liquid transition (in the case of DSC) and/or the dielectric loss features (in the case of DS) associated with the increased molecular motion during T_g. Fortunately, for many glassy materials, these features are clearly defined. However, in the case of glassy water, these signatures are (in the case of DSC measurements[12-23]) particularly weak and (for both DSC and DS[24-31] measurements)

are masked by rapid crystallization which occurs near T ~ 150-160 K. As a consequence, employment of these standard techniques [DSC, DS] has failed to unambiguously identify water's glass transition temperature, as interpretations of the experimental data have proven non-trivial. Despite the many alternative experimental approaches and techniques employed, interpretations of the current body of experimental work have resulted in two competing views of the location of water's glass transition. The first view is that water's glass transition is near T_g~136 K, and is supported by interpretations of data from numerous experimental studies (calorimetry studies[12-19], blunt probe measurements[32], dielectric studies[24-28], extrapolation of binary solution data[21], diffusion studies[33,34], TOF-SIMS studies[35,36]). The alternative view is that water's glass transition resides at a much higher temperature, perhaps T_g > 160 K.[22-23] This view is supported by a number of thermodynamic arguments and experimental studies (dielectric studies[29-31], isotope exchange studies[37], DSC studies/scaling arguments[20-23], soft-landed ions[38]). In this scenario (T_g > 160 K), water's glass transition would be masked by the onset of crystallization in glassy water, which occurs near 150-160 K. While the T_g~136 K value has generally been accepted as the "conventional" value of waters T_g,[2-5] the competing view (T_g > 160 K)[22-23] has not been satisfactorily proven or disproven. Since the glass transition typically signals the onset of fluidity in a material, developing a better understanding of the self-diffusivity of H_2O prior to crystallization (T ~136-160 K) could provide additional insights into this challenging problem.

If glassy water does undergo a glass-liquid transition near T_g~136 K prior to crystallization, there exists controversy surrounding the 'fragility' of the resulting liquid and how this liquid is related to supercooled liquid water at higher temperatures (T > 231 K). The "fragility" of a liquid refers to the temperature dependence of relaxation processes (and hence D and μ); the self-diffusivity of "fragile" liquids have non-

Arrhenius temperature dependencies, whereas the self diffusivity of "strong" liquids have Arrhenius temperature dependencies.[2,4,39-40] Fragility in liquids is believed to be related the cooperative nature (configurational entropy) of relaxation processes which occur in glasses/supercooled liquids upon heating/cooling. 'Strong' liquids have short- and intermediate- range structures that are relatively insensitive to temperature upon heating through T_g, whereas fragile liquids have structures which quickly disappear above T_g.[2,39,40] The configurational entropy of the supercooled liquid can be related (via Adam-Gibbs theory)[41] to transport properties such as viscosity and diffusivity. Using such relations[2], diffusivity of supercooled liquids can often be described, over large temperature ranges, using the modified Vogel-Tamman-Fulcher (VTF) equation, shown in Eq. 1.1.

$$D = D_o \, EXP \, (-B/(T-T_o)) \qquad\qquad (1.1)$$

where D_o is the diffusivity pre-exponential, T_o is related to the "ideal" glass transition[42], B is a constant. The term B is often used as a metric to compare the fragile character of various liquids.[2,4,43] The magnitude of the B term reflects the curvature of the Arrhenius plot of ln D vs. 1/T. Small values of B correspond to fragile liquids [curved Arrhenius plot]; large values of B correspond to strong liquids [straight Arrhenius plot]).

The fragility of supercooled liquid and glassy water and their connectivity remain a peculiar problem. While diffusivity[44-46], dielectric[47], and thermodynamic arguments demonstrate that supercooled liquid water is an extremely "fragile" liquid at higher temperatures (T ~ 230-273 K), the fragility of amorphous water at low temperatures remains less clear. Most experimental evidence (interpretations of dielectric

4

measurements[29,31], DSC measurements[16,48] , analysis of ASW crystallization kinetics[49]) suggests amorphous water (if it melts into a liquid after $T_g \sim 136$ K) is an extremely "strong" liquid prior to crystallization at T ~ 150-160 K.[50] If water is a "strong" liquid in this low temperature range, it would require a change in fragile-to-strong dynamics somewhere between T~160-231 K, to maintain smooth connection with high temperature (T > 231 K) diffusivity measurements[44-46]. While this behavior is consistent with recent theoretical work[51-57], thermodynamic arguments, and experiments on confined water samples[58-61], it remains controversial as this phenomenon has not been seen experimentally for a liquid. Also, additional theoretical work[62] and experimental work on sequestered water[63] are more consistent with continuous "fragile" relaxation behavior from high temperatures (T~231 K) to lower temperatures (T~160 K). Thus, competing viewpoints on this issue currently exist.

Unfortunately, direct experimental verification of this proposed fragile-to-strong transition (i.e. a study of relaxation vs. temperature of bulk supercooled liquid water from T~136 K to 273 K) is impossible with current experimental limitations. This is due to the fact that over a wide temperature range liquid water crystallizes much too rapidly to perform experiments on a reasonable timescale. This "no man's land"[64] (as it is often referred) of supercooled/glassy water is displayed in Figure 1.1. Approaching from high temperatures (T > 231 K), supercooled liquid water samples can only be cooled to a temperature of T~231 K prior to rapid crystallization; from the low temperature approach, glassy water can be heated to temperatures of T ~ 150-160 K before rapid crystallization occurs. Consequently, measurements of relaxation properties (such as diffusivity, viscosity) of supercooled and glassy water phases cannot be conducted over this temperature range at ambient pressures. Though experimentation on bulk

5
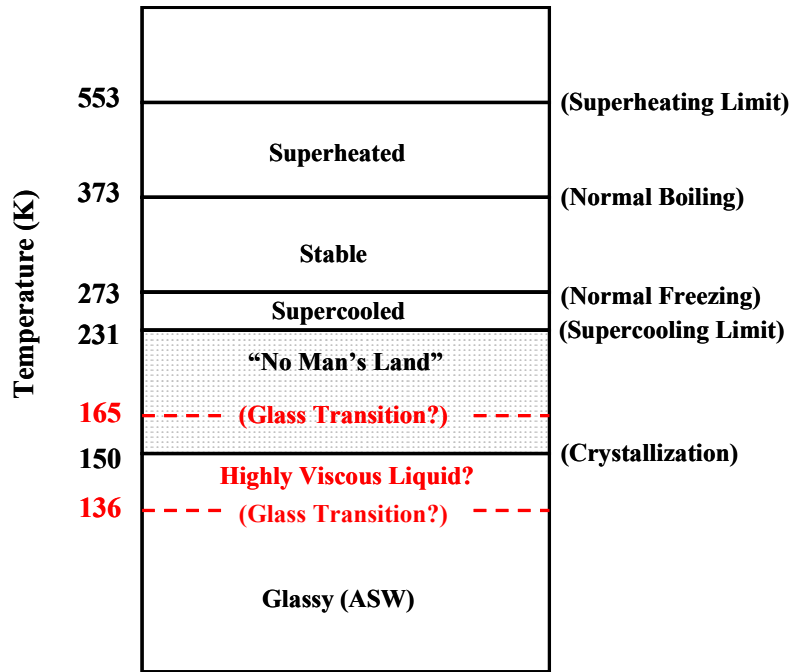
Figure 1.1. "No Man's Land" of Supercooled Liquid and Glassy Water. Displayed in Figure 1.1 is a diagram adapted from Mishima and Stanley[64] illustrating the "No Man's Land" of liquid water (shown shaded in gray). This region represents the temperature range in which experimentation on bulk supercooled water samples and glassy water samples cannot occur due to rapid crystallization. Also shown in the figure are several "accepted" (solid lines) and "unresolved" (red dotted lines) transitions in supercooled liquid/glassy water. This illustrates that fundamental aspects of low temperature glassy water behavior remain unresolved.

supercooled liquid and glassy phases have been limited to the "border" regions of this regime (T~160 K and T~231 K); understanding properties of water near these two borders can provide clues about events within the no man's land. Developing a complete understanding of the magnitude and temperature dependence of ASW *self-diffusivity* at low temperatures (between T ~ 136 - 160 K) could provide insight into the fragility of ASW at low temperatures and the postulated fragile-to-strong transition between T~160-231 K.

Nanoscale Amorphous Solid Water (ASW) Films

As the preceding section illustrated, experimental difficulties have hampered direct investigations of transport in low temperature glassy water phases. This is in large part due to the sluggish transport properties (D~10^{-18} cm^2/s, μ~10^{13} P) near T$_g$, which precludes the use of bulk glassy samples. These difficulties have prompted experimentalists to develop new, creative methods to probe the properties of glassy water. In a particularly novel approach to this problem, the Kay group[33-34,65-73] has employed temperature programmed desorption (TPD) of molecular-beam deposited, nanoscale (10-100 nm) ASW films, grown under ultra-high vacuum (UHV) conditions, to probe the properties of low temperature solid water phases. This technique, employed by the Kay group[33-34,65-73] and others[35-38,74-76], has provided great insight into the structural properties[69-75,77], thermodynamic properties[65], transport properties[33-34,37], and crystallization kinetics[66-68,76] of ASW. Of primary importance to the present study, this technique is particularly well-suited for studies of ASW transport properties, as the small dimensions of these films (10-100 nm) allow for observation of small diffusion coefficients on reasonable time scales. In a seminal study, Smith and Kay[33,34] investigated transport in ASW near crystallization T~150-157 K, by examining the intermixing between isotopically labeled (H$_2$^{18}O, H$_2$^{16}O) nanoscale films of ASW via

7

Figure 1.2. TPD Spectra and ASW Self Diffusivity Studies of Smith and Kay et. al. Shown in Figure 1.2A is a representative TPD spectra from the ASW self-diffusivity studies of Smith et. al.[33-34] In this experiment, ~32 BL (bilayers) $H_2^{18}O$ ASW was deposited (at T ~ 77 K) onto a single crystal substrate (Ru(001)), followed by deposition of ~32 BL $H_2^{16}O$ ASW (at T ~ 77 K). The sample was then heated (at a rate of 0.6 K/s) and desorbing species were monitored via QMS. The interlayer mixing which occurs near T~155 K (during crystallization of the film) was interpreted as liquid-like bulk diffusion between the layered ASW films. By employing a simple desorption-diffusion model, ASW self-diffusivity values between T~150-157 K were extracted from the data. These self-diffusivity values are shown in Figure 1.2B (open circles) along with high temperature (T > 231 K) supercooled water self-diffusivity data.[44-46] The good fit of the VTF equation (solid line) to the low and high temperature diffusivity data has been cited as evidence for liquid-like fragile nature of ASW between T ~ 150-157 K, and a T_g near 136 K.
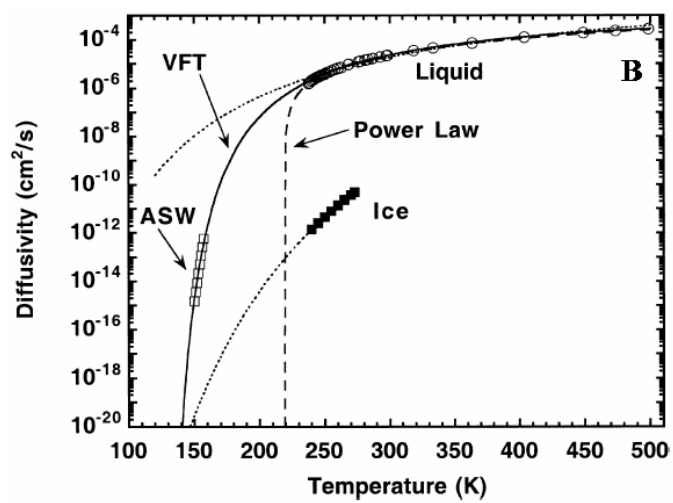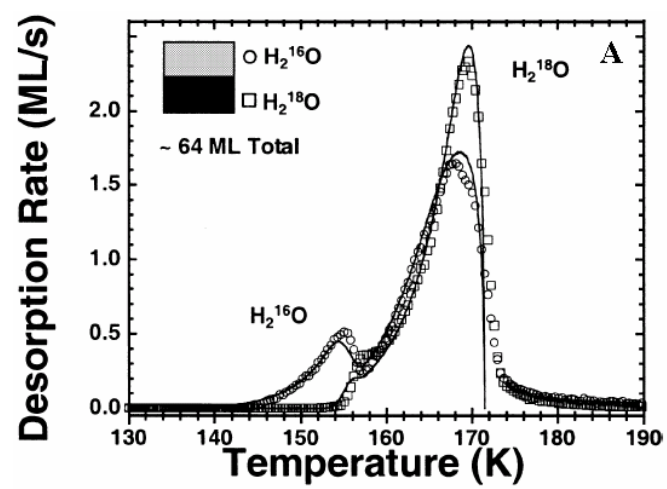
TPD. Shown in Figure 1.2A and 1.2B are selected plots from their studies[34]. In the experiment of Fig. 1.2A, ~32 BL (bilayers) $H_2^{18}O$ ASW was deposited onto a Ru(001) single crystal substrate, followed by deposition of ~32 BL $H_2^{16}O$ ASW at T ~ 77 K. (These *initially* dense, non-porous[70-71,77-79] films were deposited at T~77 K at normal incidence.) The sample was then heated (at a rate of 0.6 K/s) and desorbing species were monitored via quadrupole mass spectrometer (QMS). The spectra indicate that significant interlayer mixing occurs near T~155 K (during crystallization of the film). This substantial mixing was *interpreted* as liquid-like bulk diffusion between the layered ASW films. By employing a simple desorption-diffusion model, ASW self-diffusivity values between T~150-157 K were extracted from the data. These experimentally determined self-diffusivity values are shown in Figure 1.2B (open circles) along with high temperature (T > 231 K) supercooled water self-diffusivity data.[44-46] The good fit (Fig 1.2B) of the VTF equation (solid line) to the low temperature ASW self diffusivities (open squares) and high temperature supercooled liquid water (open circles) diffusivity data over this wide temperature range (T~150-500 K) was interpreted as strong evidence for liquid-like fragile nature of ASW near T ~ 150-157 K, and a T_g near 136 K. As will be discussed shortly, ASW films are known to exhibit significant morphological and structural changes during crystallization.

Crack and Fracture Formation in ASW Films

During crystallization of thin ASW films (150-159 K), cracks and fractures are believed to form throughout the film during the crystallization process, presumably due to stresses created within the film during crystal grain growth and grain-grain

impingement.[70,74] Numerous experimental studies performed on vapor deposited glassy water films (TPD surface area measurements[66,76,80], Kr desorption measurements[72], AFM measurements[74], TEM measurements[81], optical interferometry measurements[82-83], TPD-TOF SIMS measurements[35-36]) provide support for this hypothesis, suggesting that initially smooth ASW films exhibit significant changes in surface area and surface topology upon crystallization. Interestingly, these cracks and fractures generated within glassy water films have been shown[69,73,75] to provide high-conductance pathways for transport of trapped, volatile gases. As shown by Smith et. al., this phenomena can be probed using structured thin films of CCl_4 and ASW.[69] Figure 1.3 shows such a TPD experiment from the study of Smith et. al. In the case of Fig. 1.3A, a layered film constructed by depositing a thin layer of ASW followed by a thin layer of CCl_4 is heated at a rate of 0.6 K/s; CCl_4 multilayers desorb normally, followed by desorption of the ASW layer. In the case of Fig. 1.3B, the order of film deposition has been reversed, with CCl_4 deposited beneath the ASW thin film prior to heating. As the spectra illustrates, CCl_4 does not desorb at its' normal temperature (125-142 K), but rather remains trapped below the ASW overlayer until crystallization of the ASW ('bump' feature of the H_2O desorption spectra[65]). Once an interconnected pathway of cracks/fractures has been formed in the crystallizing film, the volatile CCl_4 multilayers are able to escape from beneath the water. This phenomena has been observed for many "volatile molecules" (such as CCl_4, Ar, N_2, O_2, etc.), illustrating the ability of these high-conductance pathways to transport molecules of varying character. In fact, this cracking and fracturing is hypothesized to be the cause of off gassing from icy interstellar bodies, such as comets, a phenomenon that has been observed by astronomers and astrophysicists.[84-91]
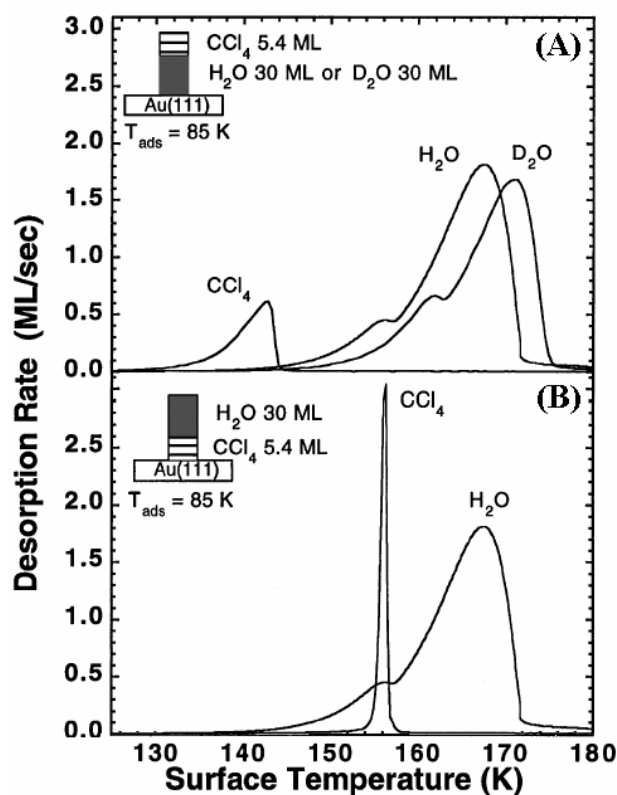
Figure 1.3. **CCl₄ "Molecular Volcano" Desorption Experiment of Smith et. al.** Figures 1.3A and 1.3B display TPD spectra from Smith et. al.[69], in which a CCl₄ film has been placed atop (Fig. 1.3A) and below (Fig. 1.3B) an ASW multilayer film prior to heating. As the spectra illustrate, when CCl₄ is placed atop the ASW film, it desorbs at its' normal temperature (T~125-142 K); when CCl₄ is placed below the ASW film, it is "trapped" until ASW crystallization ('bump'), at which point it is episodically released. This has been taken as evidence of a network of cracks/fractures which occur within the ASW film during crystallization.

While the effect of crystallization induced film-fracture on transport of a variety of molecules (such as CCl_4, Ar, N_2, O_2, etc.) has been studied, the transport of H_2O through these high-conductance pathways has not been examined as a possible mechanism for *water* transport during ASW crystallization (T~150-159 K). Since intermixing between thin, labeled ($H_2^{16}O, H_2^{18}O$) ASW films (Fig. 1.2A) occurs coincident with ASW crystallization (and hence porosity formation Fig 1.3), it is plausible that a porous transport mechanism (in contrast to a bulk diffusion mechanism) could significantly contribute to the observed isotopic mixing. While H_2O is not nearly as "volatile" as other trapped molecules (such as CCl_4) near ASW crystallization, it certainly has a non-negligible desorption rate which would allow it to desorb through an interconnected network of cracks and fracture. If transport via fracture pathways is the dominant transport mechanism for H_2O in ASW films, this would have important consequences for previous ASW self-diffusivity measurements and the resulting implications regarding ASW mobility and fragility prior to crystallization (T ~ 150-160 K).

Dissertation Overview

In this dissertation, transport phenomena in nanoscale ASW films are investigated, with particular attention to the role of porosity-mediated transport via cracks and fractures during ASW crystallization (150-160 K). All experiments are conducted using molecular beam techniques, which are employed to grow (via vapor deposition) dense/non-porous nanoscale ASW films ($H_2^{16}O$, $H_2^{18}O$) on a well-characterized Ir(111) single crystal substrate (at T ~ 77 K) under ultrahigh vacuum conditions. As stated previously, study of *nanoscale* ASW films via thermal desorption allows for study of transport processes on length scales relevant to diffusion near the glass transition (D~10^{-18}-10^{-20} cm^2/s). Quadrupole mass spectrometry (QMS) and temperature programmed

desorption (TPD) techniques are used to probe transport mechanisms within these structured films during ASW crystallization (T~150-160 K). Structured films with diffusion "barrier" layers (immiscible, hydrophobic molecules such as CCl_4, $CHCl_3$, and CH_2Cl_2) have been studied to determine the magnitude of bulk diffusion in ASW prior to crystallization. Various 'probe' molecules (CCl_4, MeOH, $CClF_2H$[80]) have been utilized to provide further insight into porosity formation, surface area changes, and diffusion barrier effectiveness.

In Chapter 2, transport in nanoscale (10-100 nm) structured films of ASW ($H_2^{16}O$, $H_2^{18}O$) and CCl_4 is investigated via thermal desorption techniques. Desorption of structured films with varying amounts (0-30 ML CCl_4) of diffusion "barrier" layers between labeled ASW layers exhibit similar mixing behavior, indicating that bulk diffusion prior to porosity formation (T~155 K) is likely negligible. Observed transport behavior is also found to be fundamentally inconsistent with a classical bulk diffusion mechanism, as determined by comparison with model calculations. Desorption experiments are also conducted with varying heating rates, illustrating that the observed translational motion within the ASW film is always concomitant with film fracture and the amorphous to crystalline phase transition. These results suggest that transport via cracks and fissures formed within the films during crystallization is the predominate mode of intermixing within ASW during crystallization (T ~ 150-160 K). We interpret these results to indicate that ASW is either a strong liquid or glass prior to 160 K, in contrast with conclusions drawn by previous investigators.[33,34]

In Chapter 3, further intermixing experiments are conducted with structured ASW films of various thicknesses at different heating rates. Isothermal desorption measurements and surface area measurements (using $CClF_2H$ probe molecule) reveal that the translational motion of labeled water molecules observed during crystallization is

14

coincident with an increase in film porosity. MeOH is used as a "water-like" probe molecule to illustrate the ability of CCl_4 barrier layers to hinder transport within structured ASW films. Investigations of abrupt CCl_4 desorption are also conducted to determine its' dependence on film thickness, film crystallization and anneal temperatures. These results illustrate parallels between observed water mixing and the onset of porosity formation within the ASW films, providing further support for the important role of a porosity mediated transport mechanism within ASW films near crystallization.

In Chapter 4, I investigate the effect of dilute amounts (0-2.2 mol %) of HNO_3 on the porosity formation in crystallizing ASW films. It is found that small amounts of HNO_3 (~0.6 mol %) are effective in reducing crack/fracture formation during crystallization as evidenced by elimination of CCl_4 "molecular" volcano desorption and film surface area measurements. The presence of HNO_3 was also found to hasten the onset of ASW crystallization (appearance of 'bump') during TPD experiments. Transport within nanoscale structured films of HNO_3 (0.6 mol %) and $H_2^{18}O$ are presented, in an effort to study intermixing in ASW films *in which crystallization-induced film fracture has been reduced*. In contrast to the pure water mixing experiments of Chapter 2 and 3, TPD mixing experiments with HNO_3-doped films show less mixing during film crystallization and show behavior more consistent with a bulk diffusion mechanism. These results again suggest that a porous transport mechanism plays an important role in the intermixing observed in nanoscale ASW films.

In Chapter 5, the major findings and implications of these studies with regards to water's T_g and fragility are summarized. Suggestions for future investigations are also presented.

15

References

1. E. F. Burton, W. F. Oliver, Proc. Roy. Soc. Lond. A. **153**, 166 (1935)

2. P. G. Debenedetti, *Metastable Liquids: Concepts and Principles* (Princeton University Press, Princeton, NJ, 1996).

3. P. G. Debenedetti, J. Phys. Cond. Matt. **15**, R1669 (2003)

4. C. A. Angell, Chem. Rev. **102**, 2627 (2002)

5. C. A. Angell, Annu. Rev. Phys. Chem. **55**, 559 (2004)

6. O. Mishima, L. D. Calvert, E. Whalley, Nature **310**, 393 (1984)

7. O. Mishima, L. D. Calvert, E. Whalley, Nature **314**, 76 (1985)

8. P. Brügeller, E. Mayer, Nature **288**, 569 (1980)

9. G. P. Johari, A. Hallbrucker, E. Mayer, Nature **330**, 552 (1987)

10. H.-G. Heide, Ultramicroscopy **14**, 271 (1984)

11. N. Sartori, J. Bednar, J. Dubochet, J. Micros. **182**, 163 (1996)

12. J. A. McMillan, S. C. Los, Nature **206**, 806 (1965)

13. M. Sugisaki, H. Suga, S. Seki, J. Chem. Soc. Jpn. **41**, 2591 (1968)

14. A. Hallbrucker, E. Mayer, G. P. Johari, J. Phys. Chem. **93**, 4986 (1989)

15. G. P. Johari, A. Hallbrucker, E. Mayer, Nature **330**, 552 (1987)

16. I. Kohl, L. Bachmann, A. Hallbrucker, E. Mayer, T. Loerting, Phys. Chem. Chem. Phys. **7**, 3210 (2005)

17. G. P. Johari, J. Chem. Phys. **119**, 2935 (2003)

18. G. P. Johari, J. Chem. Phys. B. **107**, 9063 (2003)

19. I. Kohl, L. Bachmann, E. Mayer, A. Hallbrucker, T. Loerting, Nature **435**, E1 (2005)

20. J. A. Ghormley, J. Chem. Phys. **48**, 503 (1968)

21. D. R. MacFarlane, C. A. Angell, J. Phys. Chem. **88**, 759 (1984)

22. Y. Yue, C. A. Angell, Nature **427**, 717 (2004)

23. V. Velikov, S. Borick, C. A. Angell, Science **294**, 2335 (2001)

24. G. P. Johari, J. Chem. Phys. **123**, 016102 (2005)

25. G. P. Johari, J. Chem. Phys. **122**, 144508 (2005)

26. G. P. Johari, A. Hallbrucker, E. Mayer, J. Chem. Phys. **97**, 5851, (1992)

27. G. P. Johari, A. Hallbrucker, E. Mayer, J. Chem. Phys. **95**, 2955 (1991)

28. G. P. Johari, Phys. Chem. Chem. Phys. **7**, 1091 (2005)

29. A. Minoguchi, R. Richert, C. A. Angell, J. Phys. Chem. B. **108**, 19825 (2004)

30. S. Cerveny, G. A. Schwartz, R. Bergman, J. Swenson, Phys. Rev. Lett. **93**, 245702/1 (2004)

31. A. Minoguchi, R. Richert, C. A. Angell, Phys. Rev. Lett. **93**, 215703-1 (2004)

32. G. P. Johari, J. Phys. Chem. B. **102**, 4711 (1998)

33. R. S. Smith, B. D. Kay, Nature **398**, 788 (1999)

34. R. S. Smith, Z. Dohnálek, G. A. Kimmel, K. P. Stevenson, B. D. Kay, Chem. Phys. **258**, 291 (2000)

35. R. Souda, Chem. Phys. Lett. **415**, 146 (2005)

36. R. Souda, Phys. Rev. Lett. **93**, 235502/1, (2004)

37. M. Fisher, J. P. Devlin, J. Phys. Chem. **99**, 11584 (1995)

38. A. A. Tsekouras, M. J. Iedema, J. P. Cowin, Phys. Rev. Lett. **80**, 5798 (1998)

39. C. A. Angell, Science **267**, 1924 (1995)

40. P. G. Debenedetti, F. H. Stillinger, Nature, **410**, 259 (2001)

41. G. Adam, J. H. Gibbs, J. Chem. Phys. **43**, 139 (1965)

42. W. Kauzmann, Chem. Rev. **43**, 219 (1948)

43. C. A. Angell, Science **267**, 1924 (1995)

44. K. T. Gillen, D. C. Douglass, M. J. R. Hoch, J. Chem. Phys. **57**, 5117 (1972)

45. W. S. Price, H. Ide, Y. Arata, O. Söderman, J. Phys. Chem. B. **104**, 5874 (2000)

46. H. R. Pruppacher, J. Chem. Phys. **56**, 101 (1972)

47. D. Bertolini, M. Cassettari, G. Salvetti, J. Chem. Phys. **76**, 3285 (1982)

48. K. Ito, C. T. Moynihan, C. A. Angell, Nature **398**, 492 (1999)

49. P. Jenniskens, D. F. Blake, Astro. J. **473**, 1104 (1996)

50. C. A. Angell, J. Phys. Chem. **97**, 6339 (1993)

51. P. Gallo, F. Sciortino, P. Tartaglia, S-.H. Chen, Phys. Rev. Lett. **76**, 2730 (1996)

52. F. Sciortino, P. Gallo, P. Tartaglia, H.-S. Chen, Phys. Rev. E. **54**, 6331 (1996)

53. F. W. Starr, S. Harrington, F. Sciortino, H. E. Stanley, Phys. Rev. Lett. **82**, 3629 (1999)

54. F. W. Starr, C. A. Angell, H. E. Stanley, Physica A. **323**, 51 (2003)

55. F. Sciortino, L. Fabbian, H.-S. Chen, P. Tartaglia, Phys. Rev. E. **56**, 5937 (1997)

56. F. W. Starr, F. Sciortino, H. E. Stanley, Phys. Rev. E. **60**, 6757 (1999)

57. F. W. Starr, C. A. Angell, E. La Nave, S. Sastry, F. Sciortino, H. E. Stanley, Biophys. Chem. **105**, 573 (2003)

58. A. Faraone, L. Liu, C.-Y. Mou, C.-W. Yen, S.-H. Chen, J. Chem. Phys. **121**, 10843 (2004)

59. L. Liu, S.-H. Chen, A. Faraone, C.-W. Yen, C.-Y. Mou, Phys. Rev. Lett. **95**, 117802/1 (2004)

60. R. Bergman, J. Swenson, Nature, **403**, 283 (2000)

61. J. Swenson, J. Phys. Cond. Matt. **16**, S5317 (2004)

62. D. Patschek, A. Geiger, J. Phys. Chem. B. **103**, 4139 (1999)

63. G. P. Johari, J. Chem. Phys. **105**, 7079 (1996)

64. O. Mishima, H. E. Stanley, Nature **396**, 329 (1998)

65. R. J. Speedy, P. G. Debenedetti, R. S. Smith, C. Huang, B. D. Kay, J. Chem. Phys. **105**, 240 (1996)

66. Z. Dohnálek, G. A. Kimmel, R. L. Ciolli, K. P. Stevenson, R. S. Smith, B. D. Kay, J. Chem. Phys. **112**, 5932 (2000)

67. Z. Dohnálek, Z., R. L. Ciolli, G. A. Kimmel, K. P. Stevenson, R. S. Smith, B. D. Kay, J. Chem. Phys. **110**, 5489 (1999)

68. R. S. Smith, C. Huang, E. K. L. Wong, B. D. Kay, Surf. Sci. **367**, L13 (1996)

69. R. S. Smith, C. Huang, E. K. L. Wong, B.D. Kay, Phys. Rev. Lett. **79**, 909 (1997)

70. G. A. Kimmel, K. P. Stevenson, Z. Dohnálek, R. S. Smith, B. D. Kay, J. Chem. Phys. **114**, 5284 (2001)

71. G. A. Kimmel, Z. Dohnálek, K. P. Stevenson, R. S. Smith, B. D. Kay, J. Chem. Phys. **114**, 5295 (2001)

72. G. A. Kimmel, N. G. Petrik, Z. Dohnálek, B. D. Kay, Phys. Rev. Lett. **95**, 166102/1 (2005)

73. P. Ayotte, R. S. Smith, K. P. Stevenson, G. A. Kimmel, B. D. Kay, J. Geo. Research [Planets], **106**, E12 33387 (2001)

74. J. M. K. Donev, Q. Yu, B. R. Long, R. K. Bollinger, S. C. Fain Jr., J. Chem. Phys. **123**, 044706/1 (2005)

75. J. L. Blanchard, J. T. Roberts, Langmuir **10**, 3303 (1994)

76. D. J. Safarik, R. J. Meyer, C. B. Mullins, J. Chem. Phys. **118**, 4660 (2003)

77. K. P. Stevenson, G. A. Kimmel, Z. Dohnálek, R. S. Smith, B. D. Kay, Science **283**, 1505 (1999)

78. Z. Dohnálek, G. A. Kimmel, P. Ayotte, R. S. Smith, B. D. Kay, J. Chem. Phys. **118**, 364 (2003)

79. Z. Dohnalek, G. A. Kimmel, P. Ayotte, R. S. Smith, B. D. Kay, J. Chem. Phys. **118**, 364 (2003)

80. D. J. Safarik, R. J. Meyer, C. B. Mullins, J. Vac. Sci. Technol. A. **19**, 1537 (2001)

81. P. Jenniskens, S. F. Banham, D. F. Blake, M. R. S. Mccoustra, J. Chem. Phys. **107**, 1232 (1997)

82. M. S. Westley, G. A. Baratta, R. A. Baragiola, J. Chem. Phys. **108**, 3321 (1998)

83. J. A. Ghormley, C. J. Hochanadel, Science **171**, 62 (1971)

84. P. Jenniskens, D. F. Blake, Planet. Space Sci. **44**, 711 (1996)

85. P. Jenniskens, D. F. Blake, Science **265**, 5173 (1994)

86. D. Prialnik, U. Egozi, A. Bar-nun, M. Podolak, Y. Greenzweig, Icarus, **106**, 499 (1993)

87. D. Laufer, E. Kochavi, A. Bar-Nun, Phys. Rev. B. **36**, 9219 (1987)

88. D. Prialnik, A. Bar-nun, Astron. Astrophys. **258**, L9 (1992)

89. J. J. Klinger, J. Phys. Chem. **87**, 4209 (1983)

90. A. H. Delsemme, J. Phys. Chem. **87**, 4214, (1983)

91. R. Smoluchowski, Astrophysical J. **244**, L31 (1981)

Chapter 2: Evidence that amorphous solid water below 160 K is not a fragile liquid

Introduction

Liquids cooled below their freezing point can form an amorphous solid (i.e., a glass) on experimental time scales if crystallization is avoided. Just above the glass transition temperature T_g, the diffusion coefficients of supercooled liquids generally display either Arrhenius ('strong') or non-Arrhenius ('fragile') temperature dependencies, behavior related to the nature of their relaxation processes.[1,2] Despite numerous insightful studies[3-17], there is still uncertainty about water's T_g and whether supercooled water is a strong or fragile liquid at low temperatures (T<160 K). Water crystallizes rapidly between 160 K and 230 K[1,18-20] and transport processes below 150 K are sluggish[21], making study of water's glass transition using bulk samples difficult experimentally.

Previous investigators[6,22-23] have shown the utility in employing nanoscale films of ASW, grown via molecular beam under UHV conditions, to gain insight into the nature of ASW prior to crystallization to crystalline ice. Recent temperature-programmed desorption experiments[6] have detected self-mixing in thin isotopically-labeled, amorphous solid water (ASW) layers near 150 K. Interpreted as bulk diffusion of a fragile liquid, this observed mixing in ASW films prior to crystallization has also provided convincing support for the conventional estimate of water's T_g (136 K).[6] In Chapter 2, temperature programmed desorption (TPD) of nanoscale ASW ($H_2^{18}O$, $H_2^{16}O$) and CCl_4 films has been used to investigate transport mechanisms in ASW. Using nanoscale CCl_4 films as "diffusion barrier" layers, our results illustrate that the mixing

observed in thin ASW films is primarily due to transport through an interconnected porous network created in the film upon crystallization. Our findings demonstrate that the self-diffusivity of water between T = 150-160 K is significantly smaller than previously thought[6,22], thus indicating that water undergoes either a glass transition or a fragile-to-strong transition at a temperature above 160 K.

Results and Discussion

Nano-structured films of ASW ($H_2^{18}O$, $H_2^{16}O$) and CCl_4 were vapor-deposited at normal incidence on an Ir(111) single crystal sample held at T ~ 77 K in ultrahigh vacuum using quasi-effusive molecular beams.[24] Investigations in our laboratory[24] and by other scientists[25,26] have demonstrated that water deposition under these conditions produces dense, nonporous ASW films. Sample temperature is measured via a thermocouple welded to the bottom edge of the Ir(111) substrate [No appreciable temperature gradients are expected to occur across the deposited ASW films]. Figure 2.1 shows TPD spectra (desorption rate versus temperature) for several such films. The spectra were acquired using a quadrupole mass spectrometer (QMS) to measure the partial pressure of the desorbing species as the substrate was heated at a rate of 0.6 K/s. Figure 2.1(a) shows spectra from a layered structure consisting of 30 BL $H_2^{16}O$ ASW on top of 30 BL $H_2^{18}O$ ASW (one BL_{H_2O} (bilayer of water) ~ 1 x 10^{15} molecules/cm^2). These results are in agreement with data from similar investigations conducted by Smith and Kay[6,22], who interpreted the intermixing as due to liquid-state diffusion. However, upon closer inspection, neither our experimental data nor the data of Smith and Kay[6] are consistent with a bulk diffusion mechanism. This inconsistency is illustrated in the inset to Figure 2.1(a), which shows the ratio of desorption rates, r_{18}/r_{16}, determined from the TPD mixing data of Fig. 2.1(a) and the same ratio calculated from a simple diffusion model. The quantity r_{18}/r_{16} can be viewed as an instantaneous measure of the relative

Figure 2.1. ASW TPD mixing experiments with different structured films composed of labeled ASW and CCl₄. For Figure 2.1(a) 30 BL of $H_2^{18}O$ (bold blue) deposited first followed by 30 BL of $H_2^{16}O$ (black); Figure 2.1(b), 30 BL of $H_2^{18}O$ (bold blue) deposited first, then 5 ML of CCl₄ (dashed red) and finally 30 BL of $H_2^{16}O$ (black); Figure 2.1(c), 30 BL of $H_2^{18}O$ (bold blue) deposited first, followed by 30 ML of CCl₄ (dashed red) and then 30 BL of $H_2^{16}O$ (black). The layered structures constructed for each experiment are depicted in the schematics (not-to-scale) shown in the lower left of each panel. For films in Fig. 2.1(a)-(c), molecular beams were employed that provided uniform coverage to the Ir(111) sample. All films in the figure and insets were heated at a ramp rate of 0.6 K/s. Exposure rates, F, were: F_{CCl_4} ~ 0.05 ML/s; F_{H_2O} ~ 0.17 BL/s.

Figure 2.1(a) Inset. Ratio of desorption rates of $H_2^{18}O$ to $H_2^{16}O$ (denoted as r_{18}/r_{16}) calculated from the TPD mixing experiment (open circles) shown in Figure 2.1(a) and r_{18}/r_{16} calculated using a simple desorption/diffusion model (black lines) to describe mixing between the two films. The model simulates mixing behavior of TPD experiments using extrapolated CI bulk diffusion parameters[29], ASW crystallization parameters[30], and ASW "bulk" diffusion coefficients[6] of varying magnitudes ("high" diffusivity to "low" diffusivity). The purpose of the model calculation traces is to qualitatively illustrate that, regardless of the magnitude of the diffusion coefficient; the experimentally observed non-monotonic behavior is inconsistent with a bulk diffusion mechanism.

Figure 2.1(b) Inset. CCl$_4$ "molecular volcano^{23}". TPD experiments are displayed for two different film structures composed of CCl$_4$ and ASW (H$_2^{16}$O). In depositing the ASW films (H$_2^{16}$O), a molecular beam was employed that provided uniform coverage over one face of the Ir(111) sample; for CCl$_4$, a different beam was used yielding a smaller deposition "spot" on the sample (~ 70% of the face area, located in the middle). In case (i) 5 ML of CCl$_4$ (green) is deposited on top of 30 BL H$_2^{16}$O ASW (bold black) [see schematic]. In case (ii) 5 ML CCl$_4$ (dashed purple) (signal x 0.5) is first deposited followed by a 30 BL H$_2^{16}$O ASW (bold black) to cover the CCl$_4$ [see schematic]. For both experiments (i) and (ii), the H$_2^{16}$O desorption spectra are identical.
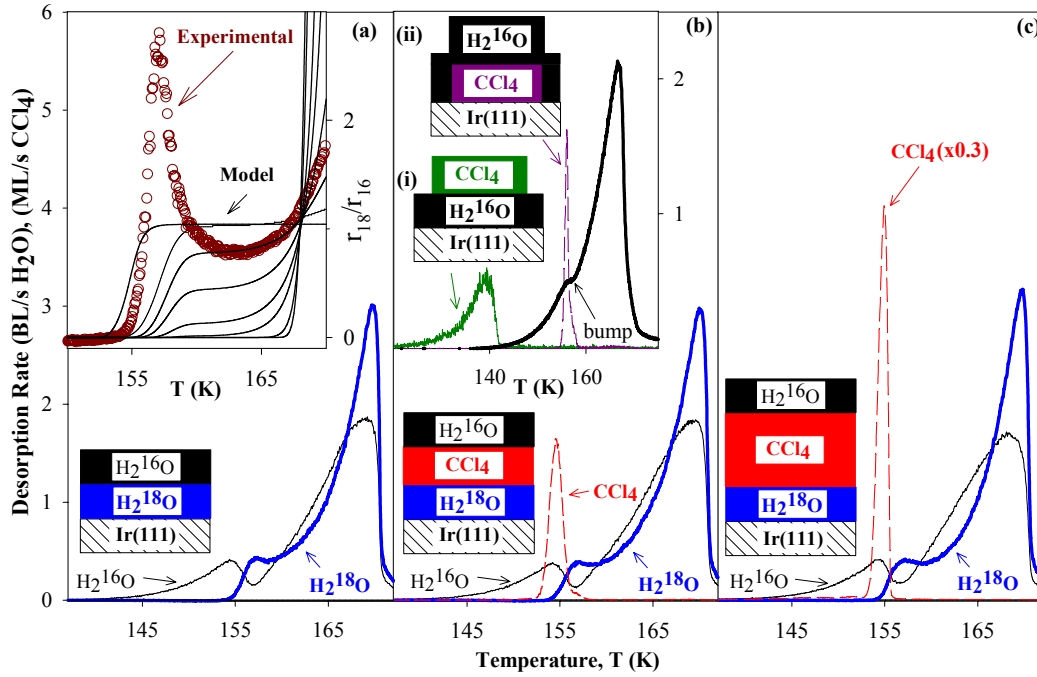
24

surface concentrations of the isotopically labeled water molecules. If bulk diffusion were the dominant mode of transport, r_{18}/r_{16} would necessarily increase monotonically upon heating (as shown by the model calculations), reflecting the increase in the $H_2^{18}O$ surface concentration as it diffuses toward the top of the film. The experimental desorption ratio r_{18}/r_{16} instead increases sharply at $T \sim 155$ K, peaks, decreases rapidly, and then increases again prior to complete desorption of the water film at $T \sim 170$ K. The desorption ratio (r_{18}/r_{16}) determined from the data of Smith and Kay[6,22] (not shown here) shows behavior similar to that shown in the inset to Fig. 2.1(a). Thus, both sets of experimental data are inconsistent with a bulk diffusion mechanism and suggest that another mode of transport dominates.

The initial intermixing (onset of $H_2^{18}O$ desorption) observed in Fig. 2.1(a) near 155 K is concurrent with crystallization of the ASW film. Crystallization is manifested as a "bump" in the water TPD spectra for a single isotope, as shown in the inset to Fig. 2.1(b).[11] This "bump" is caused by the conversion of ASW, which has a high desorption rate, to crystalline ice, which has a lower desorption rate.[11,27] Crystallization has been shown to fracture ASW, creating an interconnected porous network within the film.[23] The fracturing of the film upon crystallization is demonstrated in the Fig. 2.1(b) inset, which shows a CCl_4 "molecular volcano[23]" experiment conducted in our laboratory. Spectra (i) shows desorption of ~5 ML CCl_4 deposited *on top* of 30 BL ASW; CCl_4 (green) desorbs freely from $T \sim 120$ K - 142 K. Spectra (ii) shows desorption of ~ 5 ML CCl_4 that is completely covered by 30 BL ASW; CCl_4 (dashed purple) remains trapped under the ASW until crystallization ("bump"), when interconnected pores form and allow the CCl_4 to rapidly escape.[23] Additional measurements performed in our laboratory show significant increases in apparent surface area of the film during crystallization.[24] This

25

suggests that the onset of water intermixing observed in Fig. 2.1(a) is related to crystallization-induced porosity formation.

Figures 2.1(b) and 2.1(c), show TPD mixing experiments similar to that of Fig. 2.1(a) except that hydrophobic, immiscible CCl_4 "barrier" layers are deposited between the labeled ASW layers. The CCl_4 serves as both a "marker" for interconnected porous network formation and should serve as an impediment to water self-diffusion. Figure 2.1(b) shows a TPD experiment of a layered film of 30 BL $H_2^{18}O$ (bottom) / 5 ML CCl_4 (middle) / 30 BL $H_2^{16}O$ (top) [see schematic in Fig. 2.1(b)] which is *quantitatively* similar to the TPD spectra of Fig 2.1(a), *without a CCl₄ barrier layer*. The similarity of the water self-mixing behavior between these two spectra is inconsistent with bulk diffusion between two dense phases. If bulk diffusion were a dominant transport mechanism at temperatures less than 154 K, the 5ML CCl_4 layer should detectably hinder transport of the underlying $H_2^{18}O$ layer. Figure 2.1(c) shows an equivalent TPD experiment of a layered film of 30 BL $H_2^{18}O$ (bottom) / 30 ML CCl_4 (middle) / 30 BL $H_2^{16}O$ (top) [see schematic in Fig. 2.1(c)]. This data, involving a much thicker CCl_4 barrier layer through which diffusive mixing would seem highly unlikely, still shows similar behavior to both the non-barrier mixing experiment (Fig 2.1(a)) and the 5ML CCl_4 barrier experiment (Fig 2.1(b)). While small quantitative differences between Fig 2.1(c) and Figs 2.1(a),(b) are observed after the formation of porosity within the film, these subtle differences are likely due to effects of the abrupt CCl_4 desorption on film porosity formation. In all cases, desorption of the underlying $H_2^{18}O$ is concurrent with crystallization and, hence, the onset of interconnected pore formation within the ASW, as evidenced by the simultaneous evolution of CCl_4.

Figure 2.2. ASW mixing experiments employing different TPD heating rates. ASW mixing experiments employing different TPD heating rates [(a) 0.05 K/s; (b) 0.6 K/s; (c) 2 K/s] to control the rate of porosity creation within the ASW films. For each experiment, identical structured films of labeled ASW and CCl_4 were deposited on the Ir(111) surface held at 77 K in the following manner: 30 BL of $H_2^{18}O$ (bold blue) deposited first, then 6 ML of CCl_4 (dashed red) and finally 30 BL of $H_2^{16}O$ (black) was grown. In depositing the two ASW films, a molecular beam was employed that provided uniform coverage of one face of the Ir(111) disk-shaped sample; for the CCl_4, a different molecular beam was used which yielded a smaller deposition "spot" (~ 70% of the face area, located in the middle). This layered structure is depicted in the schematic (not-to-scale) shown in Fig. 2(c). Here, CCl_4 simply serves as a marker for the onset of porosity creation in the ASW films as discussed in the text and illustrated in the Fig. 2.1(b) inset (molecular volcano[23]). For more accurate temperature control, the experiment in Fig 2.2(a) [0.05 K/s ramp rate] was rapidly heated to 130 K at ~1 K/s, followed by heating at 0.05 K/s to 200 K. Similar experiments without CCl_4 layers yielded identical water desorption spectra.

27
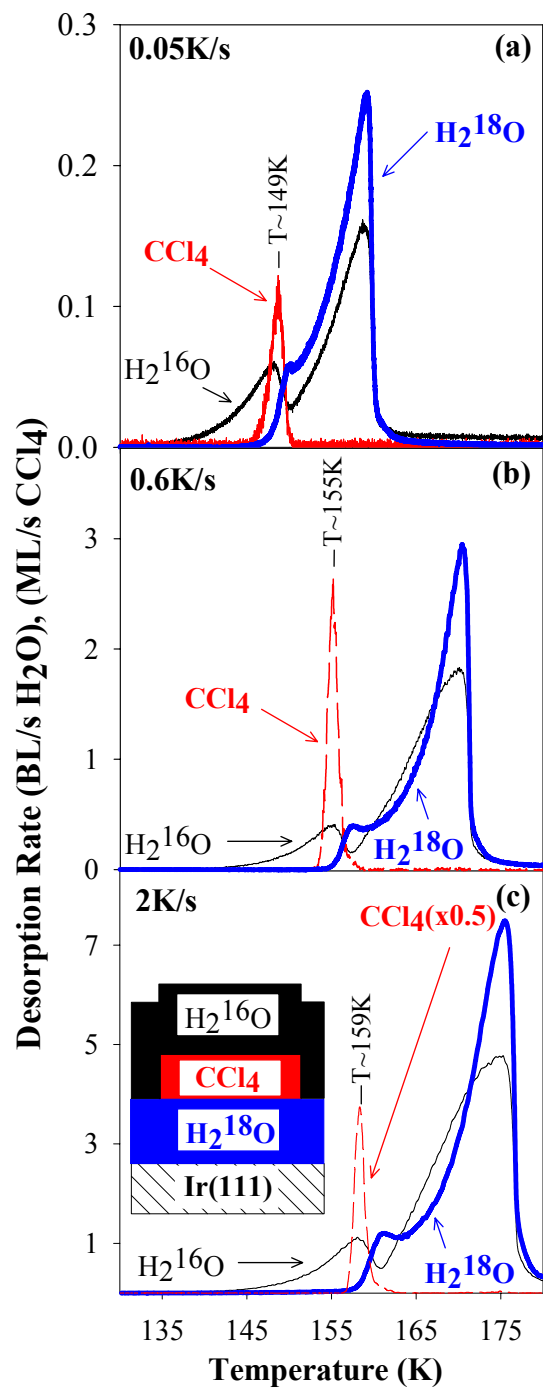
Finally, altering the TPD temperature ramp rate changes the rate of ASW crystallization, thereby allowing control over the onset of film porosity. CCl_4 Figures 2.2(a)-(c) show TPD mixing spectra of identical layered films, composed by first depositing 30 BL $H_2^{18}O$, then growth of 6 ML CCl_4, followed by deposition of 30 BL $H_2^{16}O$ [see schematic in Fig. 2.2(c)], heated at different rates (0.05 K/s, 0.6 K/s, and 2 K/s). Again, CCl_4 placed between the ASW layers acts as a "marker" for the onset of crystallization induced porosity (similar experiments without CCl_4 layers yield identical water desorption spectra). Altering the TPD heating rate changes the CCl_4 molecular volcano desorption temperature from T ~ 149 K at a ramp rate of 0.05 K/s to T ~ 159 K for a heating rate of 2 K/s. If, as we propose, transport is occurring via an interconnected porous network, altering the TPD heating rate should also shift the onset of water mixing similarly, with the appearance of $H_2^{18}O$ in the spectra occurring nearly coincident with the CCl_4 molecular volcano desorption feature and, indeed, this is observed. The ASW "liquid-like" diffusion coefficient D determined by Smith and Kay[6] changes by over three orders of magnitude from T~149 K ($\sim 7x10^{-17}$ cm^2/s) to T~159 K ($\sim 4x10^{-13}$ cm^2/s). If mixing were due to bulk diffusion, altering the TPD heating rate in this manner would change the effective length scale (L) of mixing within the ASW films by roughly an order of magnitude (using $D \sim L^2/t$; where t is time). Thus, we would expect (and do observe in model TPD calculations not shown) dramatic differences in the mixing behavior as a function of TPD heating rate, if the observed mixing is dominated by bulk diffusion. However, Figures 2.2(a)-(c) show similar mixing for each heating rate, further illustrating that the observed mixing is inconsistent with bulk diffusion. Similar to the spectra displayed in Figures 2.2(a)-(c), additional TPD mixing experiments (not shown) conducted with thicker ASW films (60 BL $H_2^{16}O$ on 60 BL $H_2^{18}O$ and 90 BL $H_2^{16}O$ on 90 BL $H_2^{18}O$) exhibit the onset of mixing coincident with the onset of porosity formation

(abrupt CCl_4 desorption). However, the overall mixing becomes less complete with increasing film thickness, consistent with a vapor-phase porous transport picture.

We envision that, prior to crystallization, there is negligible bulk diffusive motion occurring between the isotopically labeled ASW layers. However, upon creation of porosity within the crystallizing ASW film, vapor-phase water molecules are able to move through the interconnected porous network with concomitant adsorption and desorption from pore surfaces. Unlike CCl_4, which is far above its normal desorption temperature by the onset of porosity, the H_2O traveling through this porous network will have a substantial residence times on pore surfaces, owing to its lower volatility. It has been previously shown[24] that the interconnected porous network formed during crystallization can sinter and densify as the crystallizing ASW film is further annealed. Thus, we envision that as these fracture/porous pathways sinter closed[24], the water that is being transported through the interconnected porous network will become trapped within this densifying film. This "trapping" of vapor phase ASW gives rise to the apparent mixing observed in the desorption spectra after T~160K. Thus, in this picture, the transport of water will be both a function of H_2O desorption rate and surface residence time, the pore formation/sintering rate[24], and pore length/geometry within ASW films. Hence, a porous transport mechanism is consistent with both the rapid mixing observed during crystallization and the subsequent "trapped-in" mixing observed after T~160K.

Conclusions

In summary, our results illustrate that the self-mixing that has been observed in nanoscale ASW films, both here and by previous investigators[6,22], is irreconcilable with a bulk diffusion mechanism, as evidenced by (a) the fundamental inconsistency of the ratio (r_{18}/r_{16}) of experimental $H_2^{18}O$ and $H_2^{16}O$ desorption rates with a bulk diffusion mechanism (Fig. 2.1(a) inset); (b) the similarity of TPD mixing spectra of layered films

both *without* (Fig. 2.1(a)) and *with* (Figs. 2.1(b) and 2.1(c)) CCl$_4$ diffusion barrier layers; and (c) the similarity between TPD mixing spectra obtained at different TPD heating rates (Figs. 2.2(a)-(c)). Alternatively, we propose a *porous* transport mechanism (via a crystallization induced interconnected porous network) to explain the experimentally observed mixing. This mechanism is consistent with the desorption data and would explain why mixing is always concurrent with the onset of pore formation.

These results have important implications for understanding the behavior of supercooled water and its glass transition temperature. Since porous vapor-phase transport, rather than bulk diffusion, appears to be the principal mode of mobility in nanoscale ASW films, the actual self-diffusion coefficient of amorphous water in the temperature range T ~ 150 K – 160 K is significantly smaller than previously thought.[6,22] This is consistent with ASW being either a glass or a strong liquid with very low mobility under these conditions. Moreover, if ASW is indeed thermodynamically connected to liquid water at higher temperatures[11], there are only two plausible scenarios consistent with the experimental results. Either water's glass transition temperature is much higher (T$_g$ > 160 K)[3,15-16] than the conventional estimate of 136 K or liquid water undergoes a fragile-to-strong transition[2-3,28] between T ~ 160K - 230 K.

References

1.   C. A. Angell, Chem. Rev. **102**, 2627 (2002)

2.   C. A. Angell, Science **267**, 1924 (1995)

3.   A. Minoguchi, R. Richert, C. A. Angell, Phys. Rev. Lett. **93**, 215703/1 (2004)

4.   M. Fisher, J. P. Devlin, J. Phys. Chem. **99**, 11584 (1995)

5.   D.R. MacFarlane, C. A. Angell, J. Phys. Chem. **88**, 759 (1984)

6.   R. S. Smith, B. D. Kay, Nature **398**, 788 (1999)

7.   A. A. Tsekouras, M. J. Iedema, J. P. Cowin, Phys. Rev. Lett. **80**, 5798 (1998)

8. P. Jenniskens, S. F. Banham, D. F. Blake, M. R. S. Mccoustra, J. Chem. Phys. **107**, 1232 (1997)

9. G. P. Johari, J. Phys. Chem. B. **102**, 4711 (1998)

10. R. Souda, Phys. Rev. Lett. **93**, 235502/1 (2004)

11. R. J. Speedy, P. G. Debenedetti, R. S. Smith, C. Huang, B. D. Kay, J. Chem. Phys. **105**, 240 (1996)

12. G. P. Johari, J. Chem. Phys. **105**, 7079 (1996)

13. J. A. Ghormley, J. Chem. Phys. **48**, 503 (1968)

14. G. P. Johari, A. Hallbrucker, E. Mayer. Nature **330**, 552-553 (1987)

15. Y. Yue, C. A. Angell, Nature **427**, 717 (2004)

16. V. Velikov, S. Borick, C. A. Angell, Science **294**, 2335 (2001)

17. J. A. McMillan, S. C. Los, Nature **206**, 806 (1965)

18. O. Mishima, H. E. Stanley, Nature **396**, 329 (1998)

19. P. G. Debenedetti, J. Phys.: Cond. Matt. **15**, R1669 (2003)

20. C. A. Angell, Annu. Rev. Phys. Chem. **55**, 559 (2004)

21. D. E. Brown, S. M. George, J. Phys. Chem. **100**, 15460 (1996)

22. R. S. Smith, Z. Dohnálek, G. A. Kimmel, K. P. Stevenson, B. D. Kay, Chem. Phys. **258**, 291 (2000)

23. R. S. Smith, C. Huang, E. K. L. Wong, B. D. Kay, Phys. Rev. Lett. **79**, 909 (1997)

24. D. J. Safarik, R. J. Meyer, C. B. Mullins, J. Chem. Phys. **118**, 4660 (2003)

25. K. P. Stevenson, G. A. Kimmel, Z. Dohnálek, R. S. Smith, B. D. Kay, Science **283**, 1505 (1999)

26. M. S. Westley, G. A. Baratta, R. A. Baragiola, J. Chem. Phys. **108**, 3321 (1998)

27. N. J. Sack, R. A. Baragiola, Phys. Rev. B.: Cond. Matt. **48**, 9973 (1993)

28. K. Ito, C. T. Moynihan, C. A. Angell, Nature **398**, 495 (1999)

29. K. Goto, T. Hondoh, A. Higashi, Jpn J. Appl. Phys. **25**, 351 (1986)

30. Z. Dohnálek, G. A. Kimmel, R. L. Ciolli, K. P. Stevenson, R. S. Smith, B. D. Kay, J. Chem. Phys. **112**, 5932 (2000)

Chapter 3: Transport Mechanisms in Nanoscale Amorphous Solid Water Films

Introduction

Conclusively determining the glass transition temperature, T_g, of water and its fragility at low temperatures (T < 160 K) is believed to be key in developing a clear picture of the behavior and nature of liquid water.[1-4] Progress towards this goal has been hampered by the difficulty in probing the properties of water above the homogeneous nucleation temperature of glassy water (T ~ 160 K) and below the supercooling limit of the liquid (T ~ 231 K), a "no-man's land"[5] where water crystallizes very rapidly on experimental timescales. Below 160 K, transport properties (such as viscosity (μ) and diffusivity (D)), often used to characterize fragility[2-3,6-7] in liquids, are too small to be probed experimentally using bulk samples. Thus, despite much attention and many novel experimental and theoretical investigations[1-4 (and references therein)], the nature of amorphous water in the range of T~150 - 160 K remains the subject of controversy.

The glass transition temperature, T_g, of amorphous water remains a particular point of contention, with many careful analyses and interpretations of experimental data (conducted on various forms of glassy water; hyperquenched glassy water (HGW), vapor deposited amorphous solid water (ASW)[8], pressure amorphized water, and confined water) leading to differing conclusions. Some interpretations are consistent with a glass transition temperature near T_g ~ 136 K (calorimetry studies[9-17], blunt probe measurements[18], dielectric studies[19-23], extrapolation of binary solution data[3,24], diffusion studies[25,26], TOF-SIMS studies[27,28]). Other experiments (dielectric studies[29-31], isotope exchange studies[32], DSC studies/scaling arguments[24,33-36], soft-landed ions[37]) suggest that fluidity typically associated with the glass transition may not occur at T~136 K, but

rather at a higher temperature $(T_g > 160\text{-}165$ K)[34,35]. In the latter case, observation of water's T_g would be masked by glassy water crystallization upon heating near T $\sim$ 150 K. While the "conventional" assignment of water's glass transition temperature is $T_g \sim$ 136 K (as much experimental evidence suggests), this assignment has not been fully resolved and contradicting interpretations have not yet been fully disproven.

If the glass transition temperature of water indeed occurs near $T_g \sim$ 136 K, there exists controversy regarding the fragility of the liquid near T_g. Liquid fragility can be used to classify and characterize the temperature dependencies of relaxation processes (and hence, μ and D) in liquids.[2,3,6,7] 'Strong' liquids exhibit Arrhenius temperature dependencies, whereas 'fragile' liquids exhibit non-Arrhenius temperature dependencies. [2,3,6,7] Fragility in liquids is believed to be related to the cooperative nature of relaxation processes which occur in glasses/supercooled liquids upon heating/cooling. While supercooled liquid water is known to be one of the most fragile liquids at higher temperatures (T > 231 K) as suggested by dielectric[38], self-diffusivity[39-41], and thermodynamic arguments[42], the nature of amorphous water at lower temperatures (T < 160 K) remains an open question. For water to have a glass transition temperature of T_g $\sim$ 136 K, its diffusivity at this temperature should lie near D $\sim$ 10^{-18} cm^2/s (a characteristic diffusivity at T_g). For water to be considered a 'fragile' liquid at these low temperatures, the temperature dependence of the diffusion coefficient should be non Arrhenius, and would likely be highly activated near T $\sim$ 150-160 K while maintaining a smooth connection with higher temperature supercooled liquid water diffusivities. If water is a 'strong' liquid prior to crystallization at T$\sim$160 K, the diffusivity will exhibit an Arrhenius temperature dependence, while maintaining D $\sim$ 10^{-18} cm^2/s near T_g $\sim$ 136K.

Arguments based on DSC measurements of amorphous water[13,42-43], dielectric measurements of amorphous water[29,31] and crystallization kinetics[44] have been interpreted

35

as evidence that liquid water may be a 'strong' liquid at lower temperatures.[24,43] Given liquid water's known behavior above T~230 K, this scenario would require a fragile-to-strong transition[42] in the diffusivity behavior of water between the temperatures of T ~ 160 - 230 K. While fragile-to-strong behavior is not common for liquids, theoretical studies of water[45-52] [and of other network forming liquids (SiO_2[53], BeF_2[54])], are consistent with transitions from fragile dynamics at higher temperatures to strong dynamics at lower temperatures. Recent experimental neutron scattering studies[55-56] and dielectric studies[57-58] of confined water have also been offered as possible evidence consistent with this scenario.

Conversely, recent temperature programmed desorption experiments by Smith and Kay[25,26] have detected intermixing in thin, isotopically-labeled ASW films near T ~ 150 K. In this creative experimental approach, structured films of labeled water ($H_2^{16}O$, $H_2^{18}O$) were deposited at 77 K on a substrate and were heated, with desorbing species monitored via mass spectrometry, to check for evidence of molecular diffusion above water's conventional T_g (136 K) and prior to crystallization. The observed intermixing which appears near ASW crystallization has been interpreted as bulk diffusion, and has been cited as evidence for the continuous liquid-like, 'fragile' (non-Arrhenius) nature of water diffusivity (described well using the Vogel-Fulcher-Tamman (VFT) equation). Simulations by Paschek and Geiger[59] are also consistent with this picture, along with dielectric studies of sequestered water[60]. However, additional experimental evidence supporting the existence *or* non-existence of a strong-to-fragile transition in the "no man's land"[5] region of water would prove valuable in understanding the behavior of water in this temperature region of the water phase diagram. Hence, the importance of understanding the magnitude of self-diffusivity in amorphous water prior to crystallization at T ~ 150 - 160 K becomes apparent.

While the preceding discussion was by no means exhaustive (for excellent reviews of experimental/theoretical work the reader is referred to Refs. 1-4), it does serve useful to highlight that, despite many novel experimental and theoretical studies, issues still remain unresolved regarding water's T_g and fragility at low temperatures. In the present chapter, we have chosen to focus on translational motion of water molecules in vapor-deposited ASW near T~160 K in the hopes of providing some further insights and data regarding water diffusion in the temperature range T~ 150-160 K. In Chapter 2, we presented results which indicated that the intermixing observed during the temperature programmed desorption (TPD) of nanoscale, structured ASW films between (T ~ 150-157 K) is inconsistent with a bulk diffusion mechanism. Rather, the substantial mixing observed is primarily due to transport of H_2O through an interconnected porous network developed within the ASW film during crystallization. These new results suggest that self-diffusivity of ASW in the range 150 - 157 K is much smaller than previously thought[25,26], making it unlikely that ASW is a fragile liquid prior to crystallization at 150K. Instead, water either remains a *(i)* rigid glass until T_g ~ 160 -165 K, or *(ii)* is a 'strong' liquid with T_g ~ 136 K, undergoing a fragile-to-strong transition between T ~ 160 - 230 K in order to a maintain connection with liquid water diffusivities[39-41] at higher temperatures. In Chapter 3, we present additional TPD and surface area measurements to further explore transport mechanisms in nanoscale ASW films. Experiments were also conducted using methanol as a diffusion 'probe' molecule to illustrate the effectiveness of CCl_4 diffusion 'barrier' layers used in our experiments. This data provides further experimental support for our conclusions; namely, that the mixing observed during crystallization of ASW films between (T~150-160 K) is primarily due to transport through cracks/fractures occurring in the film in this temperature range, and not due to

37

bulk diffusion. Thus, we conclude that ASW is not a fragile liquid and, rather, it is most likely either a strong liquid or a rigid glass below 160 K.

Experimental

We have employed temperature programmed desorption (TPD) measurements of structured nanoscale films of isotopically-labeled ASW ($H_2^{18}O$, $H_2^{16}O$), CCl_4, and MeOH to investigate transport mechanisms in amorphous solid water films.   All experiments were conducted in a molecular beam apparatus described previously.[61] Briefly, this apparatus consists of an ultrahigh vacuum (UHV)/surface analysis chamber and a separable beam source chamber containing two molecular beam lines.[61] One set of molecular beam apertures creates a beam spot (beam spot diameter ~9.1 mm) larger than the sample (entire sample in "umbra" region), providing a uniform flux across the entire sample area.[62] The second molecular beam creates a beam spot (beam spot diameter ~6.5 mm) contained entirely within the sample area, minimizing exposure to other surfaces of the UHV chamber. The UHV/surface analysis chamber (P_{base}~1×10^{-10} Torr) is equipped with a quadrupole mass spectrometer (QMS), Auger electron spectroscopy (AES), and low energy electron diffraction (LEED) optics. An Ir(111) single crystal (circular in shape; diameter~ 9.1 mm) was used as a substrate for film growth. The iridium substrate can be cooled to T ~ 77 K via contact with a liquid nitrogen reservoir and can be heated resistively to T ~ 1550 K to conduct TPD experiments. We expect no appreciable temperature gradients to occur across the deposited ASW films during desorption and/or crystallization, based on our sample thickness and estimates of glassy water thermal conductivity.[63] The Ir(111) single crystal was initially cleaned and ordered via repeated Ar ion sputtering (1 keV; P_{Ar} ~ 1×10^{-5} Torr), O_2 anneal cycles (600 K, P_{O_2} ~ 5×10^{-7} Torr), and in vacuo anneal cycles (1400 K). Surface order and cleanliness were verified via LEED and AES.   After this initial cleaning/ordering procedure, the Ir(111) substrate was

38

cleaned prior to each TPD experiment with O_2 adsorption/desorption cycles, with annealing cycles to order the substrate when necessary.

Nanoscale structures of isotopically labeled ($H_2^{18}O$ and $H_2^{16}O$) ASW films were grown on the Ir(111) substrate at 77 K and normal incidence using room temperature, quasi-effusive molecular beams of pure water vapor. Growth under these conditions has been shown to produce smooth, dense, non-porous films of ASW.[64-68] All ASW ($H_2^{16}O$, $H_2^{18}O$) films were grown with a beam flux of ~0.17 bilayers/sec (BL/s) (One BL_{H_2O}~1x10^{-15} molecules/cm^2)[69,70] and a beam spot which provides a uniform flux of water across the entire Ir(111) substrate. In many cases, layered films of isotopically labeled ASW were grown sequentially on the Ir(111) sample which were subsequently heated while simultaneously monitoring the desorbing species ($H_2^{18}O$, $H_2^{16}O$) with the quadrupole mass spectrometer (QMS). The displayed TPD spectra have been background corrected, and corrected to account for mass fragmentation which occurs during ionization in the QMS (See Appendix). Fragmentation patterns were determined by characterization of pure $H_2^{16}O$ and $H_2^{18}O$ beams using the QMS. Molecular beams of water were formed from distilled, deionized $H_2^{16}O$ and isotopically labeled $H_2^{18}O$ (Isotec, 95-98% ^{18}O atom purity), which were thoroughly degassed prior to use. H_2O dose rates were calibrated by determining the time required to saturate H_2O bilayer feature using the reflectivity method of King and Wells.[71]

Films of carbon tetrachloride (CCl_4) (beam flux ~0.04 ML/s) and methanol (MeOH) (beam flux ~ 0.07 ML/s) were also utilized to investigate transport mechanisms in nanoscale ASW films. Beam fluxes and coverages of both CCl_4 and MeOH were calibrated by determining the exposure necessary to saturate the Ir(111) substrate (at T~140 K for CCl_4; at T~150 K for MeOH), as determined via the reflectivity method of King and Wells.[71] Pure CCl_4 and MeOH were thoroughly degassed prior to use without

any further purification. Like film growth of ASW, all CCl$_4$ and MeOH films were deposited at normal incidence and at a sample temperature of 77 K.

As shown previously by Safarik et. al.[72], thermal desorption of chlorodifluoromethane, CClF$_2$H, from ASW films can be used as a probe molecule to monitor crystallization kinetics and surface area changes (due to surface roughening and porosity formation)[72-73] during the transformation of ASW to CI. As will be discussed later in more detail, we utilize CClF$_2$H uptake measurements to monitor relative surface area changes in crystallizing ASW films due to crystallization-induced porosity formation. This is accomplished by using the technique of Safarik et. al.[72] Briefly, an H$_2$^{16}O ASW film is grown at T ~ 77 K on the Ir(111) substrate and is annealed at a given temperature for a desired length of time. This partially crystallized film is then immediately cooled to 77 K. The sample is then heated and held at T ~ 86.5 K (temperature at which an CClF$_2$H monolayer can form on ASW, but multilayers are quickly desorbed) and CClF$_2$H is dosed until the monolayer is saturated, as determined via the King and Wells reflectivity technique.[71] CClF$_2$H TPD spectra are subsequently obtained and the integrated TPD area determined. By repeating experiments for several anneal times (at the same temperature), changes in the *relative* surface area during ASW crystallization can be monitored.

Finally, a simple 1-D bulk diffusion-desorption model has been constructed in order to make qualitative comparisons with experimental TPD data. This model numerically solves the diffusion equation taking into account ASW crystallization[74], ASW and CI desorption parameters[75], extrapolated CI diffusion parameters[76], and allows the user to define the magnitude of the ASW bulk diffusion parameters. This simple model serves to make qualitative comparisons between the experimental mixing behavior

and the behavior expected if mixing were occurring via **bulk** diffusion between two dense phases.

Results and Discussion

ASW Mixing Experiments

Shown in Figure 3.1(a) is a temperature programmed desorption (TPD) spectra of a structure consisting of labeled ASW ($H_2^{18}O$, $H_2^{16}O$) films. The sample was constructed by first depositing 16 BL $H_2^{18}O$ ASW, followed by deposition of 16 BL $H_2^{16}O$ ASW, and finally heating to 200 K at a rate of 0.6 K/s. As the water desorption traces illustrate, water begins to appreciably desorb from the sample near T~140 K and interlayer mixing (appearance of $H_2^{18}O$) occurs between T~150 K -157 K. As we will discuss shortly, crystallization of the ASW film also occurs over this temperature range. This desorption spectra is in good agreement with data from previous investigations conducted by Smith and Kay[25,26] who have studied mixing in thin ASW films on both Au(111) and Ru(001) substrates. These investigators interpreted this observed intermixing as due to 'liquid-like' bulk diffusion between the ASW films prior to crystallization. Bulk diffusion occurring after the film has crystallized (T > 160 K), is expected to be negligible based on estimates of crystalline ice self-diffusivity.[69,76] Closer analysis of the intermixing behavior between 150 K and 160 K reveals that both sets (ours and previous investigators[25,26]) of experimental data cannot be explained via bulk diffusion mechanism alone. This inconsistency with a bulk diffusion mechanism is demonstrated in Figure 3.1(b). This figure shows the ratio of desorption rates of $H_2^{18}O$ and $H_2^{16}O$, which we refer to as "r_{18}/r_{16}" [r_{18}/r_{16}=(desorption rate of $H_2^{18}O$)/(desorption rate of $H_2^{16}O$)], determined from the TPD data of Fig. 3.1(a) and a series of desorption

Figure 3.1. ASW TPD Mixing Experiment and Desorption Ratio.
Shown in Figure 3.1(a) is a TPD mixing experiment of a structured film composed of labeled ASW ($H_2^{18}O$, $H_2^{16}O$). The sample was constructed (see schematic) by first depositing ~16 BL $H_2^{18}O$ (blue), followed by deposition of ~16 BL $H_2^{16}O$ ASW (black), and finally subsequent heating at a rate of 0.6 K/s. Molecular beams were employed which provide a uniform flux of H_2O to the entire Ir(111) sample. Shown in Figure 3.1(b) is the desorption ratio trace (open red circles) from the ASW TPD Mixing experiment shown in Figure 3.1(a). Additionally, a series of desorption ratio traces (solid lines) calculated from simple TPD desorption/diffusion model (see description in Experimental section) to illustrate mixing behavior observed in a *bulk* diffusion mechanism. The series of model desorption traces span a wide range of ASW bulk diffusion values ("high" diffusivity [E_a=220 kJ/mol; D_o=1.28 x 10^{62} cm^2/s] to "low" diffusivity [E_a=120 kJ/mol; D_o=6.42 x 10^{24} cm^2/s]). The purpose of the model calculation traces is to *qualitatively* illustrate that, regardless of the magnitude of the diffusion coefficient; the experimentally observed non-monotonic behavior is inconsistent with a bulk diffusion mechanism.

(a) H₂¹⁶O, H₂¹⁸O, Ir(111)

(b) Open Circles: Experimental
Solid Lines: Model Calcs.

43
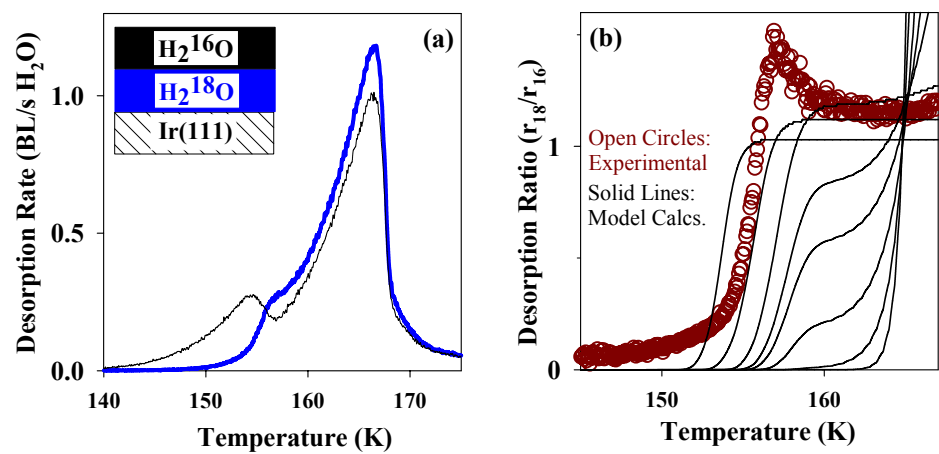
ratios (solid lines) calculated from our simple diffusion model using various bulk diffusion parameters for ASW. The quantity r_{18}/r_{16} of Fig. 3.1(b) can be viewed as an instantaneous measure of the relative surface concentrations of the isotopically labeled water molecules. If bulk diffusion were the dominant mode of transport between these ASW layers, r_{18}/r_{16} would (by necessity) increase in a monotonic fashion upon heating (as illustrated by the model calculations shown in Fig. 3.1(b)), reflecting the increase in the $H_2^{18}O$ surface concentration as it diffuses toward the top of the film. The family of model calculation curves is shown in Figure 3.1(b) to demonstrate that this characteristic behavior is exhibited regardless of the magnitude of the self-diffusion coefficient used. In contrast, the experimental desorption ratio r_{18}/r_{16} (open circles) increases sharply at T ~ 153-157 K, peaks at T ~ 157 K, decreases, and then increases (slightly) again prior to complete desorption of the water film at T ~ 166 K. Hence, the intermixing observed between the two labeled ASW films appears to be inconsistent with a bulk diffusion mechanism. This suggests that another mode of transport is at play within these films.

Fracturing/Crack Formation in ASW Films

As mentioned earlier, nanoscale ASW films are known to crack and fracture during crystallization to crystalline ice (CI). This phenomena can be observed using TPD techniques via the novel CCl_4 "molecular volcano[77]" experiment of Smith et. al. Shown in Figures 3.2(a) and 3.2(b) is an example of this particular measurement[77] conducted in our molecular beam apparatus. In Figure 3.2(a), 30 BL $H_2^{16}O$ ASW is dosed onto the Ir(111) substrate at 77 K, followed by deposition of a ~5 ML CCl_4 (see schematic) "pill" (using beam spot contained entirely within sample area). The sample is then heated and, as illustrated by the spectra, CCl_4 multilayers desorb from the sample from T ~ 120-142 K, followed by subsequent desorption of the H_2O water multilayers. Note that crystallization of the ASW film can actually be visualized (as 'bump') in the water

Figure 3.2. Example of CCl₄ "Molecular Volcano" Experiment of Smith et. al.[77]   Figure 3.2(a)-3.2(b) shows an example of the CCl₄ "molecular volcano" of Smith et. al.[77] conducted in our molecular beam apparatus. Figure 3.2(a) shows a TPD spectra of a layered film (see schematic) constructed by first depositing 30 BL $H_2^{16}O$ ASW (black), followed by deposition of a ~5 ML "pill" of CCl₄ (green dashed). Figure 3.2(b) shows a TPD spectra of a sample constructed by first depositing a ~5 ML CCl₄ "pill" (purple dashed) (signal x 0.5), followed by deposition of a 30 BL $H_2^{16}O$ ASW layer (black). TPD ramp rate for each spectra was 0.6 K/s. In depositing the ASW films ($H_2^{16}O$), a molecular beam was employed that provided uniform coverage over one face of the Ir(111) sample; for CCl₄, a different beam was used yielding a smaller deposition "spot" on the sample (~ 70% of the face area, located in the middle). For both experiments **(a)** and **(b)**, the $H_2^{16}O$ desorption spectra are identical. As the spectra illustrate, CCl₄ multilayers dosed atop the ASW film [Fig. 3.2(a)] desorb freely from the surface between T~120-142 K. When CCl₄ layers are placed below the ASW layer [Fig. 3.2(b)], they remain trapped until ASW crystallization (denoted by 'bump'). At this point, CCl₄ desorbs abruptly, presumably via vapor phase transport through crack/fractures generated within the film during crystallization.[77]
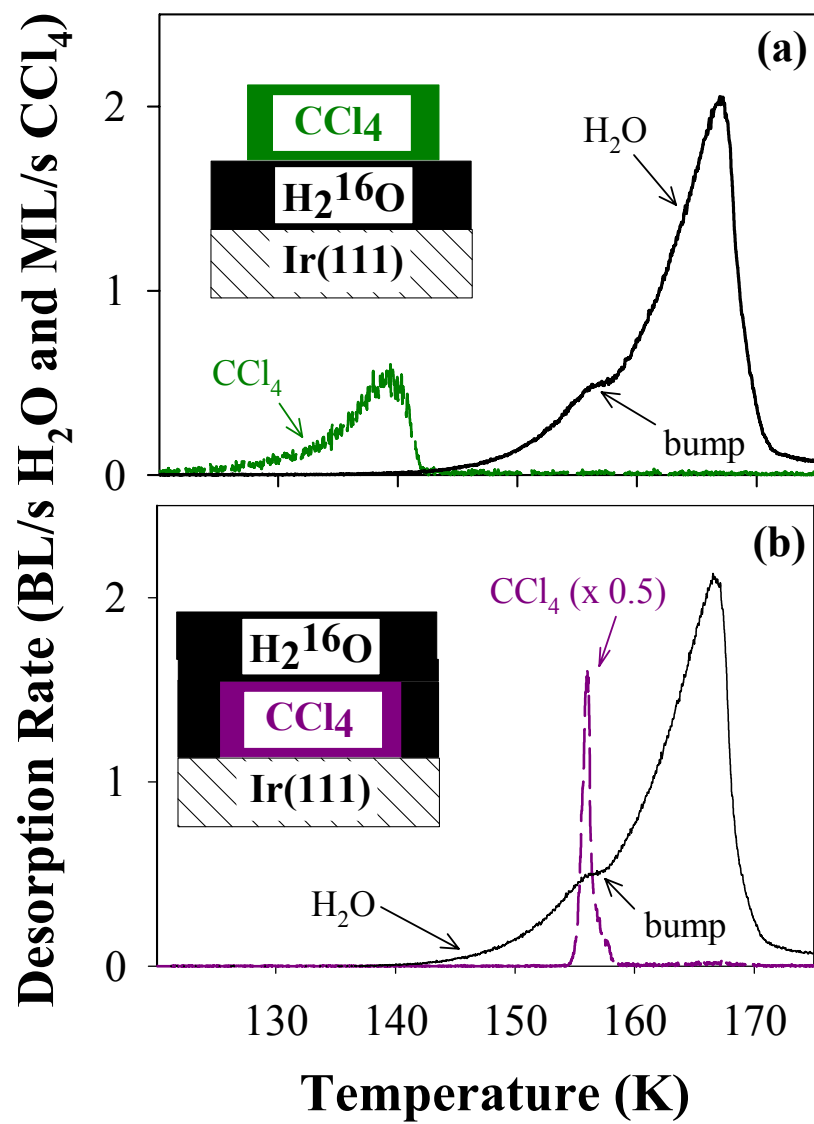
desorption spectra (see Fig. 3.2). ASW has a higher desorption rate than CI[75,78]; hence, as the film is converted from ASW to CI, a decrease in the desorption rate (bump) is observed (T ~ 154 - 155 K). In Figure 3.2(b) inset, the order of CCl_4 and ASW deposition has been reversed; first a ~5 ML CCl_4 "pill" is deposited on the Ir(111) substrate followed by deposition of the ASW overlayer (see schematic). As the layered film is heated, CCl_4 remains trapped below the ASW overlayer until the film begins to crystallize. Cracks and fractures are believed to form throughout the film during the crystallization process, presumably due to stresses created within the film during crystallization.[77,79] In addition to the Au(111) substrate used in the study of Smith et. al. this fracture phenomena has been observed on W(100) by Blanchard et. al.[80] and a number of substrates in our laboratory (Ir(111), Pt(111), TiO_2(100)). Once a complete, interconnected pathway has been created from the CCl_4 underlayer to the top of the ASW film, the CCl_4 is able to escape from beneath the water via vapor-phase transport through the crack/fracture pathways within the ASW film. This process results in an abrupt CCl_4 "molecular volcano[77]" desorption feature, since during the ASW crystallization ('bump', T ~ 154 - 155 K), CCl_4 is quite volatile. Note that the water desorption spectra in Figures 3.2(a) and 3.2(b) insets remains the same regardless of CCl_4 placement, be it on top or below the ASW film. It is also important to reiterate, that this crack/fracture formation within the film is not believed to occur *until crystallization* of ASW occurs. As stated earlier, initial dosing produces dense, non-porous ASW films.[64-68] This abrupt desorption phenomena is not unique to CCl_4, as additional data has shown that various molecules such as O_2, N_2, CH_4, Ar, trapped beneath ASW abruptly escape upon crystallization (and fracture) of the overlying layer.[79] These observations illustrate the

47

ability of these high conductance pathways to provide a means of transport for desorbing species of various character.

In addition, other evidence has been observed suggesting that ASW films undergo significant structural changes upon crystallization. Recent AFM studies by Donev et. al. have shown that thin films (~14 nm) of ASW grown on an Au thin film show appreciable changes in film topology upon annealing and crystallization (at 134 K), with crystalline grains appearing to 'deplete' nearby regions of amorphous material.[81] TEM studies by Jenniskens et. al.[82] have also demonstrated changes in glassy water film morphology upon heating. Surface area measurements by several groups have also shown crystallization induced roughening of crystallizing ASW films, presumably due to additional surface area produced by film fracture.[73,74] Souda et. al.[27,28] has conducted TOF-SIMS measurements on thin (~50 BL) ASW films grown on Ni(111) which suggest a morphological change occurs in ASW films upon heating between T~135-160 K, though this was interpreted as due to a dewetting mechanism. Additionally, multiple investigators have observed an increase in diffuse reflectance in optical interferometry measurements during crystallization of glassy water films, consistent with cracking/fracturing within the crystallizing material.[83,84] Recent studies by Kimmel et. al.[85] suggest that nanoscale ASW films dewet when annealed and crystallized at higher temperatures (T > 140 K), presumably due to the hydrophobic nature of the metal bound, H_2O monolayer. How this dewetting phenomena and film fracture (molecular volcano[77]) are related to one another (i.e.; are they the same phenomenon, or separate, distinct phenomena) remains an open question to us at this time.

A casual inspection of Fig. 3.2(b) and Fig. 3.1(a) reveals that the porosity formation in these ASW films is concurrent with the onset of isotopic mixing in structured ASW films. This suggests that these two phenomena, (1) observed interlayer

Figure 3.3. ASW TPD mixing experiments: 30 BL ASW Thicknesses.
ASW TPD mixing experiments with different structured films composed
of labeled ASW and CCl_4 are displayed. For Figure 3.3(a) 30 BL of $H_2^{18}O$
(blue) deposited first followed by 30 BL of $H_2^{16}O$ (black); Figure 3.3(b),
30 BL of $H_2^{18}O$ (blue) deposited first, then 5 ML of CCl_4 (red), and finally
30 BL of $H_2^{16}O$ (black); Figure 3.3(c), 30 BL of $H_2^{18}O$ (blue) deposited
first, followed by 30 ML of CCl_4 (red), and then 30 BL of $H_2^{16}O$ (black).
The layered structures constructed for each experiment are depicted in the
schematics shown in the lower left of each panel. For films in Fig. 3.3(a)-
(c), molecular beams were employed that provided uniform coverage to
the Ir(111) sample. All films in the figure and insets were heated at a
ramp rate of 0.6 K/s.

Figure 3(a) Inset. $H_2^{18}O/H_2^{16}O$ Desorption Ratio. Shown in Figure
3(a) inset is the desorption ratio trace (open circles) from the ASW TPD
Mixing experiment shown in Figure 3.3(a). Additionally, a series of
desorption ratio traces (solid lines) calculated from simple TPD
desorption/diffusion model to illustrate mixing behavior observed in a
bulk diffusion mechanism. The series of model desorption traces span a
range of bulk diffusion parameters ("high" diffusivity to "low"
diffusivity). The purpose of the model calculation traces is to *qualitatively*
illustrate that, regardless of the magnitude of the diffusion coefficient; the
experimentally observed non-monotonic behavior is inconsistent with a
bulk diffusion mechanism.

Figure axes and labels:

- Y-axis: **Desorption Rate (BL/s H₂O), (ML/s CCl₄)** — $Desorption\ Rate\ (BL/s\ H_2O),\ (ML/s\ CCl_4)$
- X-axis: **Temperature, T (K)**

Panel (a): inset plot with axis r_{18}/r_{16} vs $T\ (K)$, labels "Inset:", "Open Circles: Experimental", "Solid Lines: Model Calcs." Layer stack: $H_2^{16}O$, $H_2^{18}O$, Ir(111). Curves labeled $H_2^{16}O$ and $H_2^{18}O$.

Panel (b): Layer stack: $H_2^{16}O$, CCl_4, $H_2^{18}O$, Ir(111). Curves labeled $H_2^{16}O$, CCl_4, $H_2^{18}O$.

Panel (c): Layer stack: $H_2^{16}O$, CCl_4, $H_2^{18}O$, Ir(111). Labels $CCl_4 (x0.3)$, $H_2^{16}O$, $H_2^{18}O$.
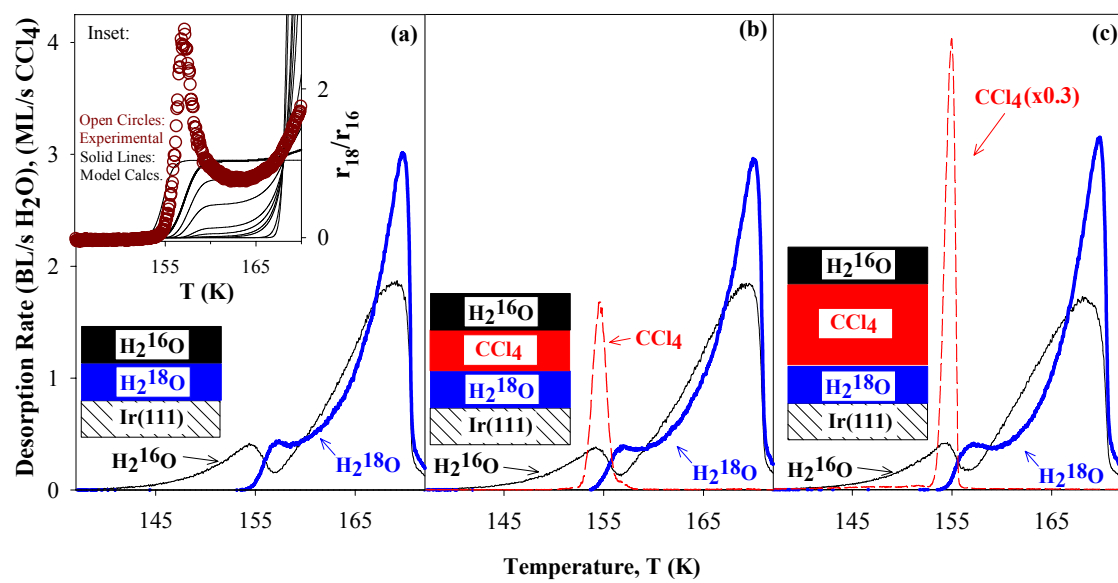
mixing in structured ASW films and (2) crystallization induced fracture formation, may be related. H_2O has an appreciable desorption rate [~0.5 BL/sec (see Fig. 3.2(a))] during film porosity formation (T ~ 154-155 K); thus, like CCl_4, underlying H_2O molecules could be available for vapor-phase transport through the interconnected fracture network created within the crystallizing film. The remainder of the manuscript will focus on experimental results which we believe strongly suggest that porosity-mediated transport, and not bulk diffusion, is the predominant mode of transport in nanoscale ASW films between T ~ 150-160 K.

CCl_4 Diffusion Barrier Experiments

Shown in Figures 3.3(a)-(c) are desorption spectra from structured films similar to Fig 3.1(a), constructed from isotopically labeled ASW ($H_2^{16}O$, $H_2^{18}O$), however various amounts of CCl_4 diffusion "barrier" layers (0, 5 and 30 ML, respectively) have been placed between the water layers (see figure schematics). These hydrophobic, immiscible CCl_4 barrier layers will serve two purposes: (1) they should provide a "diffusion barrier" to intermixing between the two isotopically labeled ASW layers prior to porosity formation in the ASW films, and (2) they will serve as a "marker" for the onset of porosity formation within ASW. (We will discuss our attempts to experimentally probe the effectiveness of this barrier layer shortly). If bulk diffusion is the primary mechanism for transport in these films, then the presence of the CCl_4 layer between T ~ 77 K and 154 K should present a hindrance to mixing between the labeled ASW layers.

Figure 3.3(a) shows a TPD spectra of a structured film prepared by deposition of 30 BL $H_2^{18}O$ ASW followed by deposition of 30 BL $H_2^{16}O$ ASW. The sample is then heated at a rate of 0.6 K/s. The desorption spectra exhibit similar behavior to experiment Figure 3.1(a) (16 BL $H_2^{16}O$ on 16 BL $H_2^{18}O$); i.e. the onset of intermixing occurs during crystallization of the ASW film (T~154 K-160 K) and are in good agreement with results

51

from previous investigators.[25,26] Shown as an inset to Fig. 3.3(a) is a plot of the desorption ratio (r_{18}/r_{16}) of the same experiment (open circles), illustrating the non-monotonic behavior which is inconsistent with a bulk diffusion mechanism (solid lines). Figure 3.3(b), constructed by depositing 30 BL $H_2{}^{16}O$, followed by 5 ML CCl_4, followed by deposition of 30 BL $H_2{}^{18}O$, exhibits remarkably similar mixing behavior to Figure 3.3(a) which contains no CCl_4 barrier layer. Likewise, Figure 3.3(c), an equivalent TPD experiment with a much thicker CCl_4 barrier layer (30 ML) exhibits mixing behavior similar (with only slight differences occurring in the spectra after 157 K) to Figures 3.3(a) and 3.3(b). The similarity between the interlayer mixing exhibited in Figures 3.3(a)-(c) is inconsistent with bulk diffusion, as the presence of a hydrophobic, immiscible layer should noticeably hinder mixing between the labeled ASW layers. These results suggest that bulk diffusion prior to exit of the CCl_4 barrier layer (154 - 155 K) is too small on these length scales (10 - 100 nm) at this heating rate.

Shown in Figure 3.4(a)-(c) are TPD mixing experiments similar to those shown in Figure 3.3(a) of structured films (see figure schematics) of labeled ASW ($H_2{}^{16}O$, $H_2{}^{18}O$) of 16 BL thickness, separated by varying amounts of CCl_4 diffusion barrier layers (0, 5, and 30 ML, respectively). The results show similar qualitative behavior as the experiments of Figure 3.4(a)-(c); i.e. remarkably similar mixing behavior between TPD spectra of structures containing no barrier layer [Fig 3.4(a)] and structures containing CCl_4 layers [Figs. 3.4(b)-(c)]. Similar to the results of Figs. 3.3(a)-(c), slight differences are observed (after T~155-156 K) when a barrier layer with a thickness of 30 ML CCl_4 is present.
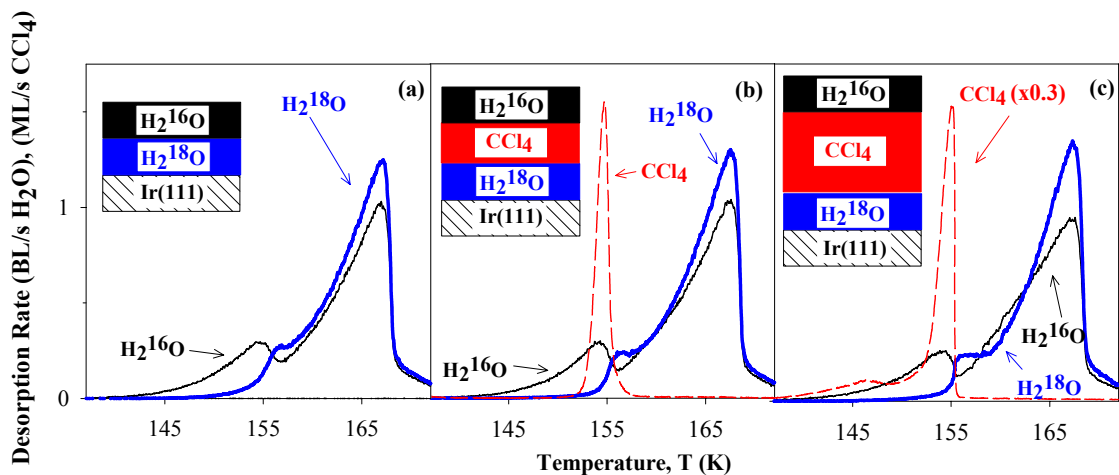
Figure 3.4. ASW TPD mixing experiments: 16 BL ASW Thicknesses.
ASW TPD mixing experiments with different structured films composed of labeled ASW and CCl_4 are displayed in Figure 3.4 For Figure 3.4(a) 16 BL of $H_2^{18}O$ (blue) deposited first followed by 16 BL of $H_2^{16}O$ (black); Figure 3.4(b), 16 BL of $H_2^{18}O$ (blue) deposited first, then 5 ML of CCl_4 (red), and finally 16 BL of $H_2^{16}O$ (black); Figure 3.4(c), 16 BL of $H_2^{18}O$ (blue) deposited first, followed by 30 ML of CCl_4 (red; signal x 0.3) and then 16 BL of $H_2^{16}O$ (black). The layered structures constructed for each experiment are depicted in the schematics shown in the lower left of each panel. For films in Fig. 3.4(a)-(c), molecular beams were employed that provided uniform coverage to the Ir(111) sample. All films were heated at a ramp rate of 0.6 K/s.

53

TPD mixing experiments (not shown) conducted with different hydrophobic barrier molecules, such as $CHCl_3$, also demonstrated behavior similar to Figure 3.3(a)-(c). This suggests that the mixing behavior is also independent of the barrier layer material. If water were somehow able to diffuse through the hydrophobic barrier layer, we might expect to observe differences in intermixing depending on the barrier material.

TPD Experiments with Different Temperature Ramp Rates

Changing the ramp rate at which TPD spectra are obtained enables alteration of the timescale over which ASW films crystallize, since crystallization is a function of both time and temperature. Thus, by modifying the timescale for crystallization, alteration of the time and temperature for the onset of porosity within ASW films should also occur. This is indeed the case as demonstrated by the data of Figures 3.5(a)-(c). These experiments show TPD mixing spectra of identical layered films composed by first depositing 60 BL $H_2^{18}O$, with subsequent deposition of a 6 ML CCl_4 "pill", followed by deposition of 60 BL $H_2^{16}O$ [see schematic in Fig. 3.5(c)] heated at different ramp rates (0.05 K/s, 0.6 K/s, and 2 K/s, respectively). The CCl_4 layer between the ASW layers serves as a "marker" for the onset of crystallization induced porosity throughout the structured film, abruptly desorbing concurrent with the creation of conductive pathways across the film. As Figs. 3.5 (a)-(c) illustrate, varying the TPD ramp rate changes the CCl_4 desorption temperature from T ~ 149 K at a ramp rate of 0.05 K/s to T ~ 160 K at a ramp rate of 2 K/s. If transport of water within these films is occurring via an interconnected porous network, altering the TPD ramp rate should also shift the onset of water mixing in a similar fashion, with the desorption of $H_2^{18}O$ in the spectra occurring nearly coincident with the CCl_4 molecular volcano desorption feature. Indeed, this is observed in the spectra of Figs. 3.5(a)-(c), with all TPD experiments exhibiting

Figure 3.5. ASW mixing experiments employing different TPD heating rates. ASW mixing experiments employing different TPD heating rates [(a) 0.05 K/s; (b) 0.6 K/s; (c) 2 K/s] to control the rate of crack/fracture creation within the ASW films are displayed in Figure 3.5. For each experiment, identical structured films of labeled ASW and CCl_4 were deposited on the Ir(111) surface held at 77 K in the following manner: 60 BL of $H_2^{18}O$ deposited first, then ~7 ML of CCl_4, and finally 60 BL of $H_2^{16}O$ was grown. Structured films were then heated at respective ramp rates. For more accurate temperature control, the 0.05 K/s experiment [Fig 3.5(a)] was first heated quickly to 130 K at ~1 K/s, then was heated to 200 K at 0.05 K/s. In depositing the two ASW films, a molecular beam was employed that provided uniform coverage of one face of the Ir(111) disk-shaped sample; for the CCl_4, a different molecular beam was used which yielded a smaller deposition "spot" (~ 70% of the face area, located in the middle). This layered structure is depicted in the schematic (not-to-scale) shown in Fig. 3.5(c). Here, CCl_4 simply serves as a marker for the onset of porosity creation[77] in the ASW films as discussed in the text and illustrated in Figure 3.2 (molecular volcano[77] of Smith et. al.). Analogous experiments without CCl_4 layers yielded similar water desorption spectra.

56
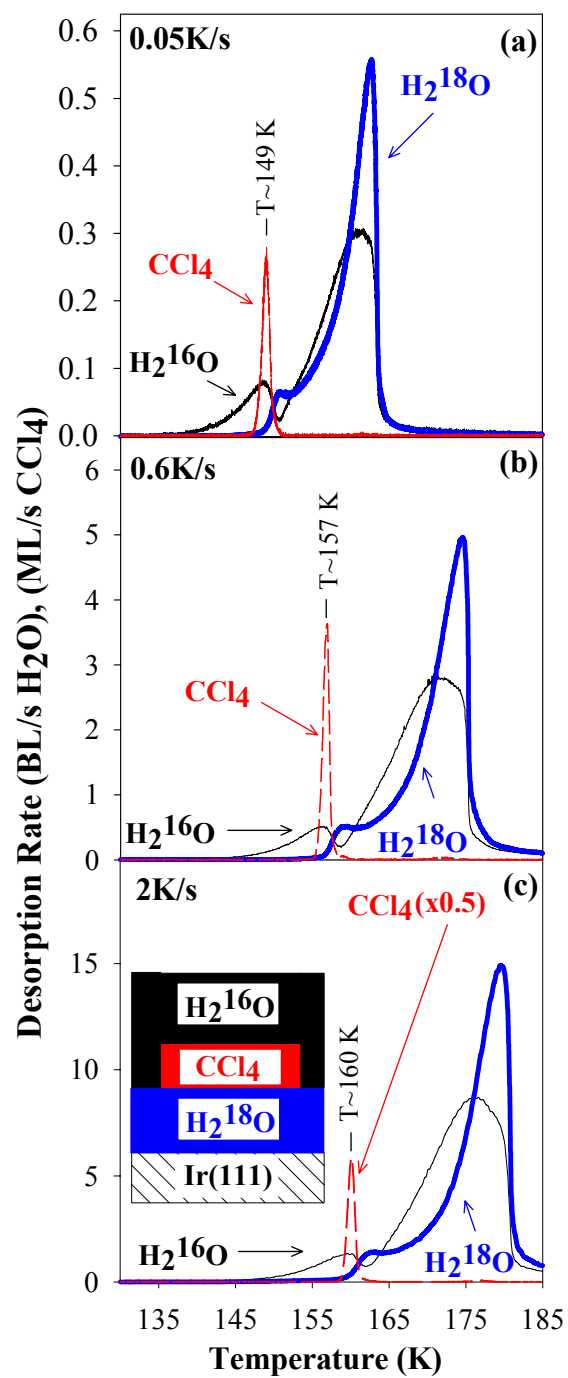
substantial mixing at each ramp rate, and with the onset of $H_2{}^{18}O$ desorption occurring during porosity formation. The ASW "bulk" diffusion parameters calculated by Smith and Kay[25,26] predict that the bulk diffusion coefficient D of ASW should change by over three orders of magnitude from T ~ 149 K to T ~ 160 K. A quick, "back of the envelope" calculation indicates that altering the TPD ramp rate of mixing experiments in this manner would then change the effective length scale (L) of mixing due to bulk diffusion within the ASW films by roughly an order of magnitude (using $D \sim L^2/t$; where t is time). We should expect (and do observe in model TPD calculations not shown here) striking differences in the experimentally observed mixing behavior as a function of TPD ramp rate, if the observed mixing were due to bulk diffusion. However, Figures 3.5(a)-(c) show similarly extensive mixing for each ramp rate, consistent with porosity-mediated transport.

Analysis of isotopically labeled mixing experiments with ASW layers of different thicknesses (30 BL on 30 BL, 100 BL on 100 BL) with different TPD ramp rates show similar qualitative behavior as those of Figure 3.5(a)-(c) [i.e.; intermixing concurrent with film fracture]. Shown in Figure 3.6(a)-(c) are several such experiments; TPD measurements conducted with ASW film thicknesses varying from 30, 60, 100 BL, conducted at a ramp rate 0.6 K/s. As the TPD experiments illustrate, the onset of mixing of each of these films occurs during crystallization and is concurrent with the onset of film fracture as evidenced by the abrupt CCl_4 desorption. Desorption ratio (r_{18}/r_{16}) behavior of these experiments are qualitatively similar [non-monotonic] to that displayed in Figure 3.1(b) and Figure 3.3(a) inset, an increase during ASW crystallization, a decrease, then a subsequent increase as the layered film continues to desorb. However, interlayer mixing observed later in the TPD spectra of these thicker films appears to be less complete than in thinner films, in agreement with previous investigators.[25,26] Closer
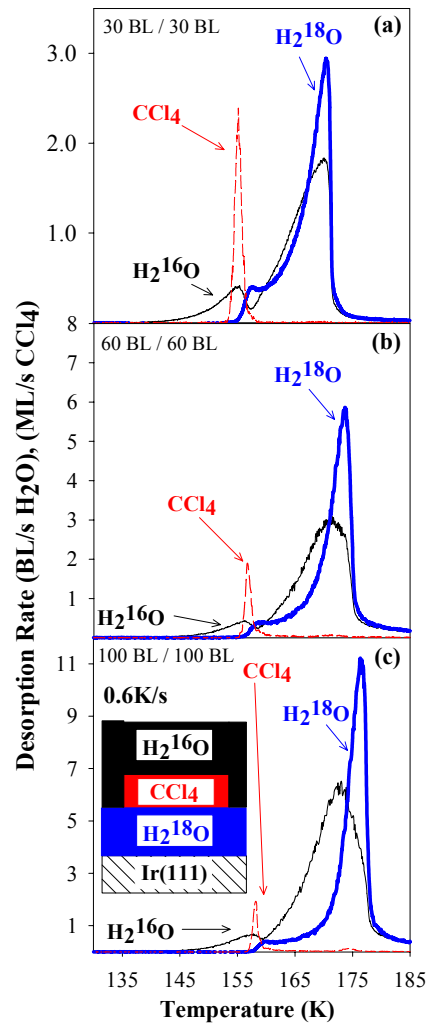
Figure 3.6. TPD Mixing Experiments with Varying ASW Thickness

Figures 3.6(a)-(c) show ASW TPD Mixing Experiments with varying thickness of ASW layers (30BL on 30BL; 60BL on 60BL; 100BL on 100BL; respectively). Each film was constructed by first dosing $H_2^{18}O$ ASW, followed by deposition of a ~5-6 ML CCl_4, 'pill', followed by dosing of $H_2^{16}O$ ASW (see schematic in figure). All structured films were then heated at a ramp rate of 0.6 K/s.

inspection of Figure 3.6(a)-(c) shows that the time for CCl_4 desorption [porosity formation] is slightly delayed for thicker films [from T~155 K to T ~ 158 K], suggesting an apparent thickness dependence on porous transport within the film. As we will discuss in more detail shortly, film thickness appears to be an important variable in the formation of cracks/fractures and transport in ASW thin films, as shown by CCl_4 "volcano" desorption[77] experiments.

Figure 3.5 illustrates that, despite variation of the heating rate, intermixing is concurrent with the onset of crystallization induced fracture of the ASW film. This behavior is observed for structured films of varying thickness (30 BL on 30 BL to 100 BL on 100BL). Though previously determined ASW bulk diffusion parameters predict dramatic differences in mixing behavior as the heating rate is altered, experiments exhibit substantial interlayer mixing at different ramp rates. These results are consistent with porosity mediated transport in nanoscale ASW films.

Isothermal ASW Mixing Experiments and Surface Area Adsorption Measurements

Intuitively, crystallization induced fracture of ASW films should result in an increase in apparent film surface area due to the creation of crack and pore surfaces. Gas uptake measurements can serve as a useful probe of material porosity, revealing the apparent surface area[86] of pore/void spaces which are connected to the material surface and, hence, are available for gas adsorption. Previous gas uptake measurements on thicker glassy water films ($CClF_2H$ on 150-1050 BL ASW films[73] and N_2 on 150 BL ASW films[74]) have displayed increases in apparent surface area occurring upon crystallization, presumably due to the introduction of cracks and fractures within the film. As shown by Safarik et. al.[72,73], uptake and desorption measurements of $CClF_2H$ monolayers from water surfaces can be instructive, revealing information about the phase (ASW,CI) and relative surface area changes of ASW films as they are crystallized. Here

CClF$_2$H gas uptake measurements are utilized to investigate changes in ASW film surface area as films of relevant thickness to our study (60 BL) are annealed isothermally (at temperatures between T~146-154 K). We then combine these surface area measurements with *isothermal mixing experiments* of layered ASW films (H$_2$^{16}O, H$_2$^{18}O) enabling comparison of mixing behavior with the changing surface area of the ASW film. If transport within ASW films is linked to porosity formation, then increases in film surface area should be observed coincident with the onset of interlayer mixing.

Before discussing the surface area/isothermal mixing measurements, we will first examine isothermal desorption features of a pure ASW film. Shown in Figure 3.7 are two isothermal desorption (T ~ 150 K; desorption rate vs. time) experiments; (1) desorption of a 60 BL H$_2$^{16}O ASW film (Fig. 3.7(b)), *and* (2) desorption of a structured film (Fig. 3.7(d)), constructed by dosing 30 BL H$_2$^{18}O ASW, followed by deposition of a ~7-8 ML CCl$_4$ 'pill', followed by dosing of 30 BL H$_2$^{16}O ASW. Once deposited, each of the films are heated and held at T~150 K, according to the heating schedule displayed in Figure 3.7(a), and desorbing species are monitored via the QMS. In the case of Figure 3.7(b), when the 60 BL H$_2$^{16}O ASW film reaches T~150 K (around t ~ 148 sec) it is desorbing as ASW (desorption rate ~ 0.18 BL/s). During the anneal at T ~ 150 K, the ASW begins to convert to CI (which has a lower desorption rate than ASW[75,78]); this crystallization process is manifested in the decrease in desorption rate which occurs between t~152 sec and t~182 sec. Note that this decrease in the desorption rate is the same behavior that gives rise to the 'bump' in the TPD ramp rate experiment of Figure 3.2(a)-(b). This behavior has been observed previously in several isothermal desorption studies of ASW films.[73,87,88] Once the film is completely transformed, it proceeds to desorb as CI (desorption rate of ~0.10 BL/s) until the entire multilayer film is desorbed (t~750 sec).

Figure 3.7. Isothermal Desorption Pure and Structured ASW Films. Figure 3.7(b) shows isothermal desorption of 60 BL $H_2^{16}O$ ASW film (black). The heating schedule shown in Fig. 3.7(a) was used to heat the ASW film to T ~ 150 K (heating between t=0-148 s; ramp rate ~0.5 K/s) and held there while desorbing species were monitored. The decrease in the desorption rate of the pure water film (t=152-182 s) occurs due to crystallization of the ASW film to crystalline ice (which has a lower desorption rate).[75,78] Displayed in Figure 3.7(c) are relative surface area measurements (solid circles) of the 60 BL $H_2^{16}O$ film obtained by employing the $CClF_2H$ probe molecule (as described in experimental section). Shown in Figure 3.7(d) is an isothermal desorption spectra of a structured film, prepared by deposition of 30BL $H_2^{18}O$ ASW (blue), followed by deposition of ~7-8 ML 'pill' of CCl_4 (red; signal x 0.25), and finally deposition of 30 BL $H_2^{16}O$ ASW (black). This structured film was heated to T ~150 K with an identical heating schedule as Fig. 3.7(b), thus allowing for direct comparison of the two spectra. As the data illustrates, crystallization of the film is concurrent with (i) onset of intermixing of $H_2^{18}O$, (ii) crystallization induced film fracture (abrupt CCl_4 desorption), and (iii) onset of surface area increases in the ASW film.
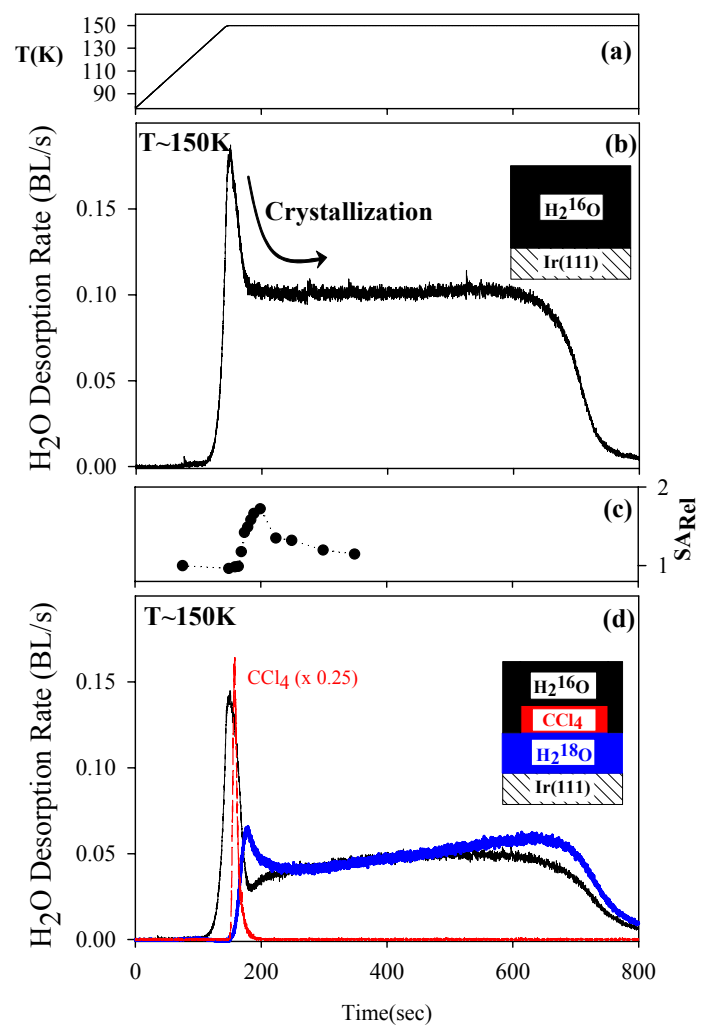
Shown in Figure 3.7(c) are relative surface area measurements of the 60 BL ASW film (such as that shown in Fig. 3.7(b)) as it is annealed at T~150 K. This surface area data was obtained by measuring uptake of the $CClF_2H$ probe molecule[72,73], employing the method described previously in the experimental section. The heating schedule used for these measurements is that of Fig 3.7(a); hence, these results can be compared directly to the experiment of Fig 3.7(b). As the data illustrate, the relative surface area of the film increases as the ASW begins to crystallize; after crystallization, decreases in surface area are observed upon further annealing. As we will discuss shortly, this behavior suggests the formation of crystallization induced cracks are dynamic in nature, both opening and sintering closed during annealing.

Shown in Figure 3.7(d) is the isothermal desorption spectra of the layered ASW film (see schematic). This sample has been heated to T ~ 150 K in a fashion identical to Figure 3.7(b) and the films are of similar total thickness (~ 60 BL), thus allowing for comparison between the two desorption spectra and the surface area measurements of Fig. 3.7(c). What becomes apparent upon comparison of the Fig. 3.7 spectra are the coincidence of (i) intermixing between the isotopically labeled ASW layers, (ii) onset of porosity (evidenced by abrupt CCl_4 desorption), and (iii) onset of apparent surface area increases with ASW film crystallization. We can now use this background information to study isothermal mixing experiments (with concurrent surface area measurements) conducted over a range of temperatures.

Shown in Figure 3.8(a)-(c) are isothermal desorption mixing measurements conducted at 146 K, 152 K, and 154 K, respectively. Displayed above each experiment are relative surface area measurements (relative to the surface area of an ASW film annealed to T ~ 115 K)[73] obtained from $CClF_2H$ desorption measurements conducted on 60BL ASW films. As the spectra illustrate, the isothermal desorption measurements

Figure 3.8.   Isothermal ASW Mixing Experiments with CClF$_2$H Uptake Measurements.   Shown in Figure 3.8(a)-(c) are isothermal anneals of structured ASW films (see cartoon) grown by dosing 30 BL H$_2$^{18}O ASW (blue), followed by 30 BL H$_2$^{16}O ASW (black). Films are then heated to the desired anneal temperature (146 K, 152 K, and 154 K, respectively) and the films are allowed to desorb. Shown above Figures 3.8(a)-(c) are relative surface area measurements (SA$_{rel}$) (solid circles) obtained from 60 BL H$_2$^{16}O ASW films annealed to 146 K, 152 K, and 154 K, respectively, using CClF$_2$H probe molecule.[72-73] These surface area measurements reflect the changes in *relative* surface area during the mixing experiment due to crystallization induced film fracture and roughening, relative to the initial film surface area. Heating schedules similar to that shown in Figure 3.7(a) were used to heat the structured films to their respective desorption temperatures.

65
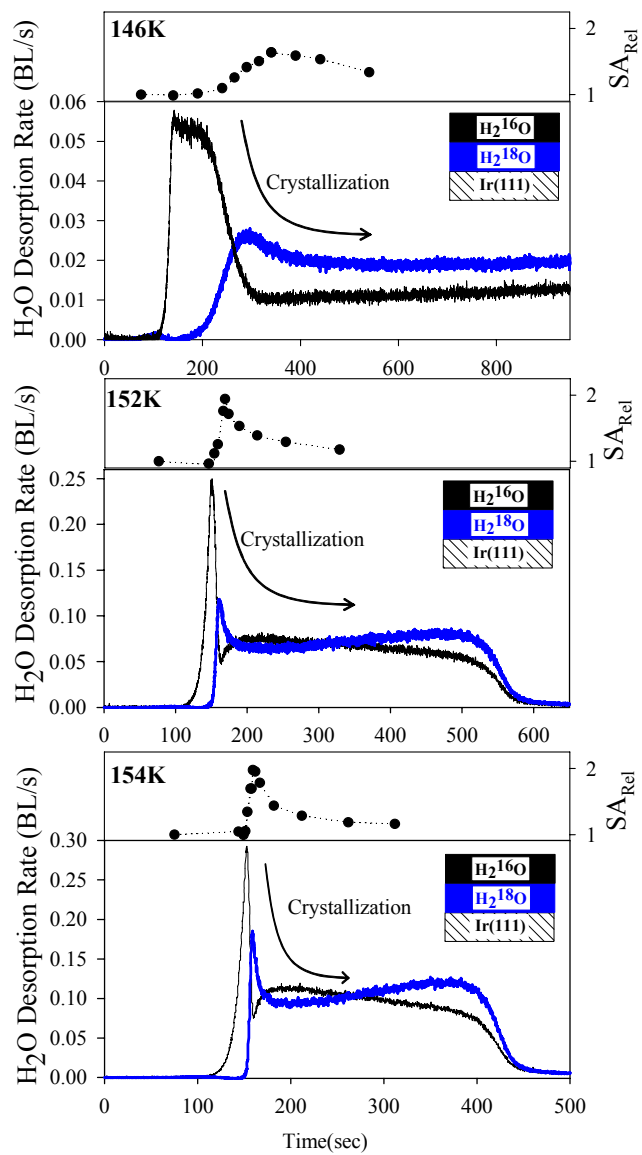
exhibit mixing behavior seen in ramp rate TPD mixing experiments, with the underlying $H_2^{18}O$ layer exhibiting substantial desorption during crystallization, and hence during crack/fracture formation within the films. This behavior is apparent over the T~146 -154 K temperature range of the experiments. Similar to the behavior of Fig. 3.7(c), the relative surface area during all anneal temperatures (T~146 K-154 K) is observed to first increase during crystallization, then decrease after crystallization as the transformed film is further annealed. This suggests, as has been previously hypothesized[73], that cracks and fractures formed within the ASW can densify or collapse upon further annealing. As we will discuss later, this sintering process may play a key role in the mixing behavior observed in our TPD spectra, eliminating these crack/fracture pathways from further mixing after crystallization and possibly trapping water molecules within the densifying film. These trends are similar to those seen by Safarik et. al. for crystallization of much thicker ASW films at lower annealing/crystallization temperatures.[72] For the isothermal anneals, peak surface area increases correspond to, *at least,* a roughly two-fold increase in internal surface area, for anneal temperatures of 146 K to 154 K, since uptake measurements can only probe pore/void spaces connected *directly* to the film surface. These large increases in the apparent surface area of the film highlight the dramatic structural changes which occur within ASW thin films during crystallization. What is important to note is that the onset of intermixing is coincident with the onset of surface area increases. This evidence further suggests a connection between the observed ASW mixing and crack/fracture formation.

CCl$_4$ Barrier Layer Effectiveness: Methanol Probe Experiments

As discussed earlier, the CCl$_4$ diffusion barrier experiments of Figures 3.3 and 3.4 suggest that negligible bulk diffusion is occurring within ASW films prior to the onset of

crystallization induced film fracture. Determining the effectiveness of the CCl_4 barrier layer is important with regard to such conclusions made about bulk diffusion in dense ASW prior to the onset of fracture within the ASW film. Intuitively, one would expect a hydrophobic, immiscible CCl_4 barrier layer [such as those employed in Figure 3.3 and 3.4] to hinder bulk diffusion between isotopically labeled ASW layers until the onset of crystallization-induced cracks (molecular volcano)[77], the point at which the CCl_4 diffusion barrier layer is allowed to escape from beneath the water overlayer. This CCl_4 barrier layer should hinder bulk diffusion between ASW layers due to both the hydrophobic effects of the CCl_4 layer and the additional spacing between the films (t ~ L^2/D). Issues such as CCl_4 barrier layer roughness and CCl_4 wetability (how well CCl_4 covers the entire $H_2^{16}O$ / $H_2^{18}O$ interface) could influence the effectiveness of the CCl_4 barrier toward blocking H_2O bulk diffusion and therefore the validity of our conclusions. Thus we have attempted to quantify the effectiveness of the CCl_4 diffusion barrier layer using methanol (MeOH) as a barrier "probe" molecule. Interestingly, we find that the polar MeOH molecule exhibits mobility through dense ASW films. Previous TPD-TOF SIMS experiments by Souda[28] and TPD experiments by Livingston et. al.[89] have also confirmed that MeOH appears to be, at low temperatures, fairly mobile in thin amorphous and crystalline ice films (although, in contrast to the results of Souda et. al.[28] we do not see a suppression of morphological change in ASW due to MeOH). If CCl_4 provides a good barrier to MeOH mobility, one might expect it to be a good diffusion barrier for H_2O.

Figures 3.9(a)-(e) shows desorption of multilayers of MeOH from bare Ir(111), 30 BL ASW H_2O, and from underneath various water overlayers (15-90 BL). MeOH multilayer desorption (Fig 3.9(a)) appears to occur between T ~ 125-143 K for a MeOH coverage of 8 ML, with an activation energy of (E_d ~ 0.39 eV), based on zero order

Figure 3.9. MeOH ASW Mixing Experiments. Shown in Figure 3.9(a)-(e) are TPD spectra of various structured films of ASW (black) and MeOH (green) (see cartoons). Figure 3.9(a) shows a TPD spectra of an 8 ML coverage of MeOH from Ir(111). Figure 3.9(b) shows a TPD spectra of a structured film constructed by first dosing 30 BL $H_2^{16}O$ ASW, followed by deposition of ~8 ML MeOH. Figures 3.9(c)-(e) are desorption spectra from structured films created by first dosing ~8 ML MeOH on Ir(111), followed by dosing of various amounts of $H_2^{16}O$ ASW (30, 60, and 90 BL, respectively). MeOH desorption monitored via m/z~31.
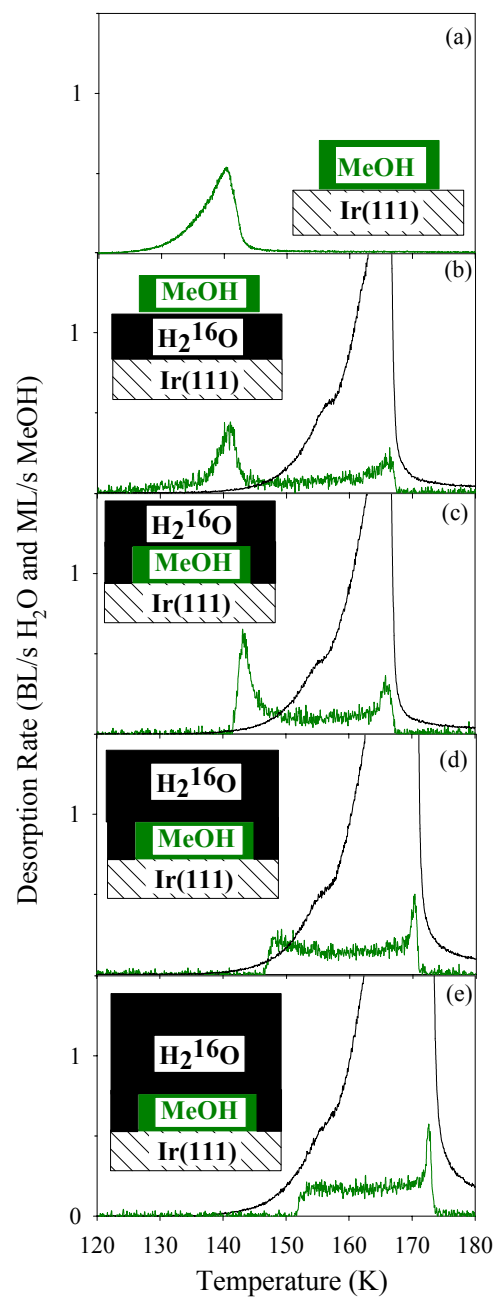
desorption kinetics. When MeOH multilayers are deposited and desorbed from atop a 30 BL $H_2^{16}O$ ASW film, two desorption features become apparent in the subsequent TPD spectra, as shown in Figure 3.9(b). In this experiment, 30 BL $H_2^{16}O$ ASW has been deposited first, followed by dosing of ~8 ML MeOH. Upon heating, the first desorption feature occurs near the MeOH multilayer desorption feature (T ~ 130-145 K), with the second occurring near the end of the H_2O desorption feature. This second desorption feature, occurring between T ~ 160 K-170 K, is coincident with the end of desorption of the underlying water film. Figures 3.9(c)-(e) show TPD spectra from samples in which ~8 ML MeOH has been dosed on the Ir(111) sample first, followed by dosing of ASW overlayers of varying thickness (30-90 BL). As the spectra illustrate, the first MeOH desorption feature shifts in temperature as a function of water overlayer thickness, from T~ 143 K [Fig. 3.9(c)] to T ~ 152 K [Fig. 3.9(e)], presumably due to the additional ASW layers the methanol must traverse to reach the surface of the ASW film. Interestingly, no "volcano" effect is seen for MeOH desorption during ASW crystallization (T ~ 155 K), further suggesting that MeOH is able to intermix well with the ASW film prior to crystallization and film fracture. After its initial desorption feature, MeOH proceeds to desorb from each of the films in Figs 3.9(c)-3.9(e) at a nearly constant rate as the ASW film proceeds to crystallize and desorb from the sample. A second MeOH feature again is seen concurrent with the completion of desorption of the water overlayer, increasing in intensity with increasing ASW overlayer thickness. While currently we can only speculate on the nature of this second TPD feature, it could be due to an associated water/methanol complex (such as a methanol hydrate) which is known to occur in low temperature H_2O / MeOH mixtures with high methanol concentration (~1:1 ratio).[90] This may explain why, even when MeOH is placed atop the ASW film, it still exhibits a MeOH feature coincident with the completion of ASW desorption. Regardless, what is

important to note is that these spectra demonstrate MeOH can exhibit mobility through dense ASW films on these length scales *prior* to crystallization (and, hence, prior to porosity formation). As we will try to illustrate in the following discussion, this information can be used to help study the effectiveness of CCl_4 barrier layers to MeOH transport in ASW.

Figures 3.10(a)-(e) show TPD spectra obtained from structured films of MeOH, CCl_4, and $H_2^{16}O$ ASW (see figure schematic) with various CCl_4 barrier layer thicknesses (0 - 60 ML). These films were constructed in the following manner: first, ~8 ML MeOH are dosed onto the Ir(111) sample; next 30 BL $H_2^{16}O$ ASW are dosed; third, a CCl_4 barrier layer of desired thickness was dosed; finally, 30 BL $H_2^{16}O$ ASW are dosed and the sample was heated at 0.6 K/s. The spectra show that when CCl_4 barrier layers are present in ASW films, the MeOH desorption trace is delayed, presumably due to the presence (hydrophobicity and additional length) of the CCl_4 barrier layer. While it appears that 5 ML CCl_4 [Fig 3.10(b)] provides some hindrance to MeOH transport through the structured film (onset of MeOH desorption is delayed from T~148 K until T~152 K), 15 ML of CCl_4 [Fig 3.10(c)] appears to be a sufficient thickness to completely halt MeOH desorption until the molecular volcano feature (T ~ 155 K). For CCl_4 barrier thicknesses of 15 - 60 ML [Figs 3.10(c)-(d)], the first MeOH desorption feature is delayed and always appears concurrent with the molecular volcano feature, the point at which the CCl_4 diffusion barrier layer is allowed to escape. Experiments conducted at TPD ramp rates of $\beta = 0.05$ K/s and $\beta = 2$ K/s show similar behavior; i.e. the appearance of MeOH tracer occurs concurrent with abrupt desorption of CCl_4 due to crystallization induced porosity.

71

Figure 3.10. **CCl$_4$ Diffusion Barrier Layer:** **CCl$_4$ Thickness Dependence.** Shown in Figure 3.10(a)-(e) are TPD spectra of structured films prepared as follows (see cartoon): First, ~8 ML MeOH "pill" (green) is deposited on the Ir(111) substrate, followed by 30BL H$_2^{16}$O ASW (black), followed by 0-60 ML CCl$_4$ (red; thickness denoted in figure), followed by 30BL H$_2^{16}$O ASW (black). All experiments conducted at a ramp rate of 0.6 K/s. Spectra demonstrate for CCl$_4$ barrier layer thicknesses > 15 ML, MeOH tracer does not appear until after CCl$_4$ desorption (porosity formation).

Y-axis: BL/s H2O and ML/s of MeOH and CCl4

X-axis: Surface Temperature (K)

(a) 0ML CCl4, H$_2$^{16}O, MeOH

Inset: H$_2$^{16}O, CCl$_4$, H$_2$^{16}O, MeOH, Ir(111)

(b) 5ML CCl4, H$_2$^{16}O, MeOH, CCl4

(c) 15ML CCl4, CCl4 (x0.25), H$_2$^{16}O, MeOH

(d) 30ML CCl4, CCl4 (x0.15), H$_2$^{16}O, MeOH

60ML CCl4, CCl4 (x0.10), H$_2$^{16}O, MeOH

73
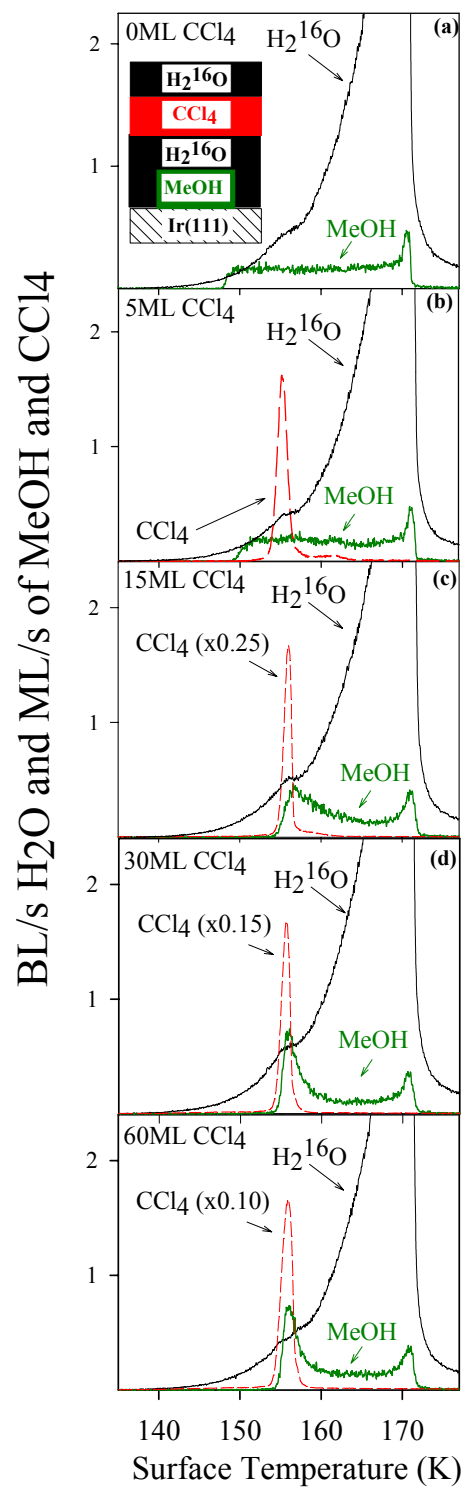
Figures 3.11(a)-(d) show TPD spectra obtained from structured films of MeOH, CCl$_4$, and H$_2$^{16}O ASW (see figure schematics) in which the MeOH layer position has been shifted throughout the structured film. Figures 3.11(c)-(d) show films constructed such that the MeOH layer has been placed directly below the 30 ML CCl$_4$ layer and on the Ir(111) surface, respectively. As the spectra in Figs. 3.11(c)-(d) suggest, transport of MeOH layers appear to be completely hindered by the CCl$_4$ layer, with MeOH desorption appearing concurrent with the molecular volcano feature at T ~ 155 K. Figs 3.11(a)-(b) show films in which the MeOH layer has been placed directly above the CCl$_4$ layer and on top of the entire structured film. These experiments show that MeOH multilayers placed below the CCl$_4$ layer do not appear until the CCl$_4$ barrier layer is removed during porosity formation. Experiments in which MeOH is placed above the CCl$_4$ barrier are unhindered by the presence of the barrier layer, and hence are able to traverse the ASW film and desorb much sooner.

Taken together, we interpret these results to suggest that CCl$_4$ barrier layers with thicknesses greater than 15 ML provide an effective barrier to MeOH transport prior the onset of film fracture. Thus, it seems reasonable to argue that bulk transport of H$_2$O, a molecule similar to MeOH, would also be hindered by the presence of the CCl$_4$ layer. Though CCl$_4$ barrier layers with a thickness of less than 15 ML do provide some hindrance to MeOH transport, it is possible that these thicknesses do not provide a complete conformal layer between the ASW films. We speculate this behavior could arise due to de-wetting of the initial layers of CCl$_4$ on ASW due to hydrophobic effects.

One point of our analysis of Figures 3.9-3.11, worth mentioning, remains a bit ambiguous. Methanol, (MeOH), is a molecule similar to H$_2$O in many ways (i.e., polar, hydrogen-bonding, highly miscible in water) Thus, it seems MeOH might be a good

Figure 3.11. CCl₄ Diffusion Barrier Layer: Location Dependence.
Shown in Figure 3.11(a)-(d) are TPD spectra of films prepared such that the MeOH (green) tracer "pill" (~8 ML) has been placed in various locations throughout a 30BL $H_2^{16}O$ (black) / 30ML CCl₄ (red)/ 30BL $H_2^{16}O$ (black) structured film (see cartoons). All TPD spectra were obtained at a ramp rate of 0.6 K/s. As the spectra illustrate, films where the MeOH tracer is placed above the CCl₄ barrier layer (Figs. 3.11(a),(b)) exhibit MeOH desorption prior to crystallization. Structured films where the MeOH tracer is placed below the CCl₄ barrier layer (Figs. 3.11(c),(d)) exhibit MeOH desorption once the CCl₄ barrier layer abruptly desorbs, allowing underlying species to desorb via porous transport. In all spectra, CCl₄ signal (red) is reduced by a factor of (x 0.15)
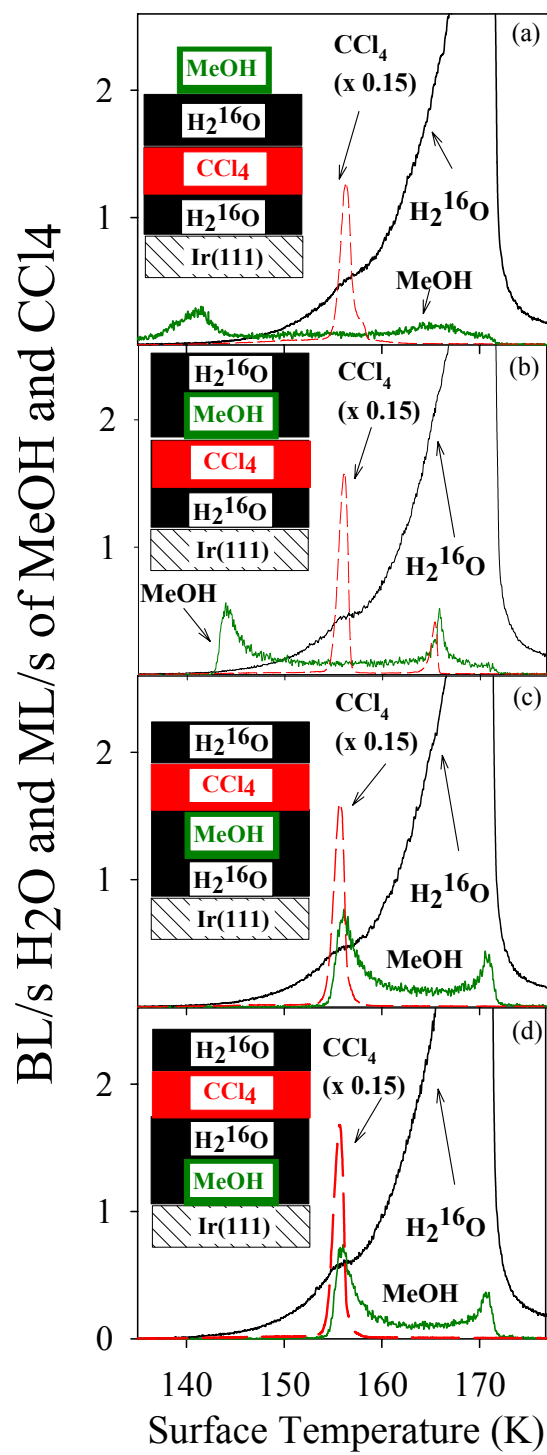
'probe' molecule to test the effectiveness of the non-polar, CCl_4 'barrier' layers to H_2O mobility. As recently discussed, the data of Figures 3.10-3.11 seem to suggest that these layers do hinder MeOH mobility in structured films. One question that naturally arises is, if MeOH which can intermix well with H_2O, why shouldn't water exhibit similar diffusive mobility in thin ASW films near the same temperatures? Though we do not have a simple answer to this issue at this time, it should be reiterated that the evidence of low temperature MeOH mobility in low temperature H_2O phases is not unique to our study. As mentioned earlier, previous investigations have suggested that MeOH is mobile in both ASW[28] and CI[89] thin films. Experiments by Souda et. al.[28] (employing thin ASW and MeOH films) suggest that MeOH intermixes with ASW around T~135-140 K. This apparent mobility has indeed been cited[28] as evidence of a glass-liquid transition in thin ASW films. Despite these ambiguities, we believe the MeOH experiments of Figures 3.9-3.11 are instructive in examining the effectiveness of the CCl_4 layers in hindering bulk diffusive transport and do provide some useful information with regards to the present study. We view these experiments as an opportunity to probe the effectiveness of the CCl_4 layer with a molecule that appears to exhibit mobility across the ASW film prior to crystallization (Figure 3.9). This "high" mobility of MeOH in ASW allows for investigation of the effectiveness of the CCl_4 layer prior to film crystallization with a molecule "similar" to H_2O. As illustrated by Figures 3.10-3.11, at thicknesses greater than 15 ML, the CCl_4 'barrier' layer appears to block the appearance of MeOH at the film surface prior to film fracture.

In light of these MeOH results, we interpret the similarity of the TPD mixing spectra of Fig. 3.3(a) (no bulk diffusion barrier) and Figs 3.3(b)-(c) (5 ML and 30 ML diffusion barrier, resp.) to suggest that any bulk diffusion occurring between nanoscale ASW films prior to crystallization is very small. This suggests the substantial mixing

exhibited by these films during crystallization is not due to bulk diffusion; rather, we argue the mixing to be primarily attributed to cracking/fracturing of the crystallizing ASW films.

Transport through Cracks/Fractures in ASW

Transport of vapor-phase species through the interconnected network created in crystallizing films is likely to be a complicated process dependent on a number of variables, including crack/fracture propagation kinetics, crack/fracture sintering kinetics, and the desorption rate of the water molecule. Additionally, transport in porous media can often be a complicated combination of Knudsen diffusion (free molecular flow), viscous flow, ordinary diffusion, and surface diffusion modes.[91,92] Physical parameters key to defining the relevant transport conditions locally within the porous film, such as pore sizes and distributions, geometry of pore pathways, and nature of vapor phase within the pores (viscous, molecular flow) are currently ill-defined. Thus, developing a complete, *quantitative* model of porous transport within crystallizing ASW films remains a challenging task. Despite these difficulties, we can obtain important *qualitative* information regarding the porosity creation and transport through these pathways during crystallization. Here we present experiments probing the effects of film thickness and heating schedule on crack/fracture formation and transport in ASW using CCl_4 as a "marker" for porosity formation. As we will attempt to illustrate, this information can aid in understanding, on a *qualitative* level, the mixing behavior in structured, labeled water films and the relationship between pore formation/transport and variables such as film thickness and heating schedule.

Experiments (such as those shown in Figures 3.6(a)-(c)) demonstrate that ASW film thickness plays a role in the transport behavior observed in labeled, structured films.

Figure 3.12. CCl₄ Desorption Experiments: Increasing ASW Overlayer Thickness. Shown in Figure 12(a)-(f) are TPD spectra of TPD desorption experiments of films constructed by first depositing ~6 ML CCl₄ "pill" (black) on the Ir(111) surface, followed by deposition of varying amounts (15-500 BL) of ASW $H_2^{16}O$. All TPD spectra were conducted at a ramp rate of 0.6 K/s. H_2O desorption spectra (m/z~18) are not shown in the figure due to their large scale. In cases in which the H_2O desorption signal saturated the QMS multiplier (thicknesses > 180 BL), H_2O desorption could be monitored by the scattering chamber pressure (ion gauge). **Inset Figure 12.** The inset to Figure 3.12 is a plot of "trapped CCl₄" as a function of ASW film thickness. "Trapped" CCl₄ refers to the amount of the initially dosed (6 ML) CCl₄ that is present in the 2nd CCl₄ feature occurring at higher temperatures. This feature appears near the completion of ASW overlayer desorption (2nd CCl₄ feature "straddles" the ASW multilayer desorption peak).
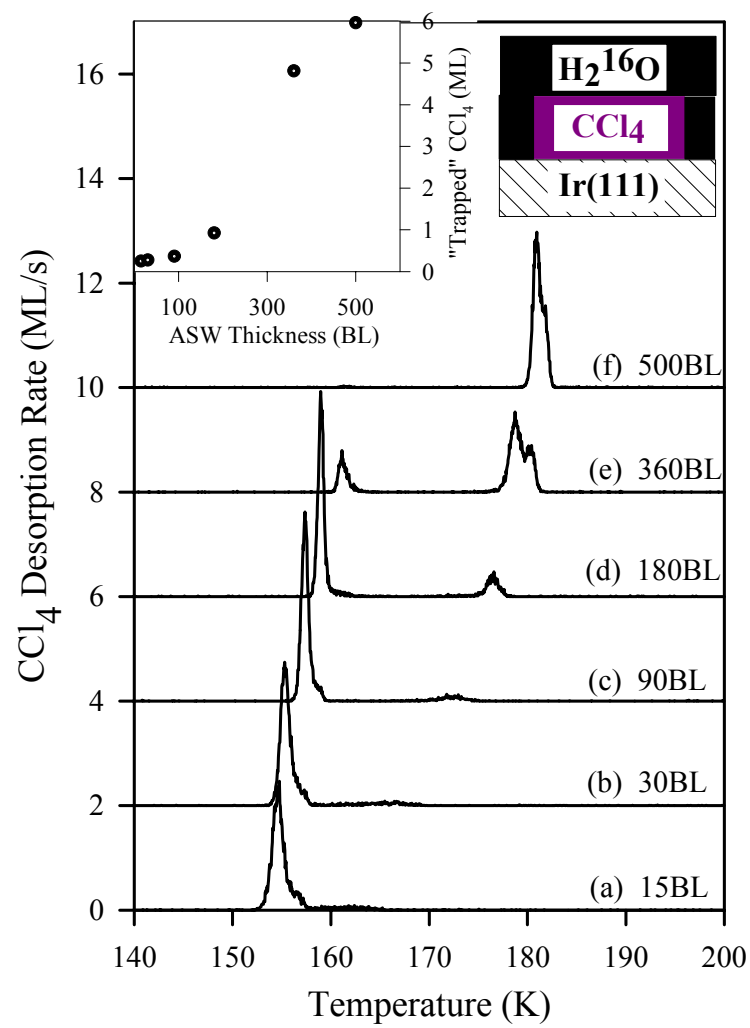
As layered films increase in thickness, overall mixing becomes less complete upon subsequent crystallization and desorption. We have conducted measurements of CCl_4"volcano" desorption, shown in Figure 3.12, with films of increasing ASW overlayer thickness to gain some further insight into the role of film thickness on film fracture and transport. In these experiments, ~6 ML of CCl_4 (black) is deposited on the Ir(111) substrate, followed by deposition of varying amounts (15 - 500 BL) of amorphous solid water; subsequent desorption follows at a heating rate of 0.6 K/s. As the spectra illustrate, increasing film thickness results in different CCl_4 desorption behavior. As overlying ASW film thickness is increased from 15 to 90 BL, abrupt CCl_4 desorption is shifted from T ~ 155 K to T ~ 158 K. This trend is consistent with that observed by Smith et. al., who observed an increase in abrupt CCl_4 desorption temperature with increasing D_2O ASW overlayer thickness (from 30 - 60 BL).[77] In Figures 3.6(a)-(c), this *same* delay in the abrupt CCl_4 desorption [and isotopic mixing] is observed as the thickness of the structured film is increased.

As the ASW overlayer thickness is further increased to 180, 360, and 500 BL, a 2nd CCl_4 desorption feature, at later temperatures, becomes increasingly apparent in the CCl_4 desorption spectra. This CCl_4 desorption feature coincides near the completion of ASW overlayer film desorption [i.e, the CCl_4 peak "straddles" the H_2O multilayer desorption peak temperature] . We attribute this feature to CCl_4 which remains "trapped" below the crystallized ASW layer, either unable to escape through cracks/fractures prior to sintering (due to the increased pore length) and/or are not sufficiently interconnected to the ASW surface to escape. Thus, CCl_4 is able to desorb freely from the sample near the end of the H_2O overlayer desorption, when a substantial portion of the water overlayer has been removed. Shown in the inset of Figure 3.12 is a plot of this "trapped" CCl_4 (expressed as portion of 6 ML CCl_4 initially adsorbed onto the Ir(111) substrate) as a

function of ASW film thickness. As the spectra and the inset plot demonstrate, complete "trapping" of the CCl_4 occurs at a thickness of ~500 BL. These results give an estimate of the ASW film thickness (ASW film thickness of 360 - 500 BL) over which crack/fracture in ASW is relevant with regard to CCl_4 transport; i.e. the length scale at which crack pathways cannot sufficiently span and/or CCl_4 molecules cannot traverse prior to film sintering. All mixing experiments (both isothermal and TPD) conducted in our study have thickness less than 360-500 BL; hence, we should expect these films to have crack/fracture pathways spanning their entire film thickness. The decrease in apparent mixing (Figure 3.5(a)-(c)) we observe in thicker structured, labeled water films are consistent with this idea; as film thickness is increased, interlayer mixing is lessened, presumably by the reduction in the number of cracks/fractures that span the entire water film and/or kinetic competition with pore sintering.

This apparent "delay" in the 1st CCl_4 desorption feature [concurrent with crystallization] with increasing overlayer thickness can be related to a number of factors. First, as shown in previous studies[88], for thin ASW films (thicknesses < 55 BL) timescales for crystallization increase with increasing film thickness. Since film fracture is intimately linked to the crystallization process, the delays in CCl_4 desorption could be due to delays in crystallization and development of the interconnected network within the film. The increased pore length CCl_4 must traverse to reach the film surface is another factor which could cause delays in the CCl_4 desorption spectra as a function of overlayer thickness. To further probe this possibility, we have conducted experiments, shown in Figure 3.13, in which 6 ML CCl_4 has been placed at various locations within an ASW film of constant thickness (90 BL). These experiments were conducted to attempt to investigate the effect of film thickness on CCl_4 transport in a film of constant thickness, and, hence, similar crystallization kinetics for each experiment. As the results

82

Figure 3.13.   CCl$_4$ Desorption: Constant ASW Film Thickness.
Experiments shown were conducted to study the escape of CCl$_4$ from within an ASW film of constant thickness (~90 BL) as a function of location.   Each experiment was conducted by first dosing the desired amount of H$_2$^{16}O at 77 K, followed by deposition of a small CCl$_4$ "pill" (purple) (6-7 ML), followed by deposition of desired amount of H$_2$^{16}O, maintaining the total ASW thickness of 90 BL. Structured films were then heated at 0.6 K/s to 200K and desorbing species were monitored. Results suggest that, even in a film of constant thickness and similar crystallization kinetics, abrupt CCl$_4$ desorption is dependent overlying film thickness.

The y-axis label reads "CCl$_4$ Desorption Rate (ML/s)" and the x-axis label reads "Temperature (K)".

Right-side stacked diagrams:

(f)
90 BL H$_2$^{16}O
CCl$_4$
Ir(111)

(e)
75 BL H$_2$^{16}O
CCl$_4$
15 BL H$_2$^{16}O
Ir(111)

(d)
60 BL H$_2$^{16}O
CCl$_4$
30 BL H$_2$^{16}O
Ir(111)

(c)
45 BL H$_2$^{16}O
CCl$_4$
45 BL H$_2$^{16}O
Ir(111)

(b)
30 BL H$_2$^{16}O
CCl$_4$
60 BL H$_2$^{16}O
Ir(111)

(a)
15 BL H$_2$^{16}O
CCl$_4$
75 BL H$_2$^{16}O
Ir(111)
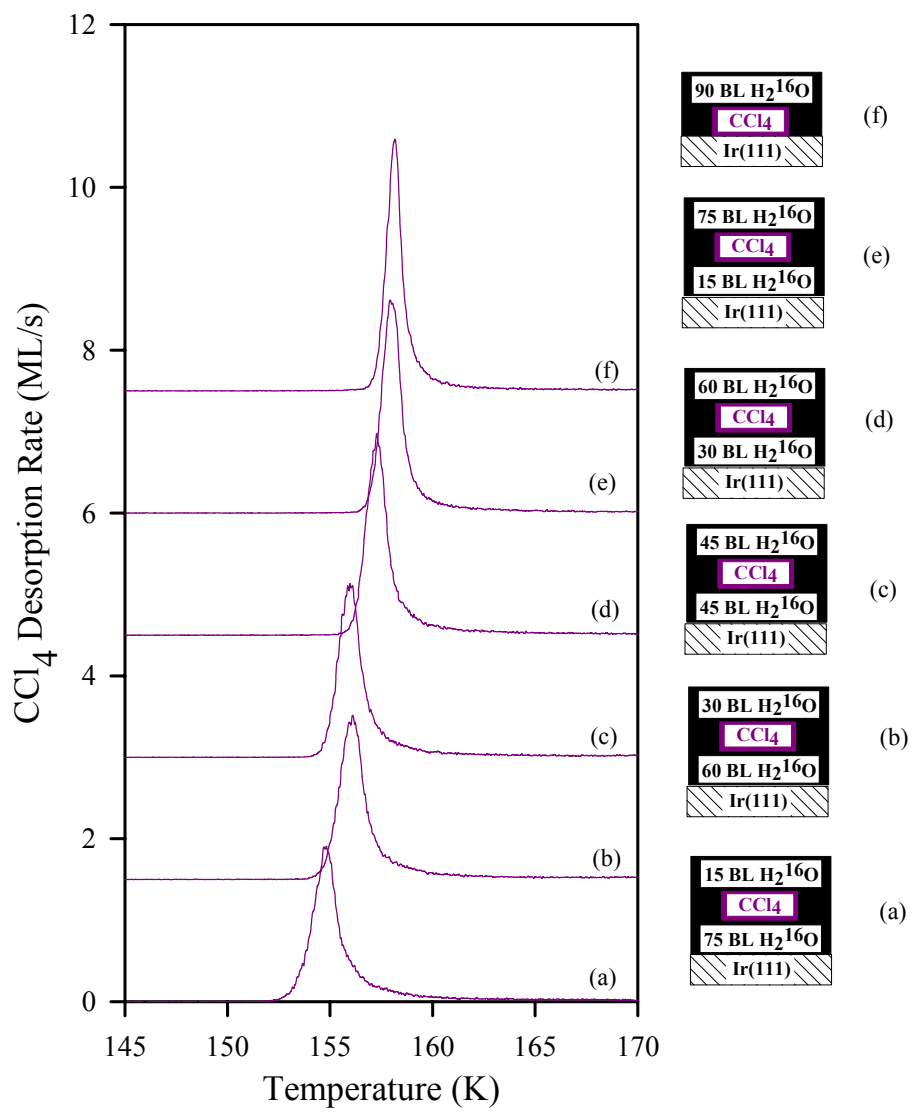
demonstrate, the deeper (further from the surface) the CCl_4 pill is located within the ASW film, the more "delayed" the abrupt CCl_4 desorption appears, shifting from T~155 K at for Fig 3.13(a) to T~158 K for Fig 3.13(f). Water desorption TPD spectra of each experiment appear virtually identical, suggesting similar crystallization kinetics in each of the structured films. Shown in Figure 3.14 are isothermal desorption experiments of structured films constructed by first dosing 5 ML of CCl_4 (beam spot covering entire sample), followed by dosing of 30 BL of ASW and annealing at the respective temperature (T ~ 144 - 152 K). These TPD spectra were annealed identically to those isothermal mixing experiments shown in Figures 3.7 and 3.8, and hence these spectra from Figures 3.7, 3.8 and 3.14 can be compared directly. As the spectra in Figure 3.14 (a)-(e) illustrate, the time and shape of the CCl_4 "volcano" desorption and hence porosity formation, is a function of anneal temperature due to its' intimate connection to crystallization of the ASW film. Isothermal anneals at higher temperatures (150 K, 152 K) give narrower and more intense CCl_4 desorption features; anneals at lower temperatures (144 K, 146 K) give much broader, less intense desorption features. $CClF_2H$ surface area measurements, such as those shown in Figure 3.8(a)-(c), exhibit greater peak surface areas for higher anneal temperatures [SA_{peak}~2.0 for T~154 K compared to SA_{peak}~1.6 for T ~ 146 K]. These trends suggest that porosity is not strictly a function of the crystallized fraction of the film, but also depends on the anneal temperature/heating schedule applied during crystallization. Upon comparison of Figure 3.12 with Figs. 3.7 and 3.8 it is also clear to see that the onset of intermixing observed in Figs. 3.7 and 3.8 and the increase in surface area of the films are coincident with the onset of porosity creation [CCl_4 desorption] for all temperatures (T ~ 146-154 K) studied. We interpret the convergence of these phenomena as lending further support to the

85

Figure 3.14. Isothermal CCl$_4$ Desorption Experiments. Shown in Figure 3.14(a)-(e) are TPD spectra of isothermal desorption experiments of films constructed by first depositing ~6 ML CCl$_4$ (black) on the Ir(111) surface, followed by deposition of 30 BL ASW H$_2^{16}$O. Structured films were then annealed isothermally at temperatures ranging from 146 K to 152 K. CCl$_4$ desorption appears concurrent with crystallization of the ASW overlayer. Heating schedules used for these anneals are identical for those used in Figure 3.6 for isothermal ASW mixing experiments; therefore these spectra can be compared directly to the mixing and surface area data of Figure 3.8, for a given temperature. For clarity, the H$_2$O desorption signal (m/z~18) is not shown in the figure; CCl$_4$ desorption appeared concurrent with ASW crystallization (and the decrease in H$_2$O desorption rate [see Figure 3.7(b)]).
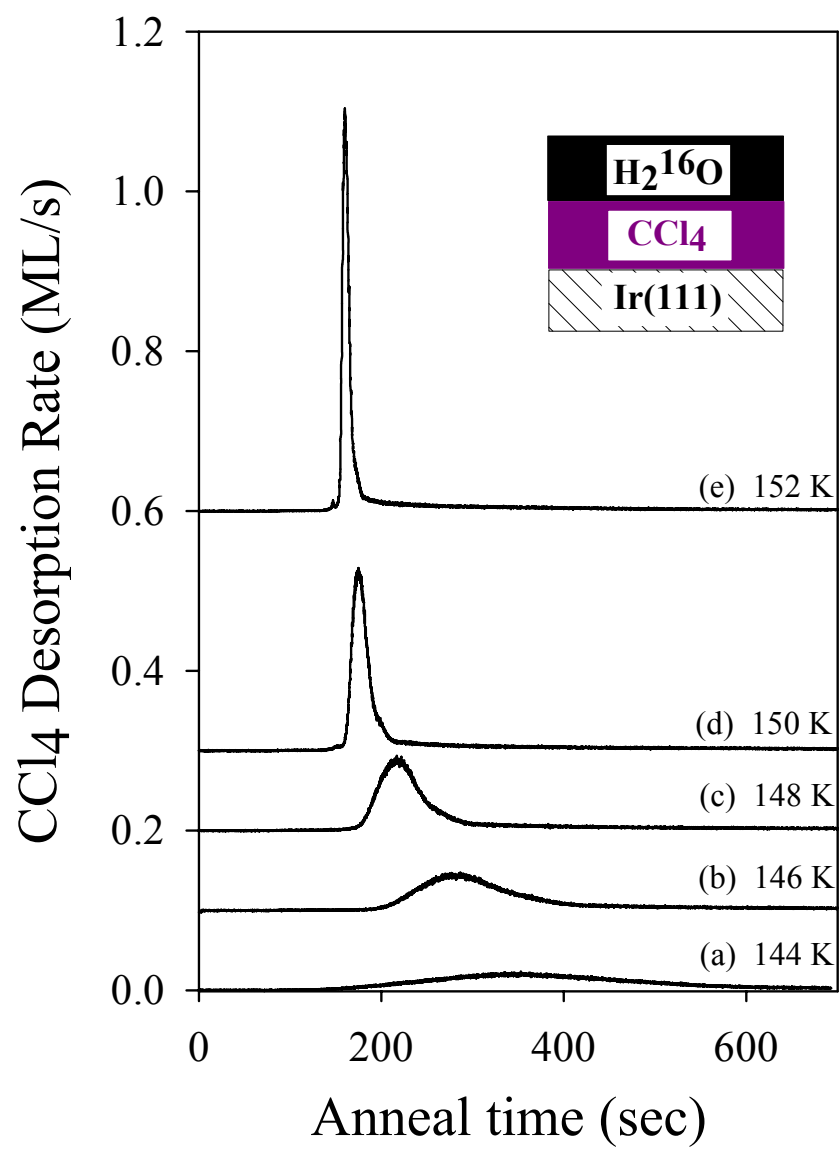
predominant role of a porous transport mechanism in the observed intermixing of these structured ASW films. Taken together, these experiments suggest that many factors play a role in dictating the formation and sintering kinetics of fractures in crystallizing ASW films. Annealing temperature, crystallization kinetics, and film thickness all appear to affect these kinetics, and hence would be expected to affect the transport kinetics of species through this interconnected network. While understanding of these factors may not yet be very quantitative, the use of CCl_4 as a 'marker' for the onset of porosity (as a function of film thickness, heating schedule, etc.) has allowed for comparison with trends in water transport. In every experiment we have conducted over the course of the present study, the onset of water transport is coincident with the onset of film fracture. In our picture of water transport along crack/fracture pathways, we envision that as voids are opened within the crystallizing film, water is able to adsorb and desorb from pore walls, moving through the film via vapor-phase transport, resulting in the observed interlayer mixing which is observed near crystallization (T ~ 154 K). Water, unlike CCl_4, has a low desorption rate at the time of film fracture, and so it will have an appreciable residence time within the crack/fracture pathways as it desorbs. Hence, water from the underlying layer does not escape as abruptly during film fracture as does CCl_4. As the films are completely crystallized and annealed further, these fractured films begin to sinter/densify as evidenced by the relative surface area measurements shown in Figure 3.8(a)-(c). Densification of the fractures and cracks would likely result in trapping of water molecules traveling through the network [as it appears to do for CCl_4 (Fig. 3.12)]. We reason this "trapped in" mixing could play an important role in the mixing which is observed after crystallization (T > 160 K) in TPD mixing experiments such as those shown in Figure 3.3 and 3.4.

88

Implications for the Glass Transition and Water Fragility

As we have argued, our data suggest that the intermixing observed in ASW films near crystallization is largely driven by transport via crystallization induced crack/fracture pathways. Consequently, this suggests that the bulk diffusivity of ASW is lower than previously thought. How "much" smaller these ASW self-diffusivity values are in magnitude is an important question with regard to water's fragility and glass transition temperature. Despite the (current) lack of a rigorous model of porosity mediated transport, we can learn more about the magnitude of the ASW self-diffusivity near T~150-160 K. While we stress the following discussion is very qualitative in nature, we do feel it is useful in illustrating the implications of our findings with respect to water's low temperature behavior. More experimental work is required in order to obtain quantitative estimates of ASW self-diffusivity at these temperatures.

Shown in Figure 3.15 is a plot of bulk diffusion coefficients for supercooled liquid water[39-41] (open squares), bulk diffusivity values obtained by Smith et. al. for ASW[25,26] (open circles), and some currently debated proposals [(i) fragile-to-strong transition (dashed line); (ii) $T_g \geq 160$ K (dotted line); as discussed in the Introduction] for water's diffusivity behavior over this temperature range. As the plot illustrates, the data of Smith et. al. fits quite nicely using the VFT equation (black solid line) to higher temperature supercooled liquid water diffusivities. [The empirical VFT equation is often used to describe the temperature dependence of diffusion behavior of glass-forming supercooled liquids[2], and has the form $D=D_o \exp (E/(T-T_o))$.] This fit has been cited as strong evidence for water's fragile nature between T~150-157 K and predicts a $D \sim 10^{-18} cm^2/s$ near T~141 K.

As mentioned earlier, the diffusion coefficient at the glass transition is typically defined to be near $D \sim 10^{-18} cm^2/s$.[2] Thus, the ASW glass transition temperature [whether it

is (i) T_g ~136 K (solid triangle) or perhaps, (ii) $T_g \geq$ 160 K (solid circle)] and the high temperature diffusivity data[39-41] can provide constraints for ASW diffusivity behavior in the "no man's land[5]" between T ~ 160 K - 230 K. In the case of (ii) [T_g > 160 K], diffusivity values near T~150-160 K would be too small to exhibit mixing on the length and timescales of our TPD experiments. This is illustrated by the dotted line shown in Figure 3.15; a VFT equation fit to higher temperature supercooled liquid data and ~10^{-18}cm^2/s at T_g ~160 K. The curve demonstrates that if $T_g \geq$ 160 K, diffusivities of the glassy ASW would likely be many orders of magnitude smaller than those expected for a liquid between T~150-160 K.

In the case of scenario (i) [T_g~136 K] the picture becomes a bit more complicated. In theory, the ASW self-diffusivity can take on a range of values near T~150-160 K consistent with D~10^{-18}cm^2/s at T_g ~136 K. While some of these self-diffusivity values would be of sufficient magnitude to allow bulk diffusive intermixing (not considering porosity-mediated transport) on the length and timescales of our experiments, other smaller diffusivity values would only allow negligible or no bulk diffusion during experiment (as is suggested experimentally by Figures 3.3 and 3.4)

With these results in mind, we can [despite the absence of a porous transport model] gain additional qualitative insights into the ASW self-diffusivity prior to crystallization by employing a simple TPD bulk diffusion model to estimate the magnitude of ASW self-diffusivity parameters in which significant bulk diffusive mixing would be observed in simulated TPD spectra. One might view these values of the self-diffusivity parameters to roughly approximate an "upper limit" to the actual ASW self diffusivity; as the data of Figure 3.3(a)-(c) suggest that little to no ASW diffusion prior to crystallization. This rough estimate can be obtained by altering the ASW self-diffusivity parameters (diffusion activation energy (E) and pre-exponential (D$_o$)) in our simple bulk

diffusion model (maintaining D~10^{-18}cm^2/s at T$_g$ ~136 K and using an Arrhenius form) and monitoring the simulated TPD spectra for interlayer bulk diffusive mixing (Figures 3.15(b) and Inset). The ASW self diffusivity values [E=70 kJ/mol; D$_o$=7.7x10^{8}cm^2/s] obtained from this exercise are shown as the dashed red line in Figure 3.15(b) Inset, and when employed in our simple bulk diffusion model (for a 30 BL on 30 BL layered ASW film), correspond to transport of ~1.9 BL of H$_2$^{18}O across the initial interface [as determined by integration of the simulated TPD spectra (see caption)]. Intermixing between the ASW layers appears noticeable during the simulated TPD spectra using these diffusion parameters, as demonstrated by the simulation results of Figure 3.15(b) (red lines).

Displayed in Figure 3.15(a) (red line) are these same ASW diffusion parameters [E=70 kJ/mol; D$_o$=7.7x10^8 cm^2/s] shown in Fig 3.15(b). As mentioned earlier, these parameters can serve as a very rough "upper limit" estimate of the actual ASW diffusivity. If the diffusivity were any greater in magnitude, we argue that greater differences should have been expected in the TPD spectra of Figure 3.3. The rough "upper limit" estimate shown in Figure 3.15(a) suggests that the actual bulk diffusivity of ASW is likely much smaller than that characteristic of a fragile liquid (open circles) between T~150-157 K. As a consequence, in order to maintain a 'smooth' connection with higher temperature supercooled liquid water diffusivity data (~242 K to 298 K) and maintain a T$_g$ ~136 K, the ASW diffusion coefficient would likely necessitate a transition from fragile to strong behavior, between T~160 K and T~231 K. This type of scenario can be envisioned by the dashed line in Figure 3.15 (Note: this line is simply for illustrative purposes). A "fragile-to-strong" transition in water diffusivity behavior has been suggested in recent theoretical work by

Figure 3.15. Implications for the ASW Self Diffusivity

Shown in Figure 3.15(a) is an Arrhenius plot [log(D) vs. 1000/T] with
literature values of supercooled liquid water diffusivities[39-41] (open
squares), ASW self diffusivity measurements of Smith and Kay[25,26] (open
circles) and a Vogel-Fulcher-Tamman (VFT) fit to both sets of data (bold
solid line).[25,26] The solid circle and solid triangle, represent a $D \sim 10^{-18} cm^2/s$ at temperatures of $T \geq 160$ K and $T \sim 136$ K, respectively. These
points represent the "typical" diffusivity values at the glass transition
temperature[2], for both the $T_g \sim 136$ K and $T_g \geq 160$ K possibilities discussed
in the text. Shown as the dotted line in Figure 3.15(a) is a VFT fit of the
supercooled liquid data to $D_o = 10^{-18}$ cm^2/s at $T_g \sim 160$ K. This trace serves
to illustrate that if water's glass transition is at $T_g \geq 160$ K, ASW self-
diffusivities will take on extremely small values prior to crystallization.
Shown as the red solid line are values (as discussed in Figure 3.15 (b) and
3.15(b) Inset caption) of the ASW diffusivity which exhibit noticeable
interlayer mixing. As discussed in the text, this rough "upper limit"
estimate suggests that the actual ASW self-diffusivity is likely much lower
than previously thought, especially near $T \sim 157$ K. This implies that if
$T_g \sim 136$ K, our experimental observations would be consistent with a
change in from "fragile" to "strong" behavior of water diffusivity between
$T \sim 160$ K and $T \sim 231$ K. Such a scenario is suggested by the (green dash)
line shown in Figure 3.15(a) *for illustrative purposes*.

Figure 3.15(b) and 3.15(b) Inset. Displayed in Figures 3.15(b) and Inset
is a demonstration of how the red line shown in Figure 3.15(a) was

determined using our simple bulk diffusion model. If the glass transition of water is $T_g \sim 136$ K, its' self-diffusivity can take on various magnitudes; our aim is to determine the ASW self diffusivity parameters [using our simple bulk diffusion model] in which substantial mixing should be observed on the length- and timescales of our experiments [and hence significant differences should have been seen in the experiments of Figure 3.3(a)-(c)]. To obtain this estimate, ASW self-diffusion parameters were systematically varied, as shown in of Fig. 3.15(b), maintaining $D \sim 10^{-18}$ cm^2/s at $T_g \sim 136$ K. These parameters were used to calculate simulated TPD mixing experiments (for ~ 30BL $H_2^{16}O$ on ~ 30 BL $H_2^{18}O$ at 0.6 K/s) using our simple bulk diffusion TPD model, monitoring the extent of mixing in the simulated TPD results. Our simple bulk diffusion model simulates TPD mixing experiments in which **bulk** diffusion only mode of transport between the layered films. As Figure 3.15(b) demonstrates, as the ASW diffusivity parameters are increased [from $D \sim 10^{-18} cm^2/s$; (black line in Fig 3.15(b) Inset) to $D_o = 7.7 \times 10^8$ cm^2/s, E=70 kJ/mol (red line in Fig 3.15(b) Inset)], increased diffusive mixing is observed in the corresponding simulated TPD spectra. [Dotted lines in Figure 15(b) Inset show "intermediate" diffusivity values, and hence show "intermediate" amounts of mixing in the simulated TPD spectra (Dotted lines) in Figure 15(b)]. ASW diffusivity values defined by the red line result in transport of ~1.9 BL across the initial interface of the labeled ASW films.

(a) Diffusivity (cm²/s) vs 1000/T (K)

(b) Desorption Rate (BL/s) and D(cm2/s) vs T(K) with Inset
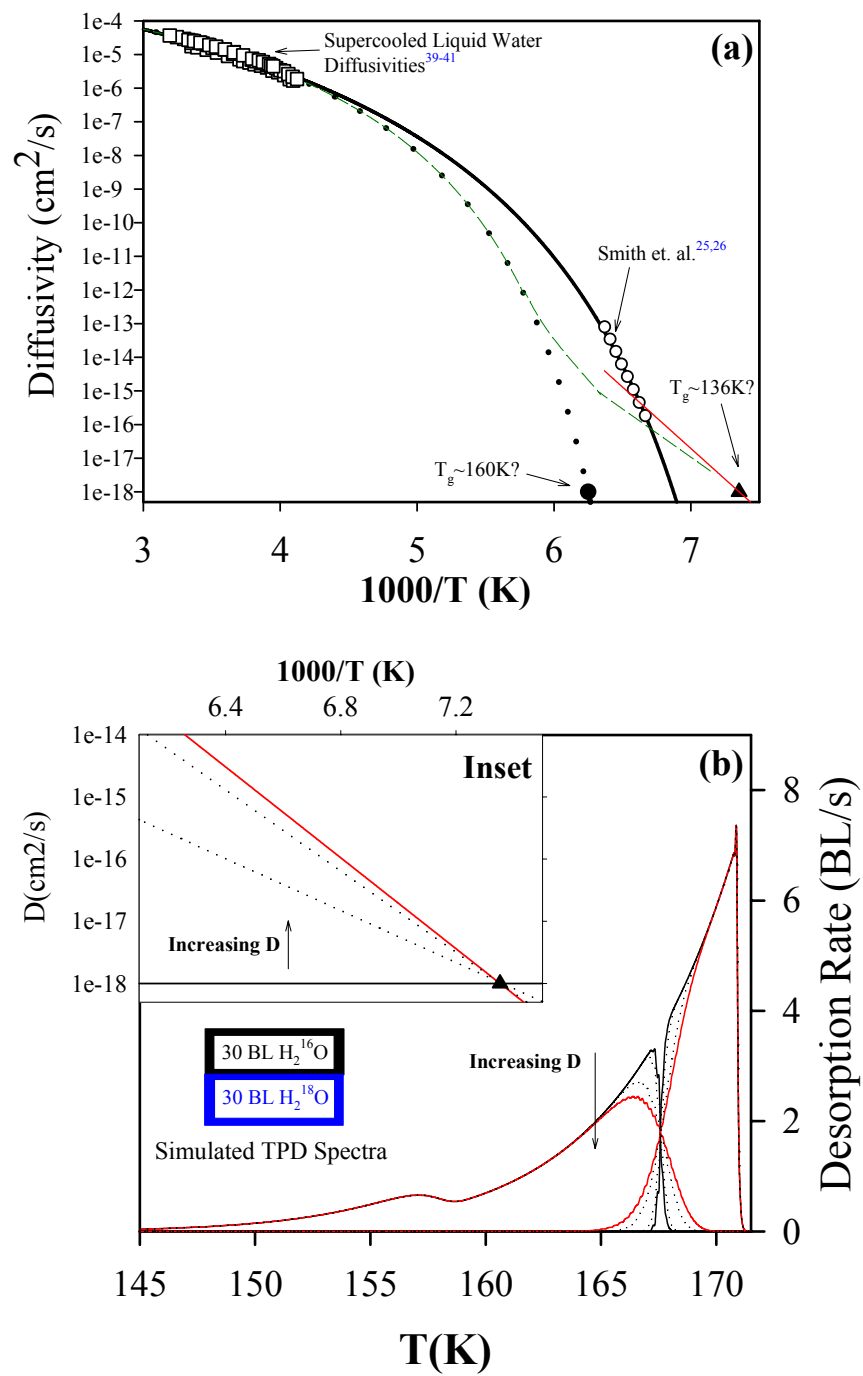
Starr et. al.[50,51] and Truskett et. al.[93,94] Thus, if water's T_g ~136 K, our experimental results seem more consistent with a fragile-to-strong transition in water diffusivity rather than continuous, fragile behavior from higher temperatures (T > 231 K).

Clearly, the analysis of Figure 3.15 is a simplified attempt to gain some further insights into the behavior of ASW self-diffusivity at low temperatures. While this exercise has its shortcomings, we have found that performing this same analysis (of Figure 3.15) using a different value of the glass transition (T_g~141 K) or using a different value of the diffusivity at T_g ~ 136 K (D~10^{-20} cm^2/s), produces a similar picture; i.e. ASW diffusivity values that are much smaller than those characteristic of a 'fragile' liquid between prior to crystallization.

One possible objection to our analysis lies in the observation that the CCl_4 diffusion barrier layer only remains between the ASW films in Figure 3.3 until T~155 K; once the ASW film has fractured (T~155 K) in Figure 3.3(a)-(c), the CCl_4 can desorb, removing the barrier layer from the interface. The CCl_4 escapes at a temperature in which a portion of the film still remains amorphous; as such, one could argue that bulk diffusive mixing could still occur between T~155 K and T~159 K (temperature at which film is completely crystallized). However, this argument is inconsistent with the experimental results of Figure 3.5, which show substantial mixing in structured films over a wide range of crystallization timescales and temperatures (T~150-160 K). Likewise, this argument would also ignore the remarkable similarity of the TPD spectra of Figure 3.3(a)-(c) despite the CCl_4 barrier layer remaining in the film between T~77 K to 155 K.

It should also be reiterated that the above exercise is dependent on the assertion that the CCl_4 multilayers would provide an effective barrier to ASW bulk diffusion (if it were to occur) between isotopically labeled ASW layers between T ~ 77 K to 155 K. As

such, it is useful to review our support for this claim. The MeOH experiments of Figures 3.10 and 3.11 suggest that CCl_4 barrier layers, at least 15 ML thick, provide an effective barrier to MeOH transport in ASW (i.e., MeOH desorption is not observed until desorption ("volcano") of CCl_4 barrier layer during crystallization). MeOH transport in experiments with thicker barrier layers (30 ML or above) show identical MeOH desorption traces, suggesting that in these structures the limiting factor for MeOH transport is removal of the CCl_4 barrier layer during crystallization. Additionally, H_2O mixing experiments such as those shown in Figure 3.1, conducted with different barrier materials (such as $CHCl_3$), exhibit behavior similar to experiments conducted with CCl_4; this appears to be inconsistent with water "diffusing" through the barrier layer, as one might expect a dependence of mixing on barrier layer material. The observation of the CCl_4 molecular volcano[77] phenomena also suggests that CCl_4 does not intermix well with ASW; as the CCl_4 remains well "capped" below the ASW films until crystallization. We interpret these observations to suggest that CCl_4 should provide an effective bulk diffusion barrier between labeled water layers. If, on the other hand, H_2O is able to move freely through the CCl_4 barrier layer then our conclusions regarding the experiments of Figures 3.3 and 3.4 and our conclusions regarding Figure 3.15 would need to be revisited. However, we believe the available experimental evidence and observations are inconsistent with such a view.

As mentioned in the discussion of Figure 3.3, very slight differences in water mixing spectra TPDs (such as those shown in Figure 3.3 and 3.4) do occur for structured films containing very thick CCl_4 films. These slight differences occur in the TPD spectra after T ~ 157 K. It is not clear what effect very thick CCl_4 barrier layers may have on crack/fracture formation and/or concurrent water transport within the structured ASW films. Additional experiments (not shown) with extremely thick CCl_4 barrier layers (~ 90

ML CCl_4) also show slight differences in mixing after T~157 K, but remarkably, exhibit the same qualitative behavior (substantial mixing occurring during crystallization). It seems possible that very thick (greater than 30 ML) CCl_4 barrier films could influence such phenomena and contribute to differences in the observed TPD spectra. However, even if we assume that these slight differences in the TPD spectra are due to "blocked" bulk diffusion, the diffusion values shown by the red line [which are still significantly smaller than "fragile" diffusivity values] would likely account for such slight differences in the TPD measurements. The primary message of Figure 3.15 is that the actual self-diffusivity of ASW is likely too small to be considered "fragile" in nature while maintaining a T_g~136 K.

In short, we interpret our measurements to suggest that ASW does not exhibit diffusion behavior typical of a fragile liquid prior to crystallization (T ~ 160 K). Rather, our results appear to be more consistent with ASW diffusivities being characteristic of a strong liquid or glass prior to 160 K. As stated earlier, more work remains with regards to obtaining more precise, quantitative values of ASW self-diffusion coefficient prior to crystallization. Attaining such quantitative values using desorption techniques on ASW thin films will likely require measurements which allow significant mixing to occur between ASW films prior to crystallization (and hence porosity formation); i.e. long mixing times at very low temperatures. However, with the temperature control issues surrounding such lengthy experiments on our apparatus, these measurements would likely have significant errors which would preclude quantitative comment on diffusivity values. One promising avenue of research involves reducing crack/fracture formation in ASW films via the addition of a dilute amount of solute to the film. Current work[95] in our laboratory with dilute HNO_3 films (less than 2 mol % HNO_3 in H_2O) suggests that the presence of HNO_3 reduces the amount of crack/fracture formation in ASW films during

97

crystallization. These experiments may provide the opportunity to study bulk diffusive mixing in films where crack formation has been reduced at timescales and temperatures with suitable temperature control. Preliminary results from layered TPD mixing experiments (such as those shown in Figure 3.3), using $H_2^{18}O$ and HNO_3-doped $H_2^{16}O$ exhibit substantially less mixing in thin HNO_3 films where porosity has been reduced. These results appear to be consistent with the findings of the present study.

Figure 3.15 also helps to illustrate that, while our data suggests ASW is not a fragile liquid at low temperatures, whether ASW is a "strong" liquid with $T_g\sim136$ K [undergoing a fragile-to-strong transition between T $\sim$ 160-230 K] or whether water remains a glass prior to crystallization [perhaps at $T_g\sim160$-165 K suggested by other investigators] remains an open question. Since both of these scenarios would exhibit negligible bulk diffusion in our experiments prior to crystallization, each scenario would be consistent with our experimental data.

Conclusions

In summary, we have studied transport processes in nanoscale amorphous solid water (ASW) films to gain insight into the nature of water's glass transition and fragility at temperatures prior to crystallization to crystalline ice (CI) (T $\sim$ 150 - 160 K). We conclude that transport through an interconnected porous network created in ASW films during crystallization is the predominate cause of the intermixing observed near (150-160 K) as evidenced by:

(1)   Similarity of mixing which occurs in structured films with *and* without CCl₄ diffusion barrier layers (Figures 3.3 and 3.4) [and corresponding MeOH probe experiments   (Figures 3.9-3.11)]

(2)   Non-monotonic behavior of the desorption ratio (r_{18}/r_{16}) during desorption of structured ASW films, behavior which is fundamentally inconsistent with a bulk diffusion mechanism (Figure 3.1(b) and Figure 3.3(a) Inset)

(3)   Onset of intermixing concurrent with porosity formation regardless of heating schedule used in our experiments (Figures 3.5 and 3.8)

(4)   Isothermal mixing experiments exhibit intermixing concurrent with increase in surface area due to crack/fracture of the ASW film (Figures 3.7 and 3.8)

Since porous transport appears to be the predominate mode of transport within ASW films, this suggests the bulk diffusivity of ASW is much smaller than previously thought.   Thus, we conclude that ASW is likely not a 'fragile' liquid prior to crystallization below 160 K.   Our data is consistent with two possible scenarios for the nature of ASW diffusivity at low temperatures: either,   (i) ASW exhibits diffusivity characteristic of a 'strong' liquid with a glass transition temperature of T_g~136 K, undergoing a fragile-to-strong transition in diffusion behavior above 160 K, or (ii) ASW remains a rigid glass with a T_g greater than 160 K.

References

1. P. G. Debenedetti, J. Phys. Cond. Matt. **15**, R1669 (2003)

2. P. G. Debenedetti, *Metastable Liquids: Concepts and Principles* (Princeton University Press, Princeton, NJ, 1996).

3. C. A. Angell, Chem. Rev. **102**, 2627 (2002)

4. C. A. Angell, Annu. Rev. Phys. Chem. **55**, 559 (2004)

5. O. Mishima, H. E. Stanley, Nature **396**, 329 (1998)

6. C. A. Angell, Science **267**, 1924 (1995)

7. P. G. Debenedetti, F. H. Stillinger, Nature, 410, 259 (2001)

8. E. F. Burton, W. F. Oliver, Proc. Roy. Soc. Lond. A. **153**, 166 (1935)

9. J. A. McMillan, S. C. Los, Nature **206**, 806 (1965)

10. M. Sugisaki, H. Suga, S. Seki, J. Chem. Soc. Jpn. **41**, 2591 (1968)

11. A. Hallbrucker, E. Mayer, G. P. Johari, J. Phys. Chem. **93**, 4986 (1989)

12. G. P. Johari, A. Hallbrucker, E. Mayer, Nature **330**, 552 (1987)

13. I. Kohl, L. Bachmann, A. Hallbrucker, E. Mayer, T. Loerting, Phys. Chem. Chem. Phys. **7**, 3210 (2005)

14. G. P. Johari, J. Chem. Phys. **119**, 2935 (2003)

15. G. P. Johari, J. Chem. Phys. B. **107**, 9063 (2003)

16. I. Kohl, L. Bachmann, E. Mayer, A. Hallbrucker, T. Loerting, Nature **435**, E1 (2005)

17. G. P. Johari, J. Chem. Phys. **116**, 8067 (2002)

18. G. P. Johari, J. Phys. Chem. B. **102**, 4711 (1998)

19. G. P. Johari, J. Chem. Phys. **123**, 016102 (2005)

20. G. P. Johari, J. Chem. Phys. **122**, 144508 (2005)

21. G. P. Johari, A. Hallbrucker, E. Mayer, J. Chem. Phys. **97**, 5851, (1992)

22. G. P. Johari, A. Hallbrucker, E. Mayer, J. Chem. Phys. **95**, 2955 (1991)

23. G. P. Johari, Phys. Chem. Chem. Phys. **7**, 1091 (2005)

24. D. R. MacFarlane, C. A. Angell, J. Phys. Chem. **88**, 759 (1984)

25. R. S. Smith, B. D. Kay, Nature **398**, 788 (1999)

26. R. S. Smith, Z. Dohnálek, G. A. Kimmel, K. P. Stevenson, B. D. Kay, Chem. Phys. **258**, 291 (2000)

27. R. Souda, Chem. Phys. Lett. **415**, 146 (2005)

28. R. Souda, Phys. Rev. Lett. **93**, 235502/1, (2004)

29. A. Minoguchi, R. Richert, C. A. Angell, J. Phys. Chem. B. **108**, 19825 (2004)

30. S. Cerveny, G. A. Schwartz, R. Bergman, J. Swenson, Phys. Rev. Lett. **93**, 245702/1 (2004)

31. A. Minoguchi, R. Richert, C. A. Angell, Phys. Rev. Lett. **93**, 215703-1 (2004)

32. M. Fisher, J. P. Devlin, J. Phys. Chem. **99**, 11584 (1995)

33. J. A. Ghormley, J. Chem. Phys. **48**, 503 (1968)

34. Y. Yue, C. A. Angell, Nature **427**, 717 (2004)

35. V. Velikov, S. Borick, C. A. Angell, Science **294**, 2335 (2001)

36. Y. Yue, C. A. Angell, Nature **435**, E2 (2005)

37. A. A. Tsekouras, M. J. Iedema, J. P. Cowin, Phys. Rev. Lett. **80**, 5798 (1998)

38. D. Bertolini, M. Cassettari, G. Salvetti, J. Chem. Phys. **76**, 3285 (1982)

39. K. T. Gillen, D. C. Douglass, M. J. R. Hoch, J. Chem. Phys. **57**, 5117 (1972)

40. W. S. Price, H. Ide, Y. Arata, O. Söderman, J. Phys. Chem. B. **104**, 5874 (2000)

41. H. R. Pruppacher, J. Chem. Phys. **56**, 101 (1972)

42. K. Ito, C. T. Moynihan, C. A. Angell, Nature **398**, 492 (1999)

43. C. A. Angell, J. Phys. Chem. **97**, 6339 (1993)

44. P. Jenniskens, D. F. Blake, Astro. J. **473**, 1104 (1996)

45. F. Sciortino, P. Gallo, P. Tartaglia, H.-S. Chen, Phys. Rev. E. **54**, 6331 (1996)

46. F. Sciortino, L. Fabbian, H.-S. Chen, P. Tartaglia, Phys. Rev. E. **56**, 5937 (1997)

47. P. Gallo, F. Sciortino, P. Tartaglia, S-.H. Chen, Phys. Rev. Lett. **76**, 2730 (1996)

48. F. W. Starr, S. Harrington, F. Sciortino, H. E. Stanley, Phys. Rev. Lett. **82**, 3629 (1999)

49. F. W. Starr, F. Sciortino, H. E. Stanley, Phys. Rev. E. **60**, 6757 (1999)

50. F. W. Starr, C. A. Angell, H. E. Stanley, Physica A. **323**, 51 (2003)

51. F. W. Starr, C. A. Angell, E. La Nave, S. Sastry, F. Sciortino, H. E. Stanley, Biophys. Chem. **105**, 573 (2003)

52. L. Xu, P. Kumar, S. V. Buldyrev, S.-H. Chen, P. H. Poole, F. Sciortino, H. E. Stanley, Proc. Nat. Acad. Sci. **102**, 16558 (2005)

53. I. Saika-Voivod, P. H. Poole, F.Sciortino, Nature **412**, 514 (2001)

54. M. Hemmati, C. T. Moynihan, C. A. Angell, J. Chem. Phys. **115**, 6663 (2001)

55. A. Faraone, L. Liu, C.-Y. Mou, C.-W. Yen, S.-H. Chen, J. Chem. Phys. **121**, 10843 (2004)

56. L. Liu, S.-H. Chen, A. Faraone, C.-W. Yen, C.-Y. Mou, Phys. Rev. Lett. **95**, 117802/1 (2005)

57. R. Bergman, J. Swenson, Nature, **403**, 283 (2000)

58. J. Swenson, J. Phys. Cond. Matt. **16**, S5317 (2004)

59. D. Patschek, A. Geiger, J. Phys. Chem. B. **103**, 4139 (1999)

60. G. P. Johari, J. Chem. Phys. **105**, 7079 (1996)

61 J.E. Davis, S.G. Karseboom, P.D. Nolan, C.B. Mullins, J. Chem Phys. **105**, 8362 (1996)

62. N. F. Ramsey, *Molecular Beams*, Cambridge Univ. Press (1960)

63. O. Andersson, H. Suga, Phys. Rev. B **65,** 140201 (2002)

64. Z. Dohnalek, G. A. Kimmel, P. Ayotte, R. S. Smith, B. D. Kay, J. Chem. Phys. **118**, 364 (2003)

65. G. A. Kimmel, K. P. Stevenson, Z. Dohnálek, R. S. Smith, B. D. Kay, J. Chem. Phys. **114**, 5284 (2001)

66. Z. Dohnálek, G. A. Kimmel, P. Ayotte, R. S. Smith, B. D. Kay, J. Chem. Phys. **118**, 364 (2003)

67. K. P. Stevenson, G. A. Kimmel, Z. Dohnálek, R. S. Smith, B. D. Kay, Science **283**, 1505 (1999)

68. G. A. Kimmel, Z. Dohnálek, K. P. Stevenson, R. S. Smith, B. D. Kay, J. Chem. Phys. **114**, 5295 (2001)

69. D. E. Brown, S. M. George, J. Phys. Chem. **100**, 15460 (1996)

70. P. A. Thiel, T. E. Madey, Surf. Sci. Rep. **7**, 211 (1987)

71. D. A. King, M. G. Wells, Proc. R. Soc. London Ser. A. **339**, 245 (1974)

72. D. J. Safarik, R. J. Meyer, C. B. Mullins, J. Vac. Sci. Technol. A. **19**, 1537 (2001)

73. D. J. Safarik, R. J. Meyer, C. B. Mullins, J. Chem. Phys. **118**, 4660 (2003)

74. Z. Dohnálek, G. A. Kimmel, R. L. Ciolli, K. P. Stevenson, R. S. Smith, B. D. Kay, J. Chem. Phys. **112**, 5932 (2000)

75. R. J. Speedy, P. G. Debenedetti, R. S. Smith, C. Huang, B. D. Kay, J. Chem. Phys. **105**, 240 (1996)

76. K. Goto, T. Hondoh, A. Higashi, Jpn J. Appl. Phys. **25**, 351 (1986)

77. R. S. Smith, C. Huang, E. K. L. Wong, B.D. Kay, Phys. Rev. Lett. **79**, 909 (1997)

    105, 240 (1996)

78. N. J. Sack, R. A. Baragiola, Phys. Rev. B.: Cond. Matt. **48**, 9973 (1993)

79. P. Ayotte, R. S. Smith, K. P. Stevenson, G. A. Kimmel, B. D. Kay, J. Geo. Research [Planets], **106**, E12 33387 (2001)

80. J. L. Blanchard, J. T. Roberts, Langmuir **10**, 3303 (1994)

81. J. M. K. Donev, Q. Yu, B. R. Long, R. K. Bollinger, S. C. Fain Jr., J. Chem. Phys. **123**, 044706/1 (2005)

82. P. Jenniskens, S. F. Banham, D. F. Blake, M. R. S. Mccoustra, J. Chem. Phys. **107**, 1232 (1997)

83 J. A. Ghormley, C. J. Hochanadel, Science **171**, 62 (1971)

84. M. S. Westley, G. A. Baratta, R. A. Baragiola, J. Chem. Phys. **108**, 3321 (1998)

85. G. A. Kimmel, N. G. Petrik, Z. Dohnálek, B. D. Kay, Phys. Rev. Lett. **95**, 166102 (2005)

86. Since we are measuring uptake and adsorption of $CClF_2H$ on *porous* ASW films, condensation of *multilayer* $CClF_2H$ can in theory occur at temperatures below T ~ 86.5 K in pores with exceedingly small radii, as described by the Kelvin equation. Hence, our $CClF_2H$ "surface area" measurements [as we refer to them through the manuscript] are a measure of both the increased surface area for monolayer adsorption (large pores) and multilayer condensation occurring in small pores formed in the film during crystallization.

87. P. Löfgren, P. Ahlström, D. V. Chakarov, J. Lausmaa, B. Kasemo, Surf. Sci. **367**, L19 (1996)

88. R. S. Smith, C. Huang, E. K. L. Wong, B. D. Kay, Surf. Sci. **367**, L13 (1996)

89. F. E. Livingston, J. A. Smith, J. Phys. Chem. A. **106**, 6309 (2002)

90. G. A. Miller, D. A. Carpenter, J. Chem. Eng. Data **9**, 371 (1964)

91. P. Adler, *Porous Media: Geometry and Transports* (Butterworth-Heinemann, Stoneham, MA, 1992)

92. E. A. Mason, A. P. Malinauskas, *Gas Transport in Porous Media: The Dusty-Gas Model* (Elsevier Science Publishers, Amsterdam, The Netherlands, 1983)

93. T. M. Truskett, K. A. Dill, J. Phys. Chem. B. **106**, 11829 (2002)

94. T. M. Truskett, K. A. Dill, Biophys. Chem. **105**, 447 (2003)

95. S. M. McClure, E. Barlow, M. Akin, D. J. Safarik, T. M. Truskett, C. B Mullins, *in preparation*

Chapter 4: Effect of Nitric Acid on Crystallization-Induced Fracture in Amorphous Solid Water Films

Introduction

The nature and properties of amorphous solid water (ASW) have important implications in the fields of astrophysics/astrochemistry[1-10], cryobiology[11], and in understanding the behavior of supercooled liquid water[12]. Recent work, led by Kay and coworkers, have illustrated the utility in studying vapor deposited, glassy films of water under UHV conditions to gain information on crystallization kinetics[13-16], transport[17,18], thermodynamic[19], and structural properties[20-24] of ASW. Several studies[20,24,25] have shown that glassy water, upon crystallization, can undergo significant structural and morphological changes. Investigations by Smith et. al.[20] have illustrated that nanoscale thin films of ASW can crack/fracture upon heating and subsequent crystallization to crystalline ice (CI), between 155-160 K depending upon thermal histories. It is hypothesized that, upon crystallization, grain-grain impingement and/or density differences between ASW and CI generate stresses within the ASW films which lead to film cracking and fracturing. [Internally generated stresses are also thought to occur during nucleation and growth in thin amorphous Si films (thickness ~550 nm) when annealed to form polycrystalline Si[26,27]]. This cracking phenomenon is believed to create an interconnected porous network which has been shown experimentally to serve as a pathway for vapor phase transport of underlying molecules (CCl_4, Ar, O_2, N_2, CH_4).[20,28,29] Evidence[13,15] also suggests that further crystallization and annealing of such films results in subsequent densification and collapse of the interconnected network, eliminating fracture pathways for vapor phase transport. Additional support for structural change in ASW thin films during crystallization has come from recent AFM measurements

conducted by Donev et. al.[24], optical measurements by Baragiola et. al.[30], TOF-SIMS/TPD measurements by Souda et. al.[31,32], and measurements of surface area of crystallizing ASW films.[13,14] On a larger scale, crack formation in ASW is also believed to have implications for astrophysics and astrochemistry. It has been hypothesized that fracture formation due to phase transitions in ASW (LDA to HDA[1-2] and/or crystallization of ASW[3-5]) may explain the abrupt off-gassing of volatile materials in interstellar cometary bodies (believed to contain ASW[6-8]).

Smith and Kay[17,18] have studied transport properties of ASW employing nanoscale films grown via molecular beam. By constructing isotopically labeled, structured ASW films (e.g. an $H_2{}^{16}O$ ASW layer deposited on top of an $H_2{}^{18}O$ ASW layer), interlayer mixing between the films was monitored via thermal desorption spectroscopy (TDS). They interpreted the intermixing as *bulk* diffusion, and self-diffusivity parameters were extracted from these novel experiments, lending support for water's fragile nature at low temperatures (T ~ 150-160 K). However, recent studies[33] in our laboratory have suggested that the water intermixing observed in these thin, labeled ($H_2{}^{16}O$, $H_2{}^{18}O$) ASW films occurs during crystallization and is not due to bulk diffusion. Rather, our results suggest that the observed mixing is predominantly due to transport through the high conductance crack/fracture pathways which are generated as a result of the ASW to CI phase transition. These results are consistent with the idea that bulk diffusion in ASW is negligible prior to crystallization, arguing that ASW is either a (i) strong liquid or (ii) a glass below T~160 K. Further insights on this issue could be gained if cracking or fracturing could somehow be eliminated in crystallizing ASW films. This would allow for further experimental study of relevant transport mechanisms in ASW thin films prior to crystallization, enabling comparison of TPD mixing experiments where

106

crack/fracture formation is prevalent with experiments where crack/fracture pathways have been reduced.

A wealth of experimental evidence (with the following references by no means exhaustive) suggests that ions can affect the hydrogen bonding network of glassy and liquid water phases. [However, whether the effects of ions are long range (translated across many water molecules) or short range (localized near the 1st solvation shell) remains a subject of current debate.[34-36]] It has been known for some time that ions (acids, bases and salts) can affect the viscosity of aqueous solutions.[37,38] This has led to the qualitative characterization of certain ions as "structure makers" and others as "structure breakers", presumably based on their ability to influence solution viscosity via ordering or disordering the hydrogen bonding structure of liquid water. Recent work has suggested that the presence of solutes can also alter water's hydrogen bond network similar to the effects of increased pressure. The experimentally observed increase in supercooled liquid water mobility (diffusivity)[39,40] upon application of pressure is thought to arise from the disruption of the tetrahedral hydrogen bonding network of water induced by the increased pressure.[41,42] Neutron diffraction measurements on concentrated aqueous salt (NaCl, Na_2SO_4, NH_4Cl)[35], acid (HCl)[91], and base (NaOH)[92] solutions have been offered as evidence that the presence of solutes can alter water's hydrogen bonding network, similar to the effects of pressure. NMR measurements[46,47] have also shown that the application of pressure can increase supercooled liquid water mobility; at low temperatures and pressures the presence of solutes can also increase water mobility. An interesting study by Koop et. al.[48] suggests that the homogenous nucleation of ice from a wide range of supercooled aqueous solutions can be well described by the solution activity and/or the applied pressure, suggesting that solutions freeze and melt when their hydrogen bonding networks are equivalent. Experimental

107

work by Hofer et. al.[49] and Angell et. al.[50,51] have shown that *glassy* solids formed from aqueous solutions of various salts exhibit composition dependent changes in their observed glass transition[49,50] and homogenous nucleation temperatures[51]. Studies by Satoh et. al.[52] suggest that glassy phases of HNO_3-H_2O exhibit interesting crystallization behavior near 54 wt % HNO_3 (composition corresponding to the HNO_3-$3H_2O$ hydrate species), exhibiting an essentially monotonic variation of T_g with HNO_3 concentration at higher HNO_3 concentrations (35 - 62 wt % HNO_3). Since cracking and fracturing of crystallizing ASW films appears to be intimately linked to the amorphous to crystalline transformation, we are motivated to investigate whether the presence of ions (with their possible effects on hydrogen bonding, mobility, and nucleation/growth of crystalline ice within the amorphous film) can affect the cracking/fracture of thin ASW films during crystallization.

Here we present results from an investigation of crystallization-induced film fracture in nanoscale (~ 30-90 BL) ASW films containing dilute amounts of nitric acid, HNO_3 (x_{HNO_3} ~0-2.2 mol %). We choose nitric acid, HNO_3, as a candidate molecule for several reasons. First, its' vapor phase concentration[53] is sufficient to allow for molecular beam deposition of dilute amorphous films of desired composition (x_{HNO_3} ~ 0-2.2 mol %). Secondly, a large body of research exists regarding nitric acid crystalline and amorphous phases. Infrared studies of thin films[54] of glassy and crystalline HNO_3/H_2O phases, Ar matrices[55], and thin liquid films of aqueous HNO_3 [56] suggest that in dilute solutions, nitric acid resides in its' ionic form (H_2O:HNO_3 mole ratios greater than 2-4[54,55,57] to stabilize the ionic species'; perhaps as high as H_2O:HNO_3 = 12 for *complete* HNO_3 ionization[56]). At higher concentrations, molecular HNO_3 can exist in hydrated complexes (mono- and tri- hydrates; referred to as NAM and NAT, respectively). Since we are working with thin films under much more dilute environments (H_2O:HNO_3 > 50),

we would expect HNO_3 present in our films to be primarily ionic in nature as well. Thirdly, vapor deposition (both co-condensation of H_2O and pure HNO_3 vapors[58-64] and condensation of HNO_3(aq) solution vapors[54,65-68]) has been employed successfully by numerous investigators to study properties of thin films composed of HNO_3 and ice. The results of the present study demonstrate that small amounts of HNO_3 doped within ASW films ($x_{HNO_3} < 2.2$ mol %) can significantly reduce fracture formation in the crystallizing ASW films. Using these dilute acid films, we have conducted initial investigations of intermixing between isotopically labeled films of $H_2^{18}O$ and HNO_3 doped ASW ($H_2^{16}O$) films, structures where we expect film fracture to be, at the very least, reduced in magnitude. These results are consistent with our previous findings[33]; namely, that porosity mediated transport of H_2O through crystallization induced fracture pathways plays an important role in the observed self-transport of water molecules in thin ASW films prior to crystallization (T~150-160 K)

Experimental

Experiments were conducted in an ultrahigh vacuum (UHV)/molecular beam chamber equipped with quadrupole mass spectrometry (QMS), low energy electron diffraction (LEED), Auger electron spectroscopy (AES), and temperature programmed desorption (TPD) capabilities, described previously.[69] Nanoscale films of ASW, dilute HNO_3 films (deposition rates of ~0.1-0.2 BL H_2O/sec) and CCl_4 (~0.05 ML/sec) are grown at normal incidence on an Ir(111) single crystal substrate at T~77 K. Deposition under these conditions has been shown to produce dense, non-porous ASW films.[23,30] Quasi-effusive (Nozzle diameter, d~1 mm; Knudsen number, K_n~0.05) molecular beams were formed in a newly designed stainless steel, multi-nozzle assembly which allows separate, independent dosing of $H_2^{16}O$, $H_2^{18}O$, and dilute HNO_3 films. Beam spots for water and dilute nitric acid films have been defined larger than the Ir(111) sample, thus

109

providing a uniform flux of vapor across the entire Ir(111) substrate[70]; CCl_4 is deposited using a beam spot smaller than the sample, such that the entire CCl_4 beam spot resides entirely on the Ir(111) substrate.

Distilled, deionized water ($H_2^{16}O$, VWR Scientific; $H_2^{18}O$, Isotec 95 atom %)), CCl_4, and aqueous nitric acid solutions (prepared with Mallinckrodt, 69 wt % stock solution) employed for film growth were thoroughly degassed prior to use. Films of desired HNO_3 concentrations (concentrations reported in mol %; [moles of HNO_3]/[moles HNO_3 and H_2O] x 100%) were achieved by creating the appropriate liquid solution composition to create the desired beam composition (assuming an effusive beam source) according to literature vapor liquid equilibrium data.[53] During the course of our studies, we found that nitric acid concentrations in the very dilute beams were extremely sensitive to nozzle conditions and nitric acid solution history. Even the length of the nozzle assembly plumbing was observed to effect HNO_3 beam concentrations, as the stainless steel tubing appeared to be an effective "getter" for HNO_3 in the dilute beams. As a consequence of such experimental issues, the following protocol for experiments was developed. All experiments were conducted with the *exact* same nozzle assembly and plumbing (all stainless steel tubing, components, and gaskets). Prior to each days' experimentation, nitric acid/water vapor was allowed to flow through the nozzle assembly for approximately 1 hour, allowing for passivation of nozzle surfaces. After this initial passivation, nitric acid/water beam were run for *at least ~20 min* (under dosing conditions) prior to each film growth, to ensure nozzle passivation and beam equilibration. This process allowed for consistent HNO_3 concentrations within the beam as determined by consistency of the TPD spectra. Since water preferentially desorbs from the nitric acid solutions over the course of experimentation, HNO_3 liquid dosers

HNO$_3$ stock solution (mL)	H$_2$O used (mL)	HNO$_3$ (aq) Liquid Concentration (mol%)	HNO$_3$ Vapor Concentration (mol%)	HNO$_3$ Beam Concentration (mol%)
25.5	25.0	17.1 ± 0.7	1.1 ± 0.2	**0.6 ± 0.1**
32.5	25.0	19.5 ± 0.7	2.0 ± 0.4	**1.1 ± 0.2**
44.0	25.0	22.5 ± 0.9	4.1 ± 0.8	**2.2 ± 0.4**

Table 4.1.   HNO$_3$ Solution, Vapor, and Molecular Beam Concentrations. Displayed in Table 4.1 are HNO$_3$ liquid concentrations, HNO$_3$ vapor concentrations, and HNO$_3$ beam concentrations used for experiments in the present study, along with the amounts of HNO$_3$ stock solution [69 wt % HNO$_3$, Mallinckrodt] and distilled, deionized water used to create the HNO$_3$ solutions. All concentrations are reported in mol % [mol % HNO$_3$ = (mol HNO$_3$)/(mol HNO$_3$ + mol H$_2$O) x 100%)]. Vapor concentrations are estimated from liquid concentrations using the VLE data of Ghmeling et. al.[53] Beam concentrations are estimated assuming a purely effusive beam (though our beam is actually quasi-effusive in nature, Knudsen number; K$_n$~0.05). Thus, our concentration estimates do not take into account any mass focusing effects which are known to occur in mildly supersonic molecular beams. Liquid dosers employed for experimentation (~which held 25 mL of solution) were used until ~1.5 mL of solution was evaporated (~6% of the initial volume). Assuming this entire lost amount was H$_2$O (estimating conservatively), we calculated estimates of the error that would reflect such uncertainties in the solution concentrations.

111

(which hold approximately ~25 mL of liquid) were refilled once ~1.5 mL of solution (~6 % of the initial doser volume) had been evaporated from a liquid doser due to use. Shown in Table 4.1 are details regarding estimated liquid and vapor concentrations of our nitric acid solutions, with uncertainty bars corresponding to the solution loss over a standard two day use. Our reported film concentrations are estimated by assuming a *purely* effusive beam of nitric acid/water; i.e., no attempt was made to correct for mass focusing effects known to occur in mildly supersonic molecular beams. Film deposition rate was calibrated by the time needed to populate the bilayer H_2O TPD feature [1 BL_{H_2O} ~ $1x10^{15}$ molecules/cm^2][71] on Ir(111) via the technique of King and Wells.[72] Nitric acid species were characterized by mass fragments m/z~30 (NO^+) and m/z~46 (NO_2^+). Mass fragments characteristic of HNO_3^+ (m/z~63) and NO_3^+ (m/z~62) were not observed during TPD of the dilute films or by directing the dilute HNO_3 beams towards the QMS ionizing region. The absence of the NO_3^+ and HNO_3^+ mass signals is likely due to a combination of the dilute amounts of HNO_3 in the beams used in our study and the high ionization probability of this species in the QMS [consistent with older literature study of HNO_3 ionization[73]].

Results and Discussion

Temperature Programmed Desorption of Dilute (0 - 2.2 mol %) HNO_3 Films

Displayed in Figures 4.1(i)-(iv) are TPD spectra obtained by (1) first depositing 30 BL of pure water, 0.6 mol % HNO_3, 1.1 mol % HNO_3, and 2.2 mol % HNO_3, respectively, on the Ir(111) substrate at T ~ 77 K, then (2) heating the sample at a rate of 0.6 K/s to monitor the desorbing species via QMS. As Figure 4.1(i) illustrates, the desorption trace of the pure ASW film exhibits a distinctive 'bump' (near T~155 K), indicating the amorphous to crystalline phase transition which occurs in the film as the

Figure 4.1. Temperature Programmed Desorption of ASW and HNO$_3$ Films. Displayed in Figure 4.1 (i)-(iv) are temperature programmed desorption (TPD) spectra (offset for clarity) of pure ASW and dilute HNO$_3$ films of varying composition (0.6, 1.1, and 2.2 mol % HNO$_3$), respectively. All films were dosed at normal incidence at an Ir(111) sample temperature of T~77 K and were heated at a rate of 0.6 K/s.

Figure 4.1 Inset (a). Shown in Figure 4.1 Inset (a) are Arrhenius plots [ln (des. rate) vs. 1000/T] for each of the spectra (i)-(iv) shown in Figure 4.1.

Figure 4.1 Inset (b). Displayed in Figure 4.1 Inset (b) is a plot of the crystallization "temperature" (T$_c$) vs. HNO$_3$ concentration for the spectra of Figure 4.1. The crystallization "temperature" is defined as the point of inflection in the 'bump' of the TPD spectra of Figure 4.1(a) spectra. [This 'bump' is characteristic of the crystallization process (amorphous to crystalline transformation)[19,20] which occurs in ASW upon heating] Error bars for T$_c$ ($\pm 2\sigma$) are obtained from numerous TPD spectra measurements; error bars for the HNO$_3$ concentrations are those from Table 4.1. This plot illustrates that, despite uncertainties in HNO$_3$ film concentrations, the differences in TPD spectra due to presence of HNO$_3$ are statistically significant.

113

Crystallization Temperature (K)

(a)

HNO3 Concentration (mol %)

Crystalline Ice

(b)

Crystallization

Amorphous

LN(Desorption Rate BL/s)

Temperature (K)

'bump'

30 BL ASW/HNO₃

Ir(111)

(i) pure ASW

(ii) 0.6 mol% HNO₃

(iii) 1.1 mol% HNO₃

(x 5)

(iv) 2.2 mol% HNO₃

Desorption Rate (BL H₂O/s)

Temperature (K)
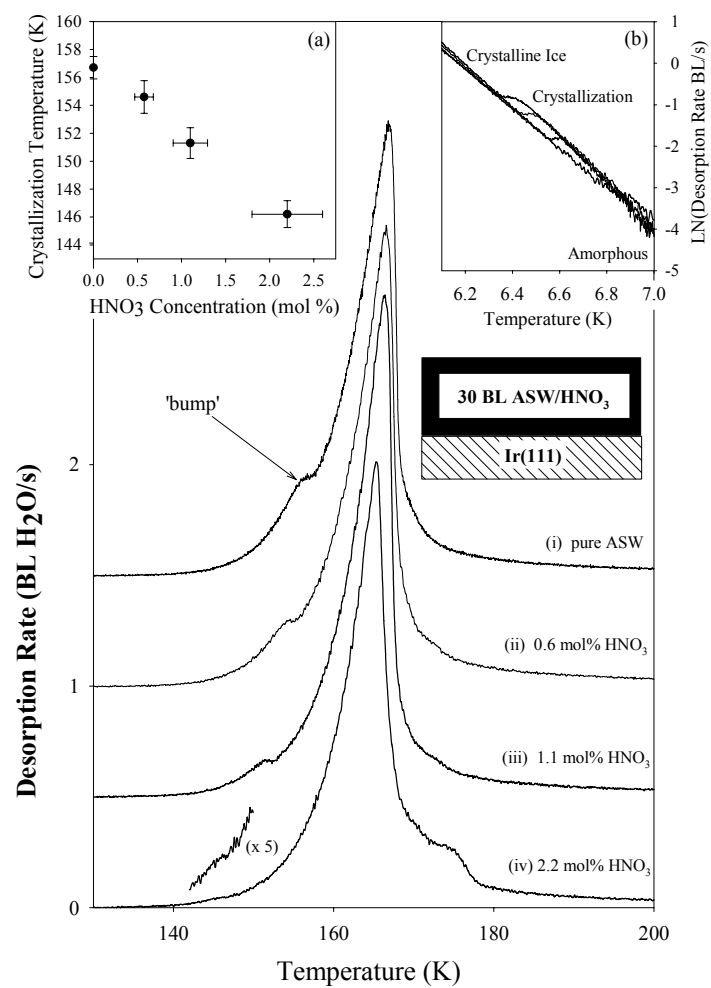
sample is heated. This 'bump' arises due to the difference in desorption rates of the ASW and crystalline ice (CI) phases[19]; CI has a lower desorption rate than ASW, and hence, a decrease in desorption occurs during the crystallization of the thin film. Figures 4.1(ii)-(iv) show desorption spectra of films created by deposition of H_2O/HNO_3 beams of varying composition (0.6, 1.1, 2.2 mol %) respectively. As these spectra demonstrate, the presence of HNO_3 decreases the temperatures during which the characteristic ASW crystallization TPD feature occurs, from T ~156.7 K for pure water, to T ~ 146.2 K for the 2.2 mol % HNO_3 film. Thus, it appears that the presence of HNO_3 may alter the crystallization kinetics of the ASW film, apparently speeding up the nucleation and/or growth of the crystalline ice phase. Experiments conducted by Hofer et. al.[49] on vitrified dilute solutions of hyperquenched glassy water (HGW) of a wide variety of binary aqueous systems (H_2O+salt, H_2O+alcohol) have shown that at *low* concentrations (~few percent) the initial effect of solutes is to *decrease* the glass transition temperature of water. It was reasoned this phenomena arises due to the increased mobility of H_2O molecules which occurs due to the weakening of the H-bonded network of glassy water by the solute. It may be possible that HNO_3 could have a similar effect on our ASW films, enhancing the mobility of the water molecules within the film and accelerating the nucleation and growth of the corresponding crystalline phase. What is also interesting to note is that the desorption rates for the amorphous and crystalline phases appear to be nearly identical for each case in Figures 4.1(i)-(iv); it is simply the crystallization 'bump' feature which appears to change. This is more easily seen in Figure 4.1 Inset (b), which shows an Arrhenius plot of the desorption spectra of Figures 4.1(i)-4.1(iv). As this figure demonstrates, it appears that (within our detection limits) the desorption rates of the amorphous and crystallized dilute HNO_3 films are nearly identical, with a shift in crystallization 'temperature' as a function of composition. Shown in the Figure 4.1 Inset

115

(a) is a plot of the 'crystallization temperature' of the H_2O spectra as a function of HNO_3 concentration. The term "crystallization temperature" refers to the inflection point of the crystallization 'bump' observed upon desorption of the amorphous films. Results of many experiments (0 - 2.2 mol % HNO_3 films) were averaged, and error bars ($\pm 2\sigma$ confidence intervals) applied to demonstrate that, even though uncertainties exist in the estimated film concentrations, TPD behavior of pure and HNO_3-doped films are statistically different. Thus, the apparent effect of HNO_3 is to accelerate the onset of crystallization (appearance of 'bump') within the ASW film, with ASW and CI desorption rates remaining essentially identical to the pure water spectra.

During desorption of dilute HNO_3 films as shown in Figures 4.1(ii)-4.1(iv), mass fragments of m/z~30 and m/z~46 (small features) are observed near the end of the desorption trace (T~170 K). We attribute these spectral features to the HNO_3 present in the ASW films. While the m/z~46 appears as a well-defined desorption peak, the m/z~30 exhibits a broad tail extending to higher temperatures (T > 200 K). These mass fragments, characteristic of nitric acid (m/z~30, 46) are much better visualized during desorption of thicker, more concentrated HNO_3 films. Desorption spectra from films (thicknesses of 30, 60 and 90 BL) grown with a ~2.2 mol % HNO_3/H_2O beam are shown in Figure 4.2. The inset to Figure 4.2 shows an enlarged view of the data, specifically the m/z~46 (NO_2^+) TPD feature. This data illustrates that an increase in HNO_3 film concentration results in the appearance of a 2nd water feature, associated with mass fragments m/z~30 and m/z~46. Increasing the thickness of the nitric acid film from 30-90 BL increases the intensity of this 2nd water desorption feature, along with the intensity of the nitric acid feature (m/z~46). An analogous effect is seen in desorption of films of a constant thickness with increasing HNO_3 concentrations; i.e. m/z~30 and

116
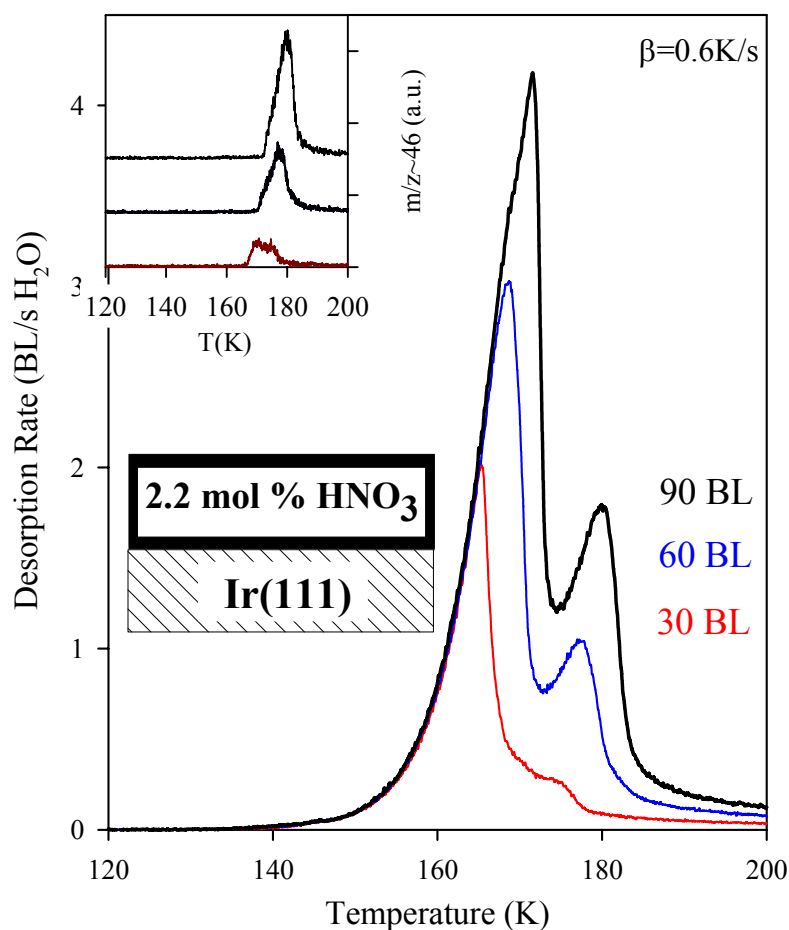
Figure 4.2. TPD Spectra of 2.2 mol % HNO₃ Films: Varying Film Thickness. Shown in Figure 4.2 are TPD Spectra obtained by dosing various thicknesses (30, 60, and 90 BL) of 2.2 mol % HNO₃ films at T~77 K and normal incidence, followed by heating to 200 K at a rate of 0.6 K/s. Displayed in the Figure 4.2 Inset are the m/z~46 fragment signal (NO_2^+) from the corresponding experiments.

m/z~46 features become more pronounced as the HNO_3 concentration of the film is increased. These data suggest that, for the large part of ASW desorption, nitric acid remains in the films with water preferentially desorbing from the film; only until a sufficient amount of H_2O has desorbed does the nitric acid and "associated" water feature appear to desorb from the sample. We speculate that this "associated" nitric acid-water species could be indicative of a nitric acid hydrate specie(s) (i.e., NAM or NAT) which are known to form in liquid and glassy phases at sufficiently high nitric acid to water ratios. This would be consistent with the observation that increasing amounts of total nitric acid in a film result in an increase in the intensity of the "associated" water desorption feature, which occurs at higher temperatures (T ~ 170 K).

A number of previous investigations[60-62,74,75] have suggested that desorption and/or evaporation rates of crystalline ice and amorphous water phases are reduced in magnitude (compared to pure ice) when HNO_3 is present in sufficient amounts to form hydrate species (typically more concentrated than the films employed in the present study). TPD and TPIR measurements of thin crystalline ice/nitric acid films have been conducted previously by Koehler et. al.[61,64] In these investigations, desorption spectra of stoichiometric (1:1 and 3:1) crystalline nitric acid films (corresponding to the NAM and NAT hydrate species) are generally observed to have higher desorption activation energies (desorption features at higher temperatures) than pure crystalline ice. These H_2O TPD features are observed to coincident with nitric acid desorption.[61,64] This finding would be qualitatively consistent with our observations, as our "associated" nitric acid-water species (Figure 4.2) desorbs at higher temperatures than the pure water phase. Livingston et. al.[60] conducted a desorption study of thin crystalline ice (D_2O) films in which pure layers (~1-3 ML) of HNO_3 had been dosed on the surface of the film. From

118

their study, they showed that the D_2O desorption rate was attenuated due to the presence of the HNO_3, possibly by the formation of an amorphous nitric acid hydrate layer. A similar effect of HNO_3 adsorbates on ice films has been observed in microbalance studies of thin ice films (~1-2 microns) with small amounts (0.5 - 7 ML) HNO_3.[62] In this study[62], H_2O evaporation was observed to decrease once a sufficiently large HNO_3 concentration had been developed (due to preferential H_2O desorption) in the film. Vapor pressure measurements by Hanson et. al.[76] demonstrate that H_2O vapor pressures above liquid and solid nitric acid/water solutions are reduced under sufficient HNO_3 concentrations. Conversely, other investigators[68] have observed *no* appreciable effect of the presence of HNO_3 on ice evaporation kinetics. As we will discuss shortly, we believe our films may be too dilute during the initial ASW desorption to see such effects. However, our results at *later* TPD times (where the effective HNO_3 concentration of the film has increased due to water desorption) would be consistent with the formation and desorption of a nitric acid hydrate.

Experiments were also conducted (not shown) in which nitric acid films were grown at T~77 K and heated to higher temperatures (T~1500 K). Besides the water and nitric acid desorption features occurring between T~140 -200 K, mass signals consistent with nitric acid fragments (m/z~30, 46), and recombinative O_2 desorption (m/z~32), were observed in desorption features at higher temperatures (T > 200 K). While the surface chemistry of HNO_3 on Ir(111) is not the focus of the present study, this does suggest that a small amount of the nitric acid within the film may remain/decompose on the Ir(111) after completion of multilayer H_2O desorption. This seems reasonable as several studies have shown Ir single crystal surfaces (Ir(111) and Ir(100)) to be active towards NO decomposition under UHV conditions.[77-80]

Crack and Fracture Formation in ASW/Dilute HNO₃ Films

As mentioned previously, ASW films are known to crack/fracture upon crystallization. This phenomenon can be observed by the CCl_4 "molecular volcano" experiment of Smith et. al.[20] Shown in Figures 4.3(a) and (b) is an example of this experiment conducted in our laboratory. In Figure 4.3(a), a structured film has been created by first dosing ~30 BL $H_2^{16}O$ ASW, followed by subsequent dosing of ~ 6 ML CCl_4 at T~77 K. This sample is then heated and, as illustrated by the spectra, desorption of the CCl_4 multilayers occurs between T~120-142 K, followed by desorption of the ASW layer. Again, the 'bump' observed in the H_2O spectra arises as a result of the ASW to CI phase transition.[19] Figure 4.3(b) shows a desorption spectra in which the 6 ML CCl_4 has been deposited first, followed by deposition of the 30 BL ASW overlayer. Upon heating, the CCl_4 multilayers remain trapped beneath the ASW until crystallization ['bump'], at which point an interconnected network of cracks/fractures are generated allowing the CCl_4 to rapidly escape ("molecular volcano[20]"), prior to desorption of the remaining ASW overlayer. Note that the $H_2^{16}O$ desorption traces shown in Figures 4.3(a) [CCl_4 on top] and 4.3(b) [CCl_4 on bottom] appear to be identical to the desorption spectra of the pure water films [with no CCl_4 layers] in Fig. 4.1(i). Figures 4.3(c)-(e) show TPD spectra from nanostructured films similar to that of Fig. 4.3(b), constructed by first depositing ~6 ML CCl_4, followed by deposition of 30 BL ASW containing dilute amounts of nitric acid (0.6, 1.1, and 2.2 mol % respectively). These structured films are then heated at a rate of 0.6 K/s to monitor the onset of film fracture [abrupt CCl_4 "molecular volcano" desorption]. As Figure 4.3(c) shows, the presence of ~0.6 mol % HNO_3 reduces the amount of abrupt CCl_4 desorption at crystallization of the overlying film ('bump'), shifting the CCl_4 desorption feature later in the TPD to a broad temperature range of T ~ 155-170 K, with a peak near T~163 K. As discussed previously

Figure 4.3. **TPD of ASW and HNO$_3$ Films: CCl$_4$ "Volcano" Desorption.**[20] Displayed in Figure 4.3(a)-(e) are desorption spectra from various structured films (see schematics) composed of CCl$_4$ (red), pure ASW, and dilute HNO$_3$ (black) of varying compositions (0.6, 1.1, and 2.2 mol %). Figure 4.3(a) shows TPD spectra of a film constructed by first depositing ~30 BL H$_2$^{16}O ASW, followed by deposition of ~6 ML CCl$_4$, and subsequent heating to T~200 K. Figures 4.3(b)-(e) show TPD spectra of structured films constructed by first depositing ~6 ML CCl$_4$, followed by deposition of ~30 BL H$_2$^{16}O ASW (b), 0.6 mol % HNO$_3$ (c), 1.1 mol % HNO$_3$ (d), and 2.2 mol % HNO$_3$ films (e), respectively. All films were dosed at normal incidence and at a sample temperature of T~77 K. TPD spectra were obtained at a heating rate of 0.6 K/s.
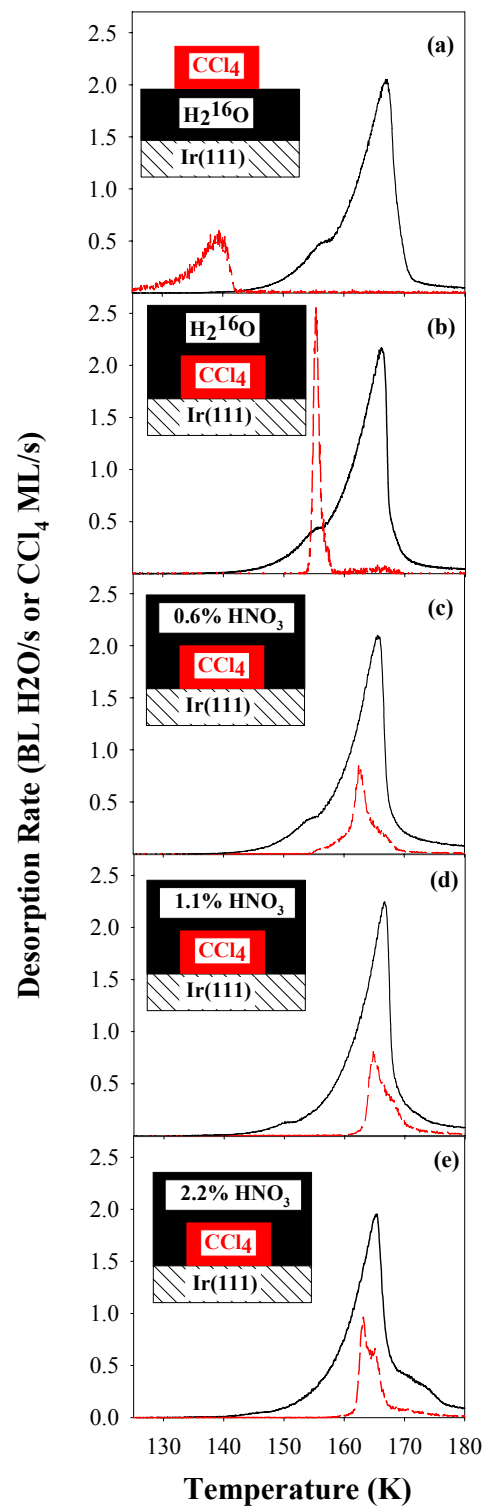
crystallization of the HNO_3-doped film occurs at an earlier temperature (T~154.6 K). Figure 4.3(d)-(e) shows experiments in which 1.1 mol % and 2.2 mol % nitric acid are present in the ASW films, respectively. These spectra also illustrate that the abrupt CCl_4 desorption coincident with crystallization has been eliminated, with all CCl_4 appearing to desorb between T~160-180 K in each case. Upon comparison with Figure 4.1 it is apparent that films with and without underlying CCl_4 layers exhibit identical H_2O desorption spectra. Altering the TPD ramp rate of an ASW desorption experiment alters the temperatures at which crystallization (and hence film fracture) occurs in pure ASW films.[20,28,33] As a further test of the ability of HNO_3 to reduce film fracture and cracking during crystallization, we have conducted the experiments (not shown) similar to those of Fig. 4.3(b)-(d) at additional ramp rates (0.05 K/s and 2 K/s); in these experiments, the presence HNO_3 was observed to eliminate CCl_4 desorption at crystallization and delay its' appearance closer to the end of the H_2O multilayers desorption

From the data it appears that the presence of nitric acid within ASW films significantly reduces the number of high conductance fracture pathways which occur within the film during the amorphous to crystalline phase transition. This prevents the abrupt desorption of CCl_4 during film crystallization (during the 'bump' in the H_2O desorption spectra), shifting CCl_4 desorption to later temperatures in the TPD spectra. It is interesting to note that CCl_4 peak desorption temperatures occur for HNO_3 films (Figs. 4.3(c)-(e)) when a substantial portion (~15-18 BL) of the water overlayer still remains on the substrate. One possible explanation for this behavior is that, while it appears negligible conductance pathways traverse the entire length of the dilute HNO_3 films during crystallization, some extent of void/fracture formation could occur locally within the film. In this picture, CCl_4 could be "sequestered" in voids within the overlying film, unable to exit the film until sufficient water overlayers have desorbed (to access these

void regions).   Another possibility is that crack/fracture formation has been completely eliminated in dilute HNO_3 films and that the dilute HNO_3 overlayer does not desorb in a layer-by-layer fashion.   Recent work by Kimmel et. al.[25] suggests that, despite exhibiting zero order desorption kinetics, *pure* ASW films dewet when annealed and crystallized at higher temperatures, presumably due to the hydrophobicity of the metal-bound, H_2O monolayer.   In this picture, underlying CCl_4 would be able to exit prior to complete desorption of the multilayer H_2O film since desorption would be accompanied by a dewetting process in the film.   If this same phenomena occurs in HNO_3-doped ASW films, CCl_4 would be able to escape prior to complete desorption of the water overlayer, even if film fracture had been completely eliminated.   Regardless, it appears from the data of Figures 4.3(a)-(c) that the presence of HNO_3 significantly reduces the amount of film fracture which occurs during crystallization ('bump').

Due to its' implications with regard to atmospheric chemistry, a number of HNO_3/H_2O uptake and desorption studies on thin films (thicknesses < 1-5 μm) have been conducted by several investigators.[58,60,63,74,75,81]   These previous studies and theories indicate that, under certain conditions, the desorption rate of HNO_3/H_2O films of sufficient HNO_3 concentration can inhibit ice evaporation rates, namely through a nitric acid hydrate capping layer on the ice surface.[75,81,82]   This layer can either be formed by uptake of HNO_3[67] or, more relevant to the present study, preferential evaporation of H_2O at the HNO_3/H_2O surface which would result in an increased HNO_3 surface concentration.   Studies of thin (~1-2 μm) HNO_3 films by Tolbert et. al. has suggested that HNO_3 hydrate (NAM, NAT) surface layers (formed by HNO_3 deposition on a thin ice film) can slow evaporation of underlying ice layers.[63]   Middlebrook et. al. has also shown that evaporation of crystalline HNO_3/H_2O thin (1μm) films, with dilute concentrations, can show modified evaporation kinetics dictated by surface concentrations of HNO_3

124

hydrates.[58]   Warshawsky et. al.[74] has demonstrated that crystalline ice evaporation rates from thin ($\sim$2-4 μm) films of ice can be lowered by the presence of a sufficient background pressure of HNO_3. However, for lower HNO_3 back pressures, no effect on ice evaporation was seen.   Additionally, studies of thin crystalline ice (D_2O) films, conducted by Livingston et. al.[60] suggest that thin layers (0.5-3.0 BL) of pure HNO_3 deposited on the surface of ASW D_2O films (thickness $\sim$ 25-200 BL) can noticeably reduce the desorption rate of CI (by a factor of $\sim$3-5). It is postulated that this occurs due to the formation of an amorphous nitric acid hydrate "cage" layer. This surface HNO_3 layer was also observed to lower water (HDO) diffusion rates in the crystalline ice D_2O film.[59]

We do not believe that an HNO_3 "capping" layer is behind the crack reduction phenomena shown in Figure 4.3 for several reasons. First, as shown in Figure 4.1, desorption rates of the amorphous and crystalline phases of the nitric acid doped films appear to be identical to the desorption rates expected for pure ASW/CI films; it is the temperature at which the amorphous to crystalline transformation occurs that is altered by addition of HNO_3. This observation argues against the presence of a surface hydrate layer in our dilute films, as the presence of this layer is often indicated by a reduction in the apparent H_2O desorption rate. Secondly, for concentrated HNO_3 films where the nitric acid features (m/z$\sim$30, 46) are clearly visible, the CCl_4 'pill' placed below the nitric acid films, begins to escape before desorption of the nitric acid features (m/z$\sim$30, 46) and "associated " water feature. If a nitric acid hydrate layer was "capping" the CCl_4 below the film, it seems that the CCl_4 would desorb after the desorption of the nitric acid features of the film. Finally, the estimated amounts of HNO_3 used in our films (0-2.2 mol %) are quite low compared to the stoichiometries believed necessary for formation of nitric acid hydrates (mono- or tri-hydrates). It does not seem likely that there would be

125

enough of these hydrates present in the film during crystallization to constitute an effective hydrate layer across the film surface.

While the mechanism by which crack/fracture reduction occurs is likely complicated, it does serve useful to speculate on possible reasons behind the observed behavior. As stated earlier, it has been hypothesized[15,20] that fracture formation within crystallizing pure ASW films is the result of stresses generated within the ASW film due to grain-grain impingement and/or density changes within the film. One might envision that as crystalline grains grow within the pure ASW film voids may develop near impingement points, locations where ASW is unable to flow sufficiently to relax stresses arising from the ASW/CI density differences. Once these internal stresses reach a critical point, cracking or fracture can occur within the crystallizing film. The presence of HNO_3 solutes within the film may affect this phenomenon, perhaps by increasing the mobility of H_2O molecules and enhancing their ability to relax and flow near grain impingement points. The hastening of ASW crystallization (suggested by Figure 4.1 spectra) in the presence of HNO_3 would be consistent with the idea of H_2O molecules having an increased mobility in HNO_3 doped ASW films. Studies by Barton et. al. of dilute H_2O/HNO_3 aerosol particles [(~1 % HNO_3)[83]] have suggested that, in dilute systems, crystalline ice nucleates first, followed by subsequent concentration and growth of the nitric acid hydrate phases from the surrounding parent phase. Additionally, studies of HNO_3 aerosols (0 - 50 mol % HNO_3) by Dickens et. al.[84] similarly suggest that, in dilute HNO_3 solutions (less than 15 mol % HNO_3), water ice nucleates and nitric acid hydrates (NAT) proceed to grow upon the pure ice nuclei. In a simplified view, HNO_3 solutes "pushed" into the surrounding amorphous regions during crystallization, and may exert an influence on water molecules near grain-grain impingement points characteristic of a more concentrated solution, as these regions will have a higher effective HNO_3

126

concentration than the initial as-deposited film. This may explain why only a small amount of HNO_3 solute (x_{HNO_3} ~0.6 mol %) is apparently required to reduce film fracture during crystallization. The presence of HNO_3 could also serve to provide preferential nucleation sites for crystalline ice. Factors such as numbers of CI grains and CI grain sizes may also effect crack/fracture propagation within the film, especially if fracture occurs near grain-grain impingement points.

Isotopic Mixing Experiments: Implications for Porous Transport within ASW Films

As discussed in the Introduction, recent studies[33] in our laboratory have suggested that the presence of crack/fracture pathways, generated in ASW thin films during the crystallization process, can be an important mode of *water* transport within ASW films during crystallization. When structured, layered films of isotopically labeled water are heated and analyzed via TDS,[17,18] intermixing is observed during crystallization (T~150-160 K), and hence during fracture formation. Like CCl_4 and other molecules[20,28,29], water molecules have an appreciable desorption rate during the ASW crystallization process, and thus would be available for vapor phase transport through these high-conductance pathways. Understanding the magnitude of the ASW bulk self-diffusivity[17,18] prior to crystallization (T~150-160 K) would be helpful in resolving some of the outstanding questions regarding the location of water's glass transition temperature and water's fragility at low temperatures.[12,85-87 *and references therein*] Dilute nitric acid films provide an opportunity to further probe these mechanisms (i.e., bulk diffusion-mediated transport vs. porosity-mediated transport). If the intermixing which occurs during crystallization is predominantly due to transport via cracks/fractures within the ASW film, it would seem reasonable to expect that this mixing should be significantly reduced during the

crystallization process when dilute nitric acid films are used, since film fracture will be reduced.

Shown in Figures 4.4(a)-(b) are TPD spectra of isotopically labeled, structured films of ASW ($H_2^{18}O$, $H_2^{16}O$, 0.6 mol % HNO_3/ $H_2^{16}O$) and CCl_4. In Figure 4(a), 30 BL of $H_2^{16}O$ ASW is deposited on the Ir(111) substrate, followed by deposition of ~6 ML CCl_4 (pill), and finally dosing of 30 BL $H_2^{18}O$ ASW. This structured film is then heated (at a rate of 0.6 K/s) and desorbing species are monitored via the QMS. As this spectra illustrates, interlayer mixing is observed (i.e. the onset of $H_2^{18}O$ desorption) during ASW crystallization and porosity formation (as signified by the abrupt desorption of CCl_4). As the spectra of Figure 4.4(a) illustrate, substantial intermixing occurs during crystallization (and coincident with film fracture) (T ~ 154-155 K) of the pure ASW films. These experimental results[33] are in good agreement with the measurements obtained previously by Smith and Kay.[17,18] Shown in Figure 4.4(b) is a desorption spectra from a structured film constructed by first dosing 30 BL $H_2^{16}O$ ASW, followed by deposition of a ~6 ML CCl_4 pill, and finally deposition of 30 BL 0.6 mol % HNO_3/ $H_2^{16}O$ film. In the case of this experiment, we would expect crack/fracture within the overlying HNO_3 layer to be reduced during film crystallization in comparison to the pure ASW film [as shown by Figure 4.1(c)]. Thus, if the observed intermixing which occurs near crystallization is indeed due to transport via crack/fracture formation, we would expect it to be reduced when compared to the pure water spectra in Figure 4.4(a). As the spectra of Figure 4.4 (b) illustrate, significantly less mixing is observed near crystallization (T ~ 154 - 155 K) than in Figure 4.4(a). The appearance of $H_2^{18}O$ does not begin to occur appreciably until T~155-156 K). We reason that this arises as a result of the reduction and/or elimination of film fracture due to the presence of HNO_3 in the $H_2^{16}O$ overlayer. As the CCl_4 desorption in Figure 4.4(b) confirms, film fracture does not occur during film

Figure 4.4. Pure and Dilute (0.6 mol %) HNO$_3$ ASW TPD Mixing Experiments. Displayed in Figure 4.4(a)-(b) are TPD mixing experiments of structured ASW and dilute HNO$_3$ ASW films. In Fig. 4.4(a), a structured film was created by first depositing 30 BL H$_2^{18}$O ASW, followed by deposition of a ~6 ML CCl$_4$ 'pill' (a marker for the onset of porosity formation), then deposition of 30 BL H$_2^{16}$O ASW, followed by desorption at a rate of 0.6 K/s. In Fig. 4.4(b), a structured film was created by deposition of 30 BL H$_2^{18}$O ASW, followed by deposition of ~ 6 ML CCl$_4$ 'pill', then deposition of 30 BL 0.6 mol % HNO$_3$ ASW film, followed by desorption at 0.6 K/s.

Figure 4.4(a) - 4.4(b) Insets. Desorption Ratio Plots. Shown in the Figures 4.4(a) and 4.4(b) insets are desorption ratio plots (r_{18}/r_{16}=[desorption rate of H$_2^{18}$O/desorption rate of H$_2^{16}$O]) during the TPD mixing experiments of Figures 4.4(a) and (b), respectively. This is displayed as open circles in both insets. The solid black lines shown in the Figure 4.4(a) inset are simulated desorption ratio traces calculated from simple TPD desorption/bulk diffusion model.[102] These simulated traces are shown to illustrate mixing behavior observed in a ***bulk*** diffusion mechanism (ignoring porosity-mediated transport), employing a range of ASW self-diffusion parameters of varying magnitudes ("high" diffusivity [E_a ~ 205 kJ/mol; D_o~3.2 x 10^{56} cm^2/s] to "low" diffusivity [E_a ~ 150 kJ/mol; D_o~1.0 x 10^{36} cm^2/s]). These plots demonstrate that, even if the magnitude of the bulk diffusivity is altered, the desorption ratio always increases monotonically if transport proceeds via a bulk diffusion mechanism.

129
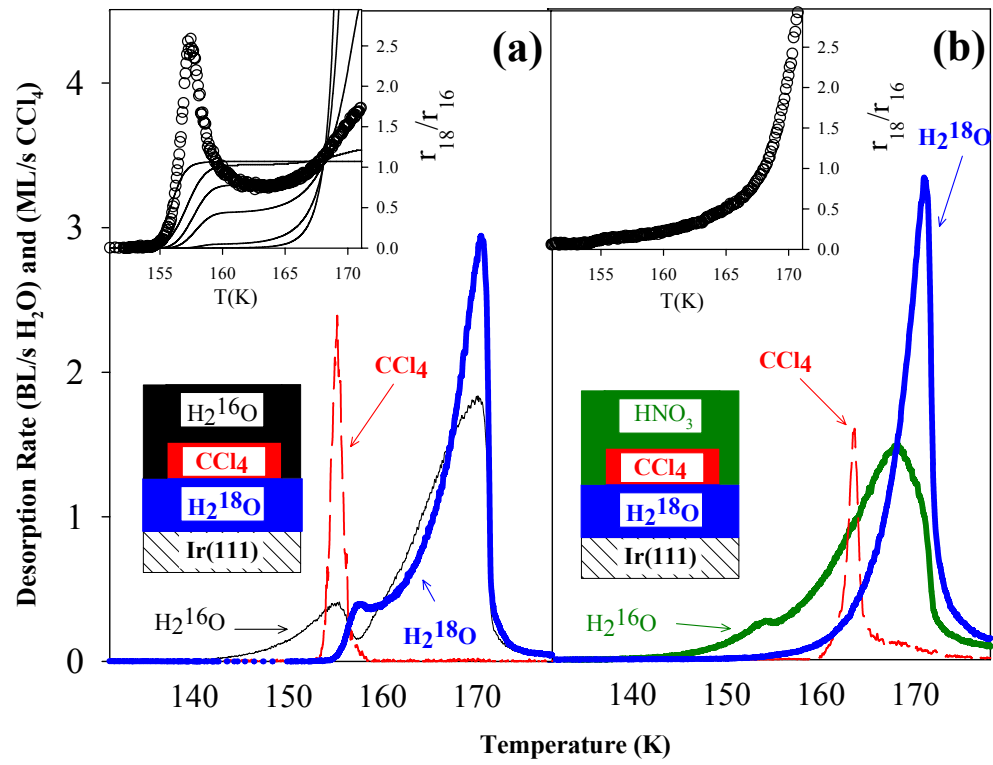
crystallization; rather, CCl_4 desorption begins at T ~ 160 K, with a peak temperature of T ~ 163 K. TPD mixing experiments conducted at different ramp rates (0.05 K/s and 2 K/s) (not shown) exhibit similar qualitative results. An alternative way of visualizing the TPD mixing spectra of Figs. 4.4(a) and 4.4(b) is to calculate the ratio of the $H_2^{18}O$ to $H_2^{16}O$ desorption rates during heating of the structured films. This ratio is shown in the insets of Figures 4.4(a) and (b). The quantity r_{18}/r_{16} [r_{18}/r_{16} = (desorption rate $H_2^{18}O$)/(desorption rate of $H_2^{16}O$)] of the Figure 4.4 Insets can be viewed as an instantaneous measure of the relative surface concentrations of the isotopically labeled water molecules during the TPD mixing experiment. If bulk diffusion is the primary mode of transport between these ASW layers, r_{18}/r_{16} would (by necessity) increase in a monotonic fashion upon heating, reflecting the increase in the $H_2^{18}O$ surface concentration as it diffuses toward the top of the film. Shown in Figure 4.4(a) inset is the experimentally determined desorption ratio r_{18}/r_{16}, (open circles) and that determined by a simple **bulk** diffusion model[88] (black solid lines). As the inset demonstrates, the experimental desorption ratio r_{18}/r_{16} (open circles) increases sharply at T ~ 155 K (during crystallization), peaks, decreases rapidly, and then increases again prior to complete desorption of the water film at T ~ 170 K. This behavior illustrates that intermixing observed between the two labeled ASW films is inconsistent with a simple bulk diffusion mechanism.

We have previously[33] interpreted the observed r_{18}/r_{16} behavior as evidence that transport via film fracture (which occurs during crystallization) is the predominant cause of intermixing between nanoscale ASW films during crystallization. As discussed earlier, porosity created within crystallizing ASW films are thought to collapse and densify upon further annealing as evidenced by numerous surface area measurements of conducted on ASW films.[13,14,88] We reason that the non-monotonic behavior of the

desorption ratio reflects this phenomenon; an increase in $H_2^{18}O$ transport during porosity formation, followed by a decrease in $H_2^{18}O$ as pores are sintered closed and made unavailable for vapor phase transport. We have recently[88] conducted isothermal TPD mixing experiments with corresponding surface area measurements (a measure of film porosity) to support this idea. Molecules of H_2O, unlike CCl_4, will have a substantial residence time within the fracture network owing to their lower desorption rate during crystallization. Thus, H_2O molecules could be "trapped" within the fracture network during film densification, contributing to the mixed appearance of the films at later TPD times (after pores have sintered closed). Calculating the desorption rate ratio during the nitric acid TPD mixing experiment of Fig. 4.4(b) should provide another important test for our porous transport hypothesis. If this non-monotonic behavior rises due to porous-mediated transport, it seems reasonable to expect this behavior to be "removed" with dilute HNO_3 films where crack/fracture formation has been reduced.

Upon examination of the mixing ratio (Figure 4.4(b) Inset) of the nitric acid structured film, it is observed that this non-monotonic behavior is in fact removed with reduction of the high conductance fracture pathways. Alteration of the magnitude of the diffusion coefficient cannot explain the removal of the non-monotonic desorption ratio behavior in the nitric acid structured film compared to the pure ASW film. The black solid lines shown in the Figure 4.4(a) inset are desorption ratios calculated from a simple bulk diffusion TPD model employing ASW diffusion parameters of varying magnitudes. As these traces illustrate, altering the magnitude of the diffusion coefficient does not affect the monotonic behavior of the desorption ratio, (r_{18}/r_{16}). This monotonic behavior is a fundamental characteristic of bulk diffusion mediated transport.

Also apparent from the TPD spectra is some overlap between the $H_2^{16}O$ and $H_2^{18}O$ desorption traces, indicative of some intermixing between the ASW layers. (Initial

appearance of $H_2^{18}O$ starts around T~155 K). While the exact mechanism behind this apparent mixing is unclear, there are several possibilities which could lead to such intermixing behavior. As mentioned during the discussion of Figure 4.3 (CCl_4 desorption from beneath pure and HNO_3-doped ASW films), CCl_4 desorption occurs while a substantial portion of the initial ASW overlayer (15-18 BL) remain on the sample. We hypothesized that this behavior could be due to either (i) small, localized regions of crack/void formation within the HNO_3-doped film, or (ii) non-uniform desorption of the crystallized ASW film (a phenomena thought to happen for *pure* ASW films[25]). Both of these scenarios could lead to the appearance of CCl_4 prior to complete desorption of the ASW overlayer, and thus could also lead to the appearance of $H_2^{18}O$ prior to desorption of the overlayer. If small, localized regions of fracture formation exist within the HNO_3 - doped film, this could result in a small amount of vapor phase transport between the labeled films, likely near the interface region. Likewise, if the HNO_3 -doped overlayer desorbs in a rough or non-uniform fashion, this could also lead to the appearance of the underlying $H_2^{18}O$ film, prior to complete desorption of the HNO_3 -doped ASW overlayer.

Roughness of the labeled water interface may also play a role in the observed spectral overlap. While *pure* ASW films prepared via molecular beam have been shown in several studies[23,30] to be relatively smooth, it is not fully known how the addition of the HNO_3 dopant may affect the morphology of the HNO_3 layer or the roughness of the pure water ($H_2^{18}O$)/HNO_3 doped ($H_2^{16}O$) interface.   It could also be possible that the observed mixing is due to bulk diffusion between the pure and HNO_3-doped layers. While we cannot discount this as a possible mechanism for the observed intermixing, it is important to note that most of the interlayer mixing appears *after* the desorption of the CCl_4 (CCl_4 desorption begins at T~160 K). Likewise, TPD spectra obtained with and without CCl_4 "pill" layers appear to be identical. This seems inconsistent with the idea of

133

substantial bulk diffusive mixing prior to crystallization, as one would expect the CCl_4 "pill" to hinder diffusive transport of H_2O. Future experiments are needed to clarify these issues. TPD experiments conducted with CCl_4 diffusion "barrier" layers across the *entire* sample (such as those employed in Chapters 2 and 3) may provide some additional insights into the mechanism behind this intermixing.

TPD mixing experiments similar to those displayed in Figures 4.4(a)-(b) were also conducted with layered, structured films of $H_2^{18}O$ and nitric acid layers containing 1.1 mol % and 2.2 mol % HNO_3. Experiments conducted with 1.1 mol % HNO_3 films exhibited qualitatively similar behavior to the experiments conducted with 0.6 mol % HNO_3 (Fig. 4.4(b)); a decrease in mixing near crystallization and removal of the non-monotonic desorption ratio behavior. Interestingly, the TPD mixing experiment conducted with 2.2 mol % HNO_3 film, while not demonstrating non-monotonic ratio behavior, did exhibit substantial interlayer mixing with the underlying $H_2^{18}O$ layer. It may be that at nitric acid concentrations higher than ~2.2 mol %, HNO_3 perturbs the ASW film enough to render comparison with pure ASW films less reliable. Figures 4.1 and 4.2 show that, at these higher HNO_3 concentrations (x_{HNO_3}~ 2.2 mol %), the "associated" H_2O-HNO_3 TPD features begin to become more apparent in the TPD spectra.

To summarize, we interpret the results of Figs 4.4(a)-(b) as additional evidence suggesting the presence of a porosity-mediated transport mechanism in ASW films during crystallization. This conclusion supports our previous findings which suggest that the observed mixing which occurs in pure ASW films near crystallization (Fig. 4.4(a)) is due to porous transport rather than bulk diffusion between dense ASW layers. We recognize that care should be taken when making comparisons between experiments conducted with pure ASW and those conducted with dilute HNO_3-doped films; our intent

is not to claim these films are identical.   Clearly, HNO_3 appears to alter the characteristics of the ASW film, reducing film fracture (Figure 4.3) and alters the timescales for film crystallization (Figure 4.1), making *quantitative* comparisons difficult. Despite these issues, we believe that TPD mixing experiments with HNO_3-doped ASW films can provide useful *qualitative* insights into the relevant transport mechanisms occurring in ASW films prior to crystallization.   Intermixing between the labeled layers of $H_2^{18}O$ and HNO_3 doped ($H_2^{16}O$) films is reduced during crystallization.   Additionally, the non-monotonic r_{18}/r_{16} behavior present in pure ASW structured films (Figure 4.4(a) Inset) is removed when dilute HNO_3 films are used (Figure 4.4(b) Inset).   As we recall from the plots in Figure 4.4(a) inset, in a bulk diffusion picture, this non-monotonic r_{18}/r_{16} behavior cannot be removed simply by altering the magnitude of the H_2O self diffusivity. As we have discussed, these experiments have provided important tests for our porous transport hypothesis; the observed results are consistent with the presence of a porous transport mechanism. The apparent mixing which occurs at later times in the TPD mixing experiments remains an open question.   Future experiments are needed to shed light on the mechanism behind this observed interlayer mixing.

Conclusions

We have conducted thermal desorption experiments of dilute nitric acid films ($x_{HNO3} < 2.2$ mol %), with particular interest in examining the effects of this species on crystallization induced film fracture known to occur in ASW films upon annealing. Transport between dilute HNO_3 films and $H_2^{18}O$ ASW films have also been examined. Our main conclusions can be summarized as follows:

(1)   The presence of dilute amounts of nitric acid (~0.6 mol % and higher) appears to significantly reduce the amount of film fracture which occurs during the amorphous solid

water to crystalline ice transition. This is evidenced by elimination of the CCl$_4$ "molecular volcano[20]" feature and surface area measurements.

(2) The desorption rates of the amorphous and crystalline phases of dilute HNO$_3$ films remain largely unchanged from the pure ASW desorption spectra; it is merely the phase transition temperature that has changed. The presence of nitric acid in the ASW film results in a 2nd H$_2$O TPD feature coincident with characteristic desorption features (m/z~30, 46) of HNO$_3$. Increasing the total amount of HNO$_3$ within the ASW film (either by dosing with a more concentrated beam or dosing thicker ASW films with the same HNO$_3$ concentration) results in a corresponding increase in these features. This "associated" nitric acid-water feature may indicate the presence of a nitric acid hydrate (NAM or NAT) as the ASW film becomes more concentrated in HNO$_3$ during desorption.

(3) Intermixing experiments between dilute HNO$_3$ films (~0.6, 1.1 mol %) and pure H$_2$^{18}O ASW exhibit less mixing than is seen in pure H$_2$^{16}O/H$_2$^{18}O mixing experiments, especially during crystallization ('bump'). Additionally, the non-monotonic behavior observed in the desorption ratio (r_{18}/r_{16}) of the pure ASW structured films is removed in corresponding film constructed with nitric acid. This is interpreted as further evidence of the importance of porosity mediated transport in pure nanoscale ASW films.

References

1.   P. Jenniskens, D. F. Blake, Planet. Space Sci. **44**, 711 (1996)

2.   P. Jenniskens, D. F. Blake, Science **265**, 5173 (1994)

3.   D. Prialnik, U. Egozi, A. Bar-nun, M. Podolak, Y. Greenzweig, Icarus **106**, 499 (1993)

4.   D. Laufer, E. Kochavi, A. Bar-Nun, Phys. Rev. B. **36**, 9219 (1987)

5.   D. Prialnik, A. Bar-nun, Astron. Astrophys. **258**, L9 (1992)

6.   J. Klinger, J. Phys. Chem. **87**, 4209 (1983)

7.   A. H. Delsemme, J. Phys. Chem. **87**, 4214, (1983)

8.   R. Smoluchowski, Astrophysical J. **244**, L31 (1981)

9.   D. Blake, L. Allamandola, S. Sandford, D. Hudgins, F. Freund, Science **254**, 548 (1991)

10.   P. Jenniskens, D. F. Blake, Astrophys. J. **473**, 1104 (1996)

11.   H. G. Heide, Ultramicroscopy **14**, 271 (1984)

12.   P. G. Debenedetti, *Metastable Liquids: Concepts and Principles* (Princeton University Press, Princeton, NJ, 1996).

13.   D. J. Safarik, R. J. Meyer, C. B. Mullins, J. Chem. Phys. **118**, 4660 (2003)

14.   Z. Dohnálek, G. A. Kimmel, R. L. Ciolli, K. P. Stevenson, R. S. Smith, B. D. Kay, J. Chem. Phys. **112**, 5932 (2000)

15.   Z. Dohnálek, R. L. Ciolli, G. A. Kimmel, K.P. Stevenson, R. S. Smith, B. D. Kay, J. Chem. Phys. **110**, 5489 (1999)

16.   R. S. Smith, C. Huang, E. K. L. Wong, B. D. Kay, Surf. Sci. **367**, L13 (1996)

17.   R. S. Smith, B. D. Kay, Nature **398**, 788, (1999)

18.   R. S. Smith, Z. Dohnálek, G. A. Kimmel, K. P. Stevenson, B. D. Kay, Chem. Phys. **258**, 291 (2000)

19.   R. J. Speedy, P. G. Debenedetti, R. S. Smith, C. Huang, B. D. Kay, J. Chem. Phys. **105**, 240 (1996)

20.   R. S. Smith, C. Huang, E. K. L. Wong, B. D. Kay, Phys. Rev. Lett. **79**, 909 (1997)

21.   G. A. Kimmel, Z. Dohnálek, K. P. Stevenson, R. S. Smith, B. D. Kay, J. Chem. Phys. **114**, 5295 (2001)

22.   G. A. Kimmel, K. P. Stevenson, Z. Dohnálek, R. S. Smith, B. D. Kay, J. Chem. Phys. **114**, 5284 (2001)

23.   K. P. Stevenson, G. A. Kimmel, Z. Dohnálek, R. S. Smith, B. D. Kay, Science **283**, 1505 (1999)

24.   J. M. K. Donev, Q. Yu, B. R. Long, R. K. Bollinger, S. C. Fain Jr., J. Chem. Phys. **123**, 044706/1 (2005)

25.	G. A. Kimmel, N. G. Petrik, Z. Dohnalek, B. D. Kay, Phys. Rev. Lett. **95**, 166102/1 (2005)

26.	H. Miura, H. Ohta, N. Okamoto, T. Kaga, Appl. Phys. Lett. **60**, 2746 (1992)

27.	H. Miura, N. Okamoto, J. Appl. Phys. **75**, 4747 (1994)

28.	P. Ayotte, R. S. Smith, K. P. Stevenson, G. A. Kimmel, B. D. Kay, J. Geo. Research [Planets], **106**, E12 33387 (2001)

29.	J. L. Blanchard, J. T. Roberts, Langmuir **10**, 3303 (1994)

30.	M. S. Westley, G. A. Baratta, R. A. Baragiola, J. Chem. Phys. **108**, 3321 (1998)

31.	R. Souda, Chem. Phys. Lett. **415**, 146 (2005)

32.	R. Souda, Phys. Rev. Lett. **93**, 235502/1, (2004)

33.	S. M. McClure, D. J. Safarik, T. M. Truskett, C. B. Mullins, submitted March 2006

34.	A. Omta, M. F. Kropman, S. Wouterson, H. J. Bakker, Science **301**, 347 (2003)

35.	A. W. Omta, M. F. Kropman, S. Woutersen, H. J. Bakker, J. Chem. Phys. **119**, 12457 (2003)

36.	L.-A. Näslund, D. C. Edwards, P. Wernet, U. Bergmann, H. Ogasawara, L.G. M. Pettersson, S. Myeni, A. Nilsson, J. Phys. Chem. A. **109**, 5995 (2005)

37.	R. W. Gurney, *Ionic Processes in Solution* (McGraw-Hill Book Company, Inc., New York, NY, 1953)

38.	Y. Marcus, *Ion Solvation* (John Wiley and Sons Ltd., Chichester, UK/Great Britain, 1985)

39.	F. X. Prielmeier, E. W. Lang, R. J. Speedy, H.-D. Lüdemann, Phys. Rev. Lett. **59**, 1128 (1987)

40.	C. A. Angell, E. D. Finch, L. A. Woolf, P. Bach, J. Chem. Phys. **65**, 3063 (1976)

41.	F. Sciortino, A. Geiger, H. E. Stanley, J. Chem. Phys. **96**, 3857 (1992)

42.	F. Sciortino, A. Geiger, H. E. Stanley Nature **354**, 218 (1991)

43.	R. Leberman, A. K. Soper, Nature **378**, 364 (1995)

44. A. Botti, F. Bruni, M. A. Ricci, A. K. Soper, J. Chem. Phys. **121**, 7840 (2004)

45. F. Bruni, M. A. Ricci, A. K. Soper, J. Chem. Phys. **114**, 8056 (2001)

46. E. W. Lang, S. Bradl, W. Fink, H. Radkowitsch, D. Girlich, J. Phys. Cond. Matt. **2**, SA195 (1990)

47. W. Fink, E. W. Lang, J. Phys. Chem. **92**, 6440 (1988)

48. T. Koop, B. Luo, A. Tsias, T. Peter, Nature **406**, 611 (2000)

49. K. Hofer, G. Astl, E. Mayer, G. P. Johari, J. Phys. Chem. **95**, 10777 (1991)

50. C. A. Angell, E. J. Sare, J. Chem. Phys. **52**, 1058 (1970)

51. H. Kanno, C. A. Angell, J. Phys. Chem. **81**, 2639 (1977)

52. K. Satoh, H. Kanno, Bull. Chem. Soc. Jpn. **55**, 1645 (1982)

53. J. Gmehling, U. Oken, *VLE Data Collection Supp. 2: Aqueous Systems*, (Scholium Intl. 1977)

54. G. Ritzhaupt, J. P. Devlin, J. Phys. Chem. **95**, 90 (1991)

55. G. Ritzhaupt, J. P. Devlin, J. Phys. Chem. **81**, 521 (1977)

56. M. Leuchs, G. Zundel, J. Phys. Chem. **82**, 1632 (1978)

57. P. R. McCurdy, W. P. Hess, S. S. Xantheas, J. Phys. Chem. A. **106**, 7628 (2002)

58. A. M. Middlebrook, M. A. Tolbert, K. Drdla, Geophys. Res. Lett. **23**, 2145 (1996)

59. F. E. Livingston, S. M. George, J. Phys. Chem. B **103**, 4366 (1999)

60. F. E. Livingston, S. M. George, J. Phys. Chem. A **102**, 10280 (1998)

61. B. G. Koehler, Int. J. Chem. Kinetics. **33**, 295 (2001)

62. C. Delval, M. J. Rossi, J. Phys. Chem. A. **109**, 7151 (2005)

63. M. A. Tolbert, A. M. Middlebrook, J. Geophys. Res, **95** 22423 (1990)

64. B. G. Koehler, A. M. Middlebrook, M. A. Tolbert, J. Geophys. Res. **97**, 8065 (1992)

65. R. Tisdale, A. M. Middlebrook, A. J. Prenni, M. A. Tolbert, J. Phys. Chem. A, **101**, 2112 (1997)

66. R. H. Smith, M.-T. Leu, L. F. Keyser, J. Phys. Chem. **95**, 5924 (1991)

67. H. Reinhardt, M. Fida, R. Zellner, J. Mol. Structure **661**, 567 (2003)

68. U. M. Biermann, J. N. Crowley, T. Huthwelker, G. K. Moortgat, P. J. Crutzen, Th. Peter, Geo. Res. Lett. **25**, 3939 (1998)

69. J.E. Davis, S.G. Karseboom, P.D. Nolan, C.B. Mullins, J. Chem Phys., **105**, 8362 (1996)

70. N. F. Ramsey, *Molecular Beams*, Cambridge Univ. Press, (1960)

71. P. A. Thiel, T. F. Madey, Surf. Sci. Rep. **7**, 211, (1987)

72. D. A. King, M. G. Wells, Proc. R. Soc. London Ser. A **339**, 245 (1974)

73. R. A. Friedel, J. L. Schultz, A. G. Sharkey Jr., Anal. Chem. **31**, 1128 (1959)

74. M. S. Warshawsky, M. A. Zondlo, M. A. Tolbert, Geophys. Res. Lett. **26**, 823 (1999)

75. T. Peter, R. Müller, P. J. Crutzen, T. Deshler, Geophys. Res. Lett. **21**, 1331 (1994)

76. D. Hanson, K. Mauersberger, J. Phys. Chem. **92**, 6167 (1988)

77. T. Fujitani, I. Nakamura, Y. Kobayashi, A. Takahashi, M. Haneda, H. Hamada, J. Phys. Chem. B. **109**, 17603 (2005)

78. S. Khatua, G. Held, D.A. King, Surf. Sci. **586**, 1 (2005)

79. J. E. Davis, S. G. Karseboom, P. D. Nolan, C. B. Mullins, J. Chem. Phys. **105**, 8362 (1996)

80. J. C. L. Cornish, N. R Avery, Surf. Sci. **235**, 209 (1990)

81. T. Deshler, Th. Peter, R. Müller, P. Crutzen, Geophys. Res. Lett., **21**, 1327 (1994)

82. S. C. Wofsy, R. J. Salawitch, J. H. Yatteau, M. B. McElroy, B. W. Gandrud, J. E. Dye, D. Baumgardner, Geo. Res. Lett., **17**, 449 (1990)

83. N. Barton, B. Rowland, J. P. Devlin, J. Phys. Chem. **97**, 5848 (1993)

84. D. B. Dickens, J. J. Sloan, J. Phys. Chem. A. **106**, 10543 (2002)

85. P. G. Debenedetti, J. Phys. Cond. Matt. **15**, R1669 (2003)

86.   C. A. Angell, Chem. Rev. **102**, 2627 (2002)

87.   C. A. Angell, Annu. Rev. Phys. Chem. **55**, 559 (2004)

88.   S. M. McClure, E. Barlow, M. Akin, D. J. Safarik, T. M. Truskett, C. B. Mullins, *in preparation*

Chapter 5: Concluding Remarks

The quest to develop a comprehensive description of the chemistry and physics of liquid water has proven to be a complex and challenging problem. Glassy water phases, such as amorphous solid water (ASW)[1], have recently been the subject of intense interest and research, in large part due to their importance in understanding the behavior of supercooled liquid water.[2] Despite the wealth of experimental and theoretical work[2-7] (*and references therein*), researchers have yet to conclusively resolve controversies surrounding very fundamental properties of glassy water, such as its glass transition temperature (T_g) and low temperature relaxation behavior. A complicating factor in resolution of these problems is the inherent difficulty of experimental study of supercooled liquid and glassy water phases. Bulk water crystallizes much too rapidly over a wide range of temperatures (T~160-231 K)[2-5,8] for conduction of reliable measurements, and transport processes (such as diffusivity (D) and viscosity (μ)) characteristic of the glass transition (μ~10^{13} Poise, D~10^{-18} cm^2/s) occur too slowly for direct measurement with bulk water samples. As a consequence of these experimental limitations, many of the hypotheses proposed by the theoretical community to describe the behavior of bulk supercooled liquid and glassy water phases (liquid-liquid critical point[9-10], fragile-to-strong transition[11-12]) are unable to be experimentally verified at this time.

The challenging experimental constraints of studying metastable water phases have provided the impetus for researchers to create innovative techniques to investigate the behavior of low temperature, amorphous water phases. Pioneering work by the Kay group[13-24] and others[25-31] have shown the utility of studying nanoscale films (thicknesses of 10-100 nm) of glassy water to gain insights into the glass transition of water and its

relaxation dynamics at low temperatures. Samples of such dimensions enable investigation of diffusion processes near T_g on a reasonable timescale. These techniques have provided valuable insights into the thermodynamics[13], crystallization kinetics[14-16,30], structural properties[19-26] and transport[17-18,31] properties of ASW. However, despite these recent innovations and focused research, new questions have arisen; in particular, how structural changes in nanoscale ASW films (e.g.; crystallization induced film fracture[19,24,26,32], morphology changes[14,23,25,27-28,30]) can affect transport phenomena and transport mechanisms in thin films. Developing a complete understanding of these important variables will allow researchers to fully utilize this novel thin film approach to probe and investigate the properties of ASW.

In this dissertation, transport phenomena in ASW films were investigated, with particular attention to the role of vapor-phase transport via cracks and fractures created within the ASW film during crystallization (T~150-160 K). Experiments were conducted under ultrahigh vacuum (UHV) conditions using molecular beams of water to grow dense, non-porous nanoscale films of ASW. As discussed in the Introduction, the study of *nanoscale* ASW films via thermal desorption spectroscopy (TDS) allows for study of transport processes on length scales relevant to diffusion near the glass transition (D~10^{-18}-10^{-20} cm^2/s). By studying the desorption of structured films of labeled $H_2^{18}O$ and $H_2^{16}O$ ASW, transport processes during crystallization (T~150-160 K) can be probed. Desorption studies of structured films with and without diffusion "barrier" layers, surface area measurements, isothermal/variable ramp rate desorption experiments, and experiments with dilute HNO_3 films were employed to determine the relative roles of bulk diffusive transport and porous transport in ASW films near crystallization. As discussed previously, the magnitude of the ASW diffusivity prior to crystallization has

important implications with regards to water's glass transition and low temperature fragility.

In Chapter 2, transport in nanoscale (10-100 nm) structured films of ASW ($H_2^{16}O$, $H_2^{18}O$) and CCl_4 was investigated via thermal desorption techniques. Desorption of structured films with varying amounts (0-30 ML CCl_4) of diffusion "barrier" layers between labeled ASW layers were shown to exhibit similar mixing behavior, indicating that bulk diffusion prior to porosity formation (T~155 K) is negligible. The observed transport behavior was also found to be fundamentally inconsistent with a classical bulk diffusion mechanism, as determined by comparison of the experimental desorption ratio (r_{18}/r_{16}) with that predicted by model *bulk* diffusion calculations. Desorption experiments were also conducted with varying heating rates, illustrating that the observed translational motion within the ASW film is always concurrent with film fracture and the amorphous to crystalline phase transition. These results suggested that transport via cracks and fissures formed within the films during crystallization is the predominate mode of intermixing within ASW during crystallization (T~150-160 K). Hence our results suggested that the diffusivity of ASW prior to crystallization is more consistent with ASW being either (i) a strong liquid or (ii) a rigid glass prior to 160 K. In the case of (i), this would require a fragile-to-strong transition in water diffusivity between T~160 K and 230 K. This finding is in contrast with conclusions drawn by previous investigators.[17-18]

In Chapter 3, a systematic study of intermixing experiments were conducted with structured ASW films of various thicknesses, diffusion barrier layers of varying thickness, and varying TPD heating rates. Isothermal desorption measurements and surface area measurements (using $CClF_2H$ probe molecule[33]) revealed that the translational motion of labeled water molecules observed during crystallization is coincident with an increase in film porosity. MeOH was used as a "probe" molecule to

illustrate the ability of CCl_4 barrier layers to hinder bulk diffusion within structured ASW films. Investigations of abrupt CCl_4 desorption were also conducted to determine its' dependence on film thickness, film crystallization and anneal temperatures. The CCl_4 results demonstrated parallels between observed water mixing and the onset of porosity formation within the ASW films, providing further support for the predominate role of porous transport within ASW films.

In Chapter 4, I investigated the effect of dilute amounts (0 - 2.2 mol %) of HNO_3 on the porosity formation in crystallizing ASW films. It was found that small amounts of HNO_3 (~0.6 mol %) were effective in reducing crack/fracture formation during crystallization as evidenced by elimination of CCl_4 "molecular" volcano desorption and film surface area measurements. The presence of HNO_3 was also found to hasten the onset of ASW crystallization (appearance of 'bump') during TPD experiments. Transport within nanoscale structured films of HNO_3 (0.6 mol %) and $H_2^{18}O$ ASW was investigated, in an effort to study intermixing in ASW films in which crystallization induced porosity was expected to be significantly reduced. In contrast to the pure water mixing experiments of Chapters 2 and 3, mixing experiments with the HNO_3 films exhibited substantially less mixing during crystallization. Furthermore, the desorption ratio (r_{18}/r_{16}) of the HNO_3 mixing experiments did not exhibit the non-monotonic behavior characteristic of the pure ASW films. Though the dilute $HNO_3/H_2^{18}O$ mixing experiments introduce new complexities into the data (i.e. altered timescales for ASW crystallization, possible ion-water interactions), the qualitative results of these experiments are interpreted as further evidence for the importance of a porous transport mechanism in ASW films.

The primary conclusion of this work is that the transport observed between 150-160 K in ASW thin films (10-100 nm) is predominantly due to transport via

145

crack/fracture pathways created within the film during crystallization. Previous investigators[17-18] have interpreted this mixing (in similar constructed films) as due to bulk diffusion. The self-diffusivity values obtained from this interpretation have provided some of the strongest support for the view that ASW melts into a 'fragile' liquid at low temperatures. In contrast, our findings demonstrate that water does not exhibit substantial mixing prior to crystallization at T~160 K. This implies that ASW is either (i) a rigid glass below 160 K (T_g > 160 K) or (ii) a 'strong' liquid below 160 K (T_g ~ 136 K). In the case of the latter (ii), this would require a change from fragile-to-strong dynamics between T~160 K and 230 K.

Recommendations for Future Work

The utilization of surface science techniques, in particular molecular beam grown ASW films, has certainly furthered our understanding of transport properties of ASW near crystallization. However, many questions remain to be answered with regard to the physical behavior and nature of nanoscale ASW films, and how these behaviors should shape our comparison of thin film data with studies performed on bulk samples. One challenging task in particular, would be the development of a thorough, *quantitative* model (incl. pore/fracture sizes, structures, formation and sintering kinetics) of porous transport in crystallizing ASW films. A descriptive, quantitative model, along with experimental results, would provide further support for the porous transport viewpoint. Discussed in this concluding section are several avenues of research, related to the present work, which could provide further insights into such outstanding issues.

Much of the existing evidence[14,19,23-24,26-28,30] supporting crack/fracture in ASW thin films has been obtained by employing thermal desorption techniques. While these studies have contributed much to our current understanding of ASW, more direct means of probing the morphology changes in ASW films are certainly desirable. Recent work by

146

Donev et. al.[25] utilized atomic force microscopy (AFM) to study morphology changes in ultrathin (~5 BL) ASW layers on an Au(111) substrate. While these clever studies have provided a more direct verification of changes in ASW film morphology upon crystallization, AFM studies on samples of similar character to the present study (30 -200 bilayers) under similar temperature control ($\Delta T \pm 0.1K$) would certainly be desirable. Information gleaned from these studies could be used to estimate pore dimensions, number density of pores, and provide insights into the kinetics of film fracture development. Such parameters[34-35] are likely to be necessary in the construction of a *quantitative* model of porous transport in these thin films.

Additionally, it may be possible to obtain pore size estimates by conducting "molecular volcano[19]" experiments with underlying molecules of varying sizes and shapes. It has been shown that many "smaller" molecules (such as N_2, O_2, CH_4, Ar, CCl_4)[19,24,26] can easily escape through the high conductance pathways generated during ASW crystallization. If a series of sufficiently volatile "larger" molecules could be discovered (some of which are too large to travel through the porous network), these could be used to gain estimates of the size and relative distribution of fracture pathways generated within crystallizing ASW films via the CCl_4 "molecular volcano[19]" measurement. Measurements such as these may provide more detailed information regarding the structural characteristics of the fracture network generated within the ASW film.

Preliminary efforts in our laboratory to use n-pentane (C_5H_{12}) as a diffusion "barrier" (similar to CCl_4 used in Chapters 2 and 3) yielded some very interesting results. While CCl_4 (and other immiscible, hydrophobic chlorinated halocarbons) behaved as excellent diffusion barriers, n-pentane molecules (also expected to be hydrophobic and immiscible with H_2O) were able to diffuse through ASW and desorb at $T \sim 110\text{-}120$ K.

The mechanism by which these long-chain hydrocarbons diffuse through a presumably dense, non-porous ASW overlayer is unclear, as (a) translational and rotational motion of water molecules is expected to be negligible at these temperatures, and (b) our beam-deposited films are likely to be dense and nonporous. Very recent experiments by Souda et. al.[36-37] have demonstrated that hydrocarbons such as butane and hexane, dosed onto thin (~50 BL) D_2O films (background dosed), are able to incorporate into water films at temperatures as low as T ~ 50-100 K. It was argued[36-37] from these results that this is indicative of the propensity of the open structure of ASW to hydrate molecules. However, it is still not understood how the ASW structure, at such low temperatures, can reorient to accommodate these large, hydrophobic molecules in the bulk structure of the film, as translational and rotational motion of H_2O would be expected to be insignificant at such low temperatures. Experiments with straight chained- and branched- alkanes on dense, non-porous beam grown ASW films are warranted and may yield further insights on this very interesting behavior.

Results shown in Chapter 4 illustrated that the presence of HNO_3 can reduce the crystallization temperature and reduce fracture formation in amorphous solid water films. While it was postulated that this behavior could arise due the effects of ions on the mobility of water molecules, further investigation of this mechanism is certainly desired. Experiments performed using ASW films doped with dilute amounts of other volatile acids (such as HCl, acetic acid, H_2SO_4) could prove useful in shedding light on the mechanism by which HNO_3 can reduce and prevent crack/fracture propagation across thin ASW films. By systematically varying the cation and anion character, possible trends and relationships could be drawn between cation/anion effects on crystallization and porosity formation and their H-bonding "structure-making" and "structure breaking" [38-39] properties. These could prove useful in developing a firmer qualitative description

of the mechanism(s) at work. Additionally, if a surface sensitive "probe" molecule (such as $CClF_2H$) could be found and used to characterize hydrogen bonding (i.e.; quantifying "non-acid bound" vs. "acid-bound" surface H_2O molecules) at the surface of dilute acid ASW films, this could also yield further insights into the possible effect of ions on H-bonding network of ASW. Work by Holmes et. al.[40] has suggested that adsorption of halocarbons (such as $CClF_2H$) on ice surface occur by bonding of the halogen lone pair to the H atom of dangling O-H surface bonds. Thus, adsorption/desorption characteristics of species from the acid-doped ASW surface could depend upon the nature of hydrogen bonding (strength of O-H bond) within the film (similar to the ASW/CI sensitivity of $CClF_2H$[33]), allowing for differentiation between pure and acid doped ASW surfaces.

References

1.   E. F. Burton, W. F. Oliver, Proc. Roy. Soc. A. **153**, 166 (1935)

2.   P. G. Debenedetti, *Metastable Liquids: Concepts and Principles* (Princeton University Press, Princeton, NJ, 1996).

3.   P. G. Debenedetti, J. Phys. Cond. Matt. **15**, R1669 (2003)

4.   C. A. Angell, Chem. Rev. **102**, 2627 (2002)

5.   C. A. Angell, Annu. Rev. Phys. Chem. **55**, 559 (2004)

6.   P. G. Debenedetti, H. E. Stanley, *Physics Today*, June 2003, p. 40

7.   H. E. Stanley, S. V. Buldyrev, M. Canpolat, O. Mishima, M. R. Sadr-Lahijany, A. Scala, F. W. Starr, Phys. Chem. Chem. Phys. **2**, 1551 (2000)

8.   O. Mishima, H. E. Stanley, Nature **396**, 329 (1998)

9.   P. H. Poole, F. Sciortino, U. Essmann, H. E. Stanley, Nature **360**, 324 (1992)

10.   P. H. Poole, F. Sciortino, T. Grande, H. E. Stanley, C. A. Angell, Phys. Rev. Lett. **73**, 1632 (1994)

11.   F. W. Starr, C. A. Angell, H. E. Stanley, Physica A. **323**, 51 (2003)

12. F. W. Starr, C. A. Angell, E. La Nave, S. Sastry, F. Sciortino, H. E. Stanley, Biophys. Chem. **105**, 573 (2003)

13. R. J. Speedy, P. G. Debenedetti, R. S. Smith, C. Huang, B. D. Kay, J. Chem. Phys. **105**, 240 (1996).

14. Z. Dohnálek, G. A. Kimmel, R. L. Ciolli, K. P. Stevenson, R. S. Smith, B. D. Kay, J. Chem. Phys. **112**, 5932 (2000)

15. Z. Dohnálek, Z., R. L. Ciolli, G. A. Kimmel, K. P. Stevenson, R. S. Smith, B. D. Kay, J. Chem. Phys. **110**, 5489 (1999)

16. R. S. Smith, C. Huang, E. K. L. Wong, B. D. Kay, Surf. Sci. **367**, L13 (1996)

17. R. S. Smith, B. D. Kay, Nature **398**, 788 (1999)

18. R. S. Smith, Z. Dohnálek, G. A. Kimmel, K. P. Stevenson, B. D. Kay, Chem. Phys. **258**, 291 (2000)

19. R. S. Smith, C. Huang, E. K. L. Wong, B. D. Kay, Phys. Rev. Lett. **79**, 909 (1997)

20. G. A. Kimmel, K. P. Stevenson, R. S. Smith, B. D. Kay, J. Chem. Phys. **114**, 5295 (2001)

21. G. A. Kimmel, K. P. Stevenson, Z. Dohnálek, R. S. Smith, B. D. Kay, J. Chem. Phys. **114**, 5284 (2001)

22. K. P. Stevenson, G. A. Kimmel, Z. Dohnálek, R. S. Smith, B. D. Kay, Science **283**, 1505 (1999)

23. G. A. Kimmel, N. G. Petrik, Z. Dohnálek, B. D. Kay, Phys. Rev. Lett. **95**, 166102/1-166102/4 (2005)

24. P. Ayotte, R. S. Smith, K. P. Stevenson, G. A. Kimmel, B. D. Kay, J. Geo. Res. [Planets] **106**, E12, 33387 (2001)

25. J. M. K. Donev, Q. Yu, B. R. Long, R. K. Bollinger, S. C. Fain Jr., J. Chem. Phys. **123**, 044706/1-044706/6 (2005)

26. J. L. Blanchard, J. T. Roberts, Langmuir **10**, 3303 (1994)

27. R. Souda, Phys. Rev. Lett. **93**, 235502 (2004)

28. R. Souda, Chem. Phys. Lett. **415**,146 (2005)

29. A. A. Tsekouras, M. J. Iedema, J. P. Cowin, Phys. Rev. Lett. **80**, 5798 (1998)

150

30. D. J. Safarik, R. J. Meyer, C. B. Mullins, J. Chem. Phys. **118**, 4660 (2003)

31. M. Fisher, J. P. Devlin, J. Phys. Chem. **99**, 11584 (1995)

32. M. S. Westley, G. A. Baratta, R. A. Baragiola, J. Chem. Phys. **108**, 3321 (1998)

33. D. J. Safarik, R. J. Meyer, C. B. Mullins, J. Vac. Sci. Technol. A. **19**, 1537 (2001)

34. E. A. Mason, A. P. Malinauskas, *Gas Transport in Porous Media: The Dusty-Gas Model* (Elsevier Science Publishers, Amsterdam, The Netherlands, 1983)

35. P. Adler, *Porous Media: Geometry and Transports* (Butterworth-Heinemann, Stoneham, MA, 1992)

36. R. Souda, J. Chem. Phys. **121**, 8676 (2004)

37. R. Souda, J. Phys. Chem. B. **109**, 21879 (2005)

38. R. W. Gurney, *Ionic Processes in Solution* (McGraw-Hill Book Company, Inc., New York, NY, 1953)

39. Y. Marcus, *Ion Solvation* (John Wiley and Sons Ltd., Chichester, UK/Great Britain, 1985)

40. N. S. Holmes, J. R. Sodeau, J. Phys. Chem. A. **103**, 4673 (1999)

Appendices

Appendix A1. Diffusion/Desorption Model

This is the description and the FORTRAN code for the one-dimensional desorption/diffusion used to compare experimental TPD results with simulated TPD spectra which model interlayer H_2O mixing in a **bulk** diffusion picture (no porous transport mechanism). The model [program written by Dr. T. M. Truskett at UT-Austin] simulates temperature programmed desorption (TPD) spectra allowing the user to define a TPD ramp rate and isotope film thickness. A Crank-Nicholson scheme is used to numerically solve the diffusion equation between the isotopically labeled water layers (H_2O^{16}, H_2O^{18}) while the film is desorbing and crystallizing.

The instantaneous diffusion coefficient is approximated to be the mean field diffusion coefficient between the crystalline diffusion coefficient and the amorphous diffusion coefficient at a given temperature, as shown below in Eq. (A1.1):

$$D(T) = D_{ASW}(T)X(T) + D_{CI}(T)(1 - X(T)) \qquad \text{(A1.1)}$$

where X(T) is the crystallized fraction of the ASW film, D_{ASW}(T) is the diffusion coefficient of the amorphous phase at a given temperature, D_{CI}(T) is the diffusion coefficient of the cubic ice phase at a given temperature. This approach has been used by previous investigators.[1] Crystallization kinetics of the ASW film are modeled via the Avrami equation, shown below in Eq. (A1.2):

$$X(T) = 1 - EXP(k(T)t)^n \qquad \text{(A1.2)}$$

where n is a fitting parameter (which depends on the characteristics of the crystallization process for a given substance), t is the elapsed time, and k(T) is the crystallization rate constant, defined by Eq. (A1.3).

$$k(T) = k_o EXP(E_C / RT) \qquad\qquad (A1.3)$$

Literature values of ASW and CI desorption rates[2], crystallization kinetics[3], and ASW CI diffusion parameters[4] were utilized in the simulation. The ASW self-diffusion parameters can be altered in the code to run the simulation with ASW bulk diffusion values of varying magnitudes. This program calculates simulated TPD mixing experiments which model diffusion *without* considering the effects of porous transport within the film.

Text of Program Code

```
---------------------------------------------------------------------------------------------------
C    THIS PROGRAM SOLVES THE DIFFUSION EQUATION IN ONE DIMENSION

C    USING CRANK-NICHOLSON IMPLICIT METHOD. THE MOLE FRACTION AT

C    EACH END IS DETERMINED BY A RELATION OF THE FORM AU+BU'=C

C    PARAMETERS ARE -

C    U    VALUES OF MOLE FRACTION AT BILAYER

C    T    TIME

C    TF   FINAL TIME VALUE FOR WHICH SOLUTION IS DESIRED

C    DT   DELTA T

C    DX   DELTA X

C    N    NUMBER OF X INTERVALS

C    RATIO RATIO OF DIFF(TEMP,CRYSFRAC)*DT/DX**2

C    COEF  COEFFICIENT MATRIX FOR IMPLICIT EQUATIONS

     IMPLICIT NONE
```

```fortran
      DOUBLE PRECISION   U(500),COEF(500,3),RHS(500),X(500)

      DOUBLE PRECISION  CRYSFRAC,DIFF,RATIO,AL,BL,CL,KFRAC

      DOUBLE PRECISION  T,DT,DX,TEMP,AR,BR,CR,TF,TEMPINIT

      DOUBLE PRECISION  TEMPSLOPE,DESO,BILRS,BLSUM

      DOUBLE PRECISION  RTBIS, FUNC,TEMPOLD

      DOUBLE PRECISION  DSTRUEA,DSTRUEB,TIMECONST


      INTEGER JJ,N,NP1,I,JROW,IBILRS,KK

C    THE FOLLOWING STATEMENT GIVES THE BOUNDARY CONDITION AT X=0.

C    A,B,C ON THE LEFT

C    EXAMPLE:  U'=.2*(U-15)

C    DATA AL/-.2/,BL/1.0/,CL/-3.0/

C    U=0

      DATA AL/0.0d0/,BL/1.0d0/,CL/0.0d0/

C    THE FOLLOWING STATEMENT GIVES THE BOUNDARY CONDITION AT X=1.

C    A,B,C ON THE RIGHT

C    U=1

      DATA AR/0.0d0/,BR/1.0d0/,CR/0.0d0/

      T=0.0d0

      CRYSFRAC = 0.0d0

      OPEN(UNIT=13, file='profile-time.dat')

      OPEN(UNIT=14, file='temp-time.dat')

      OPEN(UNIT=15, file='crysfrac-temp.dat')

      OPEN(UNIT=16, file='diff-temp.dat')

      OPEN(UNIT=17, file='TPD-A-temp.dat')

      OPEN(UNIT=18, file='TPD-B-temp.dat')
```

154

```fortran
OPEN(UNIT=19, file='bilayers-temp.dat')

PRINT 999

READ (*,*) TF

999  FORMAT(1X,'PLEASE TOTAL TIME OF INTEGRATION IN SECONDS')

PRINT 998

READ(*,*) N

998  FORMAT(1X,'PLEASE TYPE IN THE TOTAL NUMBER OF BILAYERS')

WRITE(*,*) 'Temperature ramp  T = To + mt'

WRITE(*,*) 'PLEASE TYPE IN To in Kelvins'

READ(*,*) Tempinit


WRITE(*,*) 'PLEASE TYPE IN m in Kelvins per second'

READ(*,*) Tempslope

JJ=0

! DX is THICKNESS BILAYERs

DX=1.d0

! DT is TIME STEP IN SECONDS

DT = .0001d0

!TIME CONSTANT OF MACHINE IN SECONDS

TIMECONST  =1.0d0


TEMP = TEMPINIT

write(14,*) T, TEMP

write(15,*) TEMP, CRYSFRAC

write(16,*) TEMP,DIFF(TEMP,CRYSFRAC)


!    DIMENSIONLESS RATIO R=Ddt/(dx)**2
```

```fortran
!    1 BILLAYER is 3.65*10**(-8) CM

     RATIO = DIFF(TEMP,CRYSFRAC)*DT/DX/DX
   :    /(3.65d0*10.d0**(-8.))**2.
     NP1=N+1
C    EVALUATE THE MESH POINTS
     DO 1 I=1,NP1
 1       X(I)=(I-1)*DX
C    COMPUTES INITIAL VALUES
     DO I=1,INT(NP1/2.)
       U(I)=1.0
     END DO
     DO I=INT(NP1/2.)+1,NP1
       U(I)=0.0d0
     END DO
!    INITIALIZE MACHINE-READ DESORPTION RATE
     DSTRUEA = 0.0d0
     DSTRUEB = 0.0d0

     write(17,*) TEMP,DESO(TEMP,CRYSFRAC)*U(NP1)
     write(18,*) TEMP,DESO(TEMP,CRYSFRAC)*(1.d0-U(NP1))
     write(19,*) TEMP,N

     do i=1,np1
       write(13,*) (i-1)*dx, u(i)
     end do
     write(13,*) ''

 555  CONTINUE
```

```
C    ESTABLISH COEFICIENT MATRIX

C    LET ALPHA=-A/B

C    LET BETA = C/B

C    AT LEFT (4-2*ALPHA*DX)*U(1,J+1)-2*U(2,J+1)=

C    2*ALPHA*DX*U(1,J)+2*U(2,J)-4*BETA*DX

C    AT INTERIOR  -U(I-1,J+1)+4*U(I,J+1)-U(I+1,J+1)=

C    U(I-1,I)+U(I+1,J)

C    AT RIGHT (-2*U(N,J+1)+(4+2*ALPHA*DX)*U(N+1,J+1)=

C    2*U(N,J)-2*ALPHA*DX*U(N+1,J)+4*BETA*DX


 7   IF((BL.LE.1.e-7).AND.(BL.GE.-1.e-7)) GO TO 10

     COEF(1,2)= 2.d0/RATIO+2.d0-2.d0*AL*DX/BL

     COEF(1,3)=-2.d0

     GO TO 20

10   COEF(1,2)=1.d0

     COEF(1,3)=0.d0

20   DO 25 I=2, N

       COEF(I,1)=-1.d0

       COEF(I,2)=2.d0/RATIO+2.d0

       COEF(I,3)=-1.d0

25   CONTINUE

     IF((BR.LE.1.e-7).AND.(BR.GE.-1.e-7)) GO TO 30

     COEF(N+1,1)=-2.

     COEF(N+1,2)= 2.d0/RATIO+2.d0+2.d0*AR*DX/BR

     GO TO 40

30   COEF(N+1,1)=0.d0

     COEF(N+1,2)=1.d0
```

```
C    GET THE LU DECOMPOSITION

 40  DO 50 I=2,NP1

     COEF(I-1,3)=COEF(I-1,3)/COEF(I-1,2)

     COEF(I,2)=COEF(I,2)-COEF(I,1)*COEF(I-1,3)

 50  CONTINUE

C    CALCULATE THE R.H.S. VECTOR - FIRST THE TOP AND BOTTOM ROWS

 55  IF((BL.LE.1.e-7).AND.(BL.GE.-1.e-7)) GO TO 60

     RHS(1)=(2./RATIO-2.+2.*AL*DX/BL)*U(1)+2.*U(2)-

    :    4.*CL*DX/BL

     GO TO 70

 60  RHS(1)=CL/AL

 70  IF((BR.LE.1.e-7).AND.(BR.GE.-1.e-7)) GO TO 80

     RHS(N+1)=2.d0*U(N)+(2.d0/RATIO-2.d0-2.d0*AR*DX/BR)*U(N+1)+

    :    4.d0*CR*DX/BR

     GO TO 90

 80  RHS(N+1)=CR/AR

C    NOW FOR THE OTHER ROWS OF THE RHS VECTOR

 90  DO 100 I=2, N

100     RHS(I)=U(I-1)+(2.d0/RATIO-2.d0)*U(I)+U(I+1)

C    GET THE SOLUTION FOR THE CURRENT TIME

     U(1)=RHS(1)/COEF(1,2)

     DO 110 I=2,NP1

110     U(I)=(RHS(I)-COEF(I,1)*U(I-1))/COEF(I,2)

     DO 120 I=1,N

        JROW=N-I+1

120        U(JROW)=U(JROW)-COEF(JROW,3)*U(JROW+1)

C    WRITE OUT THE SOLUTION
```

158

```
      T=T+DT

      JJ=JJ+1

      TEMP = TEMP + TEMPSLOPE*(DT)

      RATIO = DIFF(TEMP,CRYSFRAC)*DT/DX/DX
   :        /(3.65d0*10d0**(-8.))**2.

        IF(CRYSFRAC.GT. 0.999999d0) THEN

          CRYSFRAC=1.0d0

          GO TO 122

        END IF


        CRYSFRAC =
   :  rtbis(CRYSFRAC,1.d0,temp,tempold,crysfrac,dt)


122      DSTRUEA =  DSTRUEA +

   :         (DESO(TEMP,CRYSFRAC)*U(NP1)

   :          -DSTRUEA)*DT/TIMECONST


         DSTRUEB =  DSTRUEB +

   :         (DESO(TEMP,CRYSFRAC)*(1.d0-U(NP1))

   :          -DSTRUEB)*DT/TIMECONST


      IF (MOD(JJ,10).EQ.0) THEN

        write(14,*) T, TEMP

        write(15,*) TEMP, CRYSFRAC

        write(16,*) TEMP, DIFF(TEMP,CRYSFRAC)
C        write(17,*) TEMP, DESO(TEMP,CRYSFRAC)*U(NP1)
C        write(18,*) TEMP, DESO(TEMP,CRYSFRAC)*(1-U(NP1))
```

159

```fortran
    write(17,*) TEMP, DSTRUEA

    write(18,*) TEMP, DSTRUEB

    write(19,*) TEMP,N

END IF

IF (MOD(JJ,500).EQ.0) THEN

do i=1,np1

   write(13,*) (i-1)*dx, u(i)

end do

write(13,*) ' '

END IF


BILRS = BILRS + DESO(TEMP,CRYSFRAC)*DT

IF (INT(BILRS).GT.IBILRS) THEN

   IBILRS=INT(BILRS)

   N=N-1

   NP1 = NP1 -1

   IF (N.LT.1) GO TO 777

   GO TO 555

END IF

IF(T.LT.TF) GO TO 7

777     DO KK=1,75000


T=T+DT

JJ=JJ+1

TEMP = TEMP + TEMPSLOPE*(DT)

RATIO = DIFF(TEMP,CRYSFRAC)*DT/DX/DX
```

```fortran
     :          /(3.65d0*10d0**(-8.))**2.

            IF(CRYSFRAC.GT. 0.999999d0) THEN

              CRYSFRAC=1.0d0

              GO TO 222

            END IF

            CRYSFRAC =

     :  rtbis(CRYSFRAC,1.d0,temp,tempold,crysfrac,dt)


222         DSTRUEA =  DSTRUEA +

     :          (0.d0

     :           -DSTRUEA)*DT/TIMECONST


            DSTRUEB =  DSTRUEB +

     :          (0.d0

     :           -DSTRUEB)*DT/TIMECONST

            IF (MOD(JJ,10).EQ.0) THEN

              write(14,*) T, TEMP

              write(15,*) TEMP, CRYSFRAC

              write(16,*) TEMP, DIFF(TEMP,CRYSFRAC)

C          write(17,*) TEMP, DESO(TEMP,CRYSFRAC)*U(NP1)

C          write(18,*) TEMP, DESO(TEMP,CRYSFRAC)*(1-U(NP1))


              write(17,*) TEMP, DSTRUEA

              write(18,*) TEMP, DSTRUEB

              write(19,*) TEMP,N

            END IF

            IF (MOD(JJ,500).EQ.0) THEN

            do i=1,np1
```

```fortran
    write(13,*) (i-1)*dx, u(i)

    end do

    write(13,*) ' '

    END IF

    END DO

    CLOSE(UNIT=13)

      STOP

      END


DOUBLE PRECISION FUNCTION KFRAC(TEMP)

IMPLICIT NONE

DOUBLE PRECISION kcrys

DOUBLE PRECISION TEMP

DOUBLE PRECISION Ecrys

PARAMETER (Ecrys =84000.d0) !J/mol

DOUBLE PRECISION R

PARAMETER (R = 8.3144d0) !J/mol*K

kcrys = 250.0d0*10.d0**(25.)  !sec^-1


KFRAC = kcrys*EXP(-Ecrys/(R*TEMP))

RETURN

END


DOUBLE PRECISION FUNCTION DIFF(TEMP,CRYSFRAC)

IMPLICIT NONE

DOUBLE PRECISION TEMP

DOUBLE PRECISION DOA

DOUBLE PRECISION DOX
```

```
      PARAMETER (DOX = 150.d0) !cm^2/sec

      DOUBLE PRECISION EOA

      PARAMETER (EOA = 170000.d0) !J/mol

      DOUBLE PRECISION EOX

      PARAMETER (EOX = 58600.d0) !J/mol

      DOUBLE PRECISION R

      PARAMETER (R = 8.3144d0) !J/mol*K

      DOUBLE PRECISION CRYSFRAC


C     DOA = 2.9d0*10.d0**(43.)  !cm^2/sec

      DOA = 1.55d0*10.d0**(44.)


      DIFF = (1.d0-CRYSFRAC)*DOA*EXP(-EOA/(R*TEMP))+
     :   CRYSFRAC*DOX*EXP(-EOX/(R*TEMP))


      RETURN
      END
      DOUBLE PRECISION FUNCTION DESO(TEMP,CRYSFRAC)
      IMPLICIT NONE
      DOUBLE PRECISION TEMP
      DOUBLE PRECISION NUA
      DOUBLE PRECISION EDESA
      PARAMETER (EDESA = 46900.d0) !J/mol
      DOUBLE PRECISION NUX
      DOUBLE PRECISION EDESX
      PARAMETER (EDESX = 48250.d0) !J/mol
      DOUBLE PRECISION R
      PARAMETER (R = 8.3144d0) !J/mol*K
```

```fortran
      DOUBLE PRECISION CRYSFRAC

      NUA = 3.26d0*10.d0**(15.) !bilayers/sec

      NUX = 3.99d0*10.d0**(15.) !bilayers/sec

      DESO = (1.d0-CRYSFRAC)*NUA*EXP(-EDESA/(R*TEMP))+

     :    CRYSFRAC*NUX*EXP(-EDESX/(R*TEMP))


      RETURN
      END
      DOUBLE PRECISION FUNCTION rtbis(x1,x2,temi1,temi,ci,dt)
      IMPLICIT NONE
      INTEGER JMAX
      DOUBLE PRECISION x1,x2,xacc,func
      DOUBLE PRECISION kfrac
      PARAMETER (JMAX=40)
      INTEGER j
      DOUBLE PRECISION dx,f,fmid,xmid
      DOUBLE PRECISION temi1,temi,ci,dt
      xacc = .00000001d0
      fmid=func(x2,ci,dt,kfrac(temi),kfrac(temi1))
      f=func (x1,ci,dt,kfrac(temi),kfrac(temi1))
      if(f*fmid.ge.0.) pause 'root must be bracketed in rtbis'
      if(f.lt.0.)then
        rtbis=x1
        dx=x2-x1
      else
        rtbis=x2
        dx=x1-x2
```

```fortran
      endif

      do 11 j=1,JMAX

       dx=dx*.5

       xmid=rtbis+dx

       fmid=func(xmid,ci,dt,kfrac(temi),kfrac(temi1))

       if(fmid.le.0.)rtbis=xmid

       if(abs(dx).lt.xacc .or. fmid.eq.0.) return

11    continue

      pause 'too many bisections in rtbis'

      RETURN

      END

      DOUBLE PRECISION FUNCTION FUNC(ci1,ci,dt,ki,ki1)

      IMPLICIT NONE

      DOUBLE PRECISION ci1,ci,dt,ki,ki1

      FUNC = ci - ci1 + 2.0d0*dt*

     :    (ki*(-Log(1.d0-ci))**(.75d0)

     :    *(1.d0-ci)+ki1*(-Log(1.d0-ci1))**(.75d0)*(1.d0-ci1))

      RETURN

      END

C      END OF CODE
```

References

1.   R. S. Smith, B. D. Kay, Nature, **398**, 788 (1999)

2.   R. J. Speedy, P. G. Debenedetti, R. S. Smith, C. Huang, B. D. Kay, J. Chem. Phys. **105**, 240 (1996)

3.   Z. Dohnálek, G. A. Kimmel, R. L. Ciolli, K. P. Stevenson, R. S. Smith, B. D. Kay, J. Chem. Phys. **112**, 5932 (2000)

4.   K. Goto, T. Hondoh, A. Higashi, Jpn J. Appl. Phys. **25**, 351 (1986)

Appendix A2. Correcting Desorption Spectra For Water Fragmentation in Quadrupole Mass Spectrometer

Using isotopically labeled $H_2^{16}O$, $H_2^{18}O$ water molecules allows for studies of self-transport within structured ASW films using temperature programmed desorption (TPD) techniques since the two species have virtually identical desorption and crystallization kinetics. However, TPD data in which the two isotopically labeled molecules are employed must be corrected for fragmentation of water molecules within the quadrupole mass spectrometer (QMS). Discussed below is the method by which this is accomplished.

Water molecules fragment primarily into O^+, OH^+, and H_2O^+ species; producing mass signals m/z~16, 17, and 18 for $H_2^{16}O$ and m/z~18, 19, 20 for $H_2^{18}O$, respectively. Since the $H_2^{18}O$ liquid samples used (Isotec, > 95-98 atom % pure) may contain 2-5 atom % $H_2^{16}O$, there may also be a m/z~16, 17, 18 component to the $H_2^{18}O$ beam. Additionally, the presence of trace amounts of $H_2^{18}O$ present in the nozzle during $H_2^{16}O$ dosing may contribute to trace amounts of $H_2^{18}O$ (and hence, m/z~18, 19, 20) in the $H_2^{16}O$ beam (if the same nozzle is employed for dosing of both species). Thus, the *actual* $H_2^{18}O$ and $H_2^{16}O$ signals from desorption experiments are a linear combination of the observed m/z~18 and m/z~20 signals of the raw TPD spectra, with components weighted by their relative concentration and ionization probabilities in the $H_2^{16}O$ and $H_2^{18}O$ beams. This relationship is displayed in Equations (A2.1) and (A2.2) below:

$$I_{18,raw} = [S_{18}H_2^{16}O]\, I_{H_2^{16}O} + [S_{18}H_2^{18}O]\, I_{H_2^{18}O} \qquad (A2.1)$$

$$I_{20,raw} = [S_{20}H_2^{16}O]\, I_{H_2^{16}O} + [S_{20}H_2^{18}O]I_{H_2^{18}O} \qquad (A2.2)$$

where $S_{18}H_2{}^{16}O$, $S_{18}H_2{}^{18}O$, are the relative concentrations of m/z~18 in the $H_2{}^{16}O$ and $H_2{}^{18}O$ beams, respectively; and $S_{20}H_2{}^{16}O$, and $S_{20}H_2{}^{18}O$ are the relative concentrations of m/z~20 in the $H_2{}^{16}O$ and $H_2{}^{18}O$ beams, respectively. $I_{18,raw}$ and $I_{20,raw}$ represent the raw m/z~18 and m/z~20 signals measured in a TPD experiment, respectively; $I_{H_2{}^{16}O}$ and $I_{H_2{}^{18}O}$ are the actual (corrected) $H_2{}^{16}O$ and $H_2{}^{18}O$ signals, respectively. [Note: If separate nozzles and plumbing are used to dose $H_2{}^{16}O$ and $H_2{}^{18}O$, the $S_{20}H_2{}^{16}O$ term can be neglected ($S_{20}H_2{}^{16}O$=0)]

Cracking patterns were obtained by analyzing $H_2{}^{16}O$ and $H_2{}^{18}O$ beams directed into the QMS, and these values were used to estimate the $S_{18}H_2{}^{16}O$, $S_{20}H_2{}^{18}O$, $S_{18}H_2{}^{18}O$, and $S_{20}H_2{}^{18}O$ values of Eqs. (A2.1) and (A2.2). A typical beam analysis experiment is shown in Figure A2.1. These estimates, along with Eqs. (A2.1) and (A2.2), were used to correct the raw spectra. These corrected spectra were then integrated (and normalized to the dosed coverage) to give the resulting desorption spectra in terms of H_2O desorption rate (BL/sec). $H_2{}^{16}O$ impurities were generally found to be negligible in the $H_2{}^{18}O$ beams (m/z~16, 17 signals were very small), the majority of the m/z~18 signal appearing to arise from fragmentation of the $H_2{}^{18}O$. Thus, impurities in the $H_2{}^{18}O$ beam were ignored [an assumption, as we will show, which proved to have a negligible effect on the corrected spectra]. $H_2{}^{18}O$ impurities in the $H_2{}^{16}O$ beam were found to be dependent with "pump out" (pressure to which nozzle was pumped prior to $H_2{}^{16}O$ dosing) of the nozzle between dosings, generally varying between S=0 to 0.05. Consequently, care was taken to keep nozzle "pump out" times very consistent from experiment to experiment. Hence, we argue that there is little $H_2{}^{16}O$ contamination in our $H_2{}^{18}O$ beam and that the small m/z~20 signal in the $H_2{}^{16}O$ beam is due to residual labeled water ($H_2{}^{18}O$) left in the lines prior to the $H_2{}^{16}O$ dose. Beam fragmentation pattern analysis was conducted periodically

167

Figure A2.1 QMS Analysis of $H_2^{16}O$ and $H_2^{18}O$ Molecular Beams

Displayed in Figure A2.1 are two examples of experiments conducted to determine the fragmentation patterns of the $H_2^{18}O$ and $H_2^{16}O$ molecules. Fragmentation patterns are estimated by directing pure $H_2^{16}O$ (upper panel) and pure $H_2^{18}O$ (lower panel) beams towards the QMS ionizing region and monitoring the resulting mass fragments. In both cases shown (upper and lower panel) the respective H_2O beam was directed into the QMS ionizing region at t~10 sec. These signals were then analyzed to estimate the contribution of both $H_2^{18}O$ and $H_2^{16}O$ molecules to the m/z~18 and m/z~20 signals observed during a TPD mixing experiments [Results shown in Table A2.1]. $H_2^{18}O$ beams generally exhibited negligible m/z~16, m/z~17 signals, indicating low amounts of $H_2^{16}O$ impurities. $H_2^{16}O$ beams exhibited trace amounts of m/z~20 impurities, presumably due to presence of trace amounts of $H_2^{18}O$ on nozzle surfaces. This amount was sensitive to nozzle pump-out times (the amount time nozzle was allowed to evacuate residual gas), and hence care was taken to maintain consistent pump-out times during experiment. Using our standard pump out time, $S_{20}H_2^{16}O$ value typically was near ~0.05, on average.

QMS Signal (a.u.) x(10^5)

2e+0

~1.78

$S_{18},H_2{}^{16}O \sim \dfrac{1.78}{(1.78+0.16+0.13+0.01+0.02)}$

$S_{18},H_2{}^{16}O \sim 0.83$

$S_{20},H_2{}^{16}O \sim \dfrac{0.16}{(1.78+0.16+0.13+0.01+0.02)}$

$S_{20},H_2{}^{16}O \sim 0.08$ *(use ~0.05)*

	m/z~16
	m/z~17
	m/z~18
	m/z~19
	m/z~20

$H_2{}^{16}O$ Beam
(Beam on at t=10 sec)

m/z~16, (~0.01)
m/z~19, (~0.02)

~0.16
~0.13
0

0   5   10   15   20

2e+0

~1.83

$S_{18},H_2{}^{18}O \sim \dfrac{0.21}{(1.83+0.35+0.21)}$

$S_{18},H_2{}^{18}O \sim 0.09$

$S_{20},H_2{}^{18}O \sim \dfrac{1.83}{(1.83+0.35+0.21)}$

$S_{20},H_2{}^{18}O \sim 0.77$

	m/z~18
	m/z~19
	m/z~20

$H_2{}^{18}O$ Beam
(Beam on at t=10 sec)

~0.35
~0.21
0

0   5   10   15   20

Time (sec)

169

Table A2.1. Typical S Values For Spectra Correction

$S_{18,H_2^{18}O}$	$S_{20,H_2^{18}O}$	$S_{18,H_2^{16}O}$	$S_{20,H_2^{16}O}$
0.09	0.77	0.83	~0.05

throughout the course of the study, usually when a new batch of $H_2^{18}O$ was used for the experiment. Overall, it was found that the "corrected" TPD spectra are rather insensitive to minor variations in S values and beam impurities. As a demonstration of this, a typical TPD mixing experiment (30 BL $H_2^{16}O$ ASW on 30 BL $H_2^{18}O$ ASW heated at 0.6 K/s) is analyzed with various values for S. This analysis is presented in Figure A2.2, which is shown along with the raw data obtained for the experiment. As the figure illustrates, the correction technique is rather insensitive to minor variations in S values and to minor variations in beam impurity concentrations. Our spectra are in generally good agreement with those found in the literature.[2] Furthermore, comparisons with the raw data spectra show that the large qualitative features of the spectra remain unchanged as a result of the correction. Hence, none of the conclusions drawn from our spectra would likely be changed by the small differences in spectra that may arise due to errors in correcting for mass fragmentation.

References

(1)   NIST Chemistry Webbook, http://webbook.nist.gov/chemistry/, Accessed February 1, 2006

(2)   R. S. Smith, B. D. Kay, Nature, **398**, 788 (1999)

Figure A2.2. TPD Mixing Experiment Calculations

Shown in Figure A2.2(a)-(f) are examples of a typical TPD mixing experiment (30 BL $H_2^{16}O$ ASW grown atop 30BL $H_2^{18}O$ ASW) heated at a rate of 0.6 K/s, corrected using various S parameters. Figures A2.2(a) shows the raw, uncorrected TPD spectra, normalized to the multilayer coverage. Figures A2.2(b)-(d) represent the *same* experiment of A2.2(a), corrected with different S values; the TPD spectra of (b) were corrected using experimentally determined S values; the TPD spectra of (c) were corrected ignoring $H_2^{18}O$ nozzle contamination; the TPD spectra of (d) were corrected using NIST Webbook[1] S values; the TPD spectra of (e) represents a spectra corrected assuming an $H_2^{16}O$ impurity of ~5% in the $H_2^{18}O$ beam. Figure A2.2(f) is an identical TPD experiment (30 BL $H_2^{16}O$ ASW grown atop 30BL $H_2^{18}O$) conducted with a **different** batch of $H_2^{18}O$ (and slightly different QMS conditions) than the experiment of Figures A2.2(a)-(e). These differences resulted in slightly different estimated S values. The raw, uncorrected data for this experiment is also shown in Fig. A2.2(f) inset. Each mass-corrected TPD spectra shows the S values used to analyze the data. This exercise illustrates that (1) minor variations in S values does not significantly alter the nature of the TPD data, (2) correction of the spectra for mass fragmentation does not alter the qualitative nature of the raw spectra, and (3) the correction procedure, when applied to identical experiments under different QMS conditions and $H_2^{18}O$ batches, produces fairly good agreement between TPD spectra.
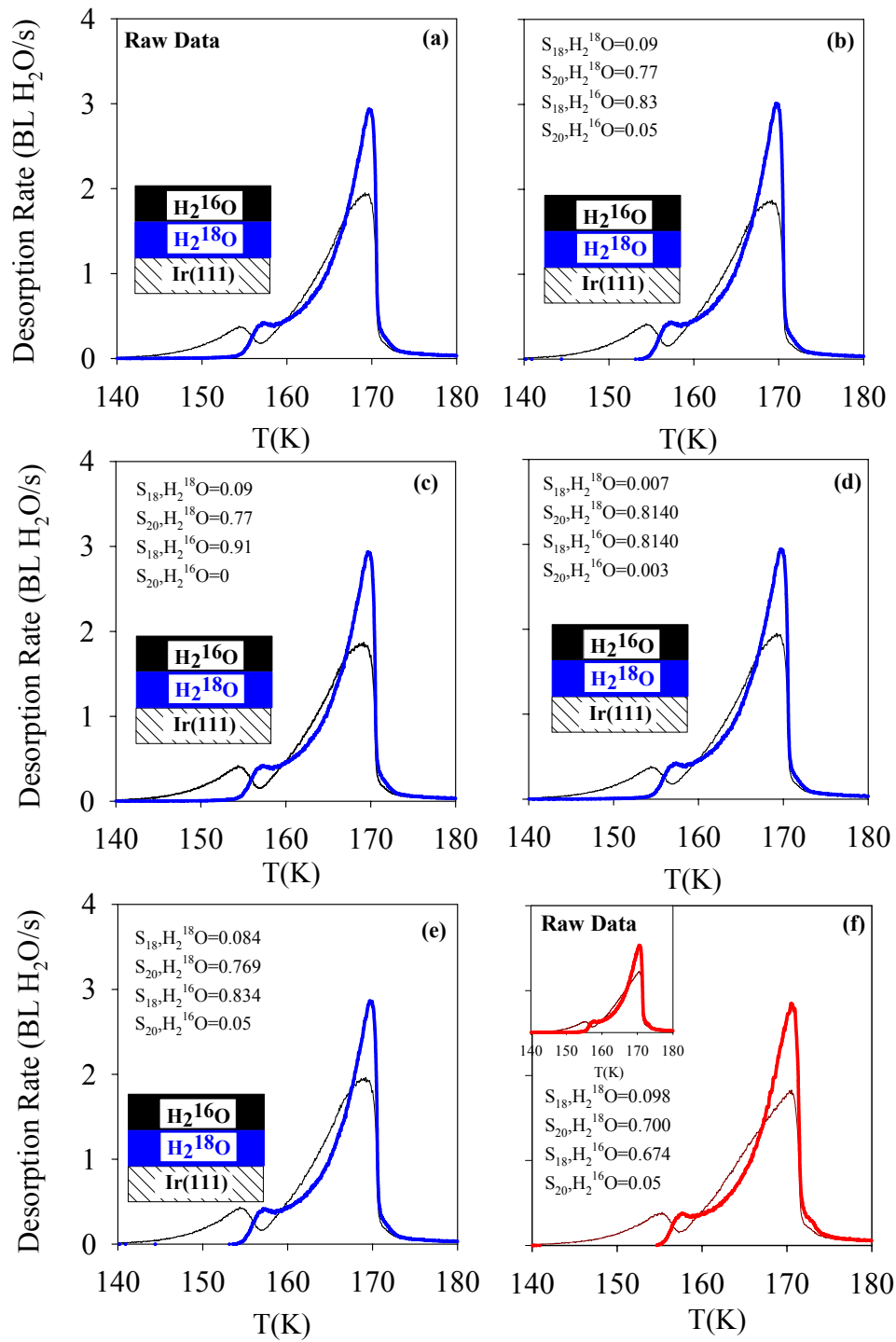
Bibliography

G. Adam, J. H. Gibbs, J. Chem. Phys. **43**, 139 (1965)

P. Adler, *Porous Media: Geometry and Transports* (Butterworth-Heinemann, Stoneham, MA, 1992)

O. Andersson, H. Suga, Phys. Rev. B **65,** 140201 (2002)

C. A. Angell, E. D. Finch, L. A. Woolf, P. Bach, J. Chem. Phys. **65**, 3063 (1976)

C. A. Angell, J. Phys. Chem. **97**, 6339 (1993)

C. A. Angell, Science **267**, 1924 (1995)

C. A. Angell, Chem. Rev. **102**, 2627 (2002)

C. A. Angell, Annu. Rev. Phys. Chem. **55**, 559 (2004)

C. A. Angell, E. J. Sare, J. Chem. Phys. **52**, 1058 (1970)

P. Ayotte, R. S. Smith, K. P. Stevenson, G. A. Kimmel, B. D. Kay, J. Geo. Research [Planets], **106**, E12 33387 (2001)

N. Barton, B. Rowland, J. P. Devlin, J. Phys. Chem. **97**, 5848 (1993)

R. Bergman, J. Swenson, Nature, **403**, 283 (2000)

D. Bertolini, M. Cassettari, G. Salvetti, J. Chem. Phys. **76**, 3285 (1982)

U. M. Biermann, J. N. Crowley, T. Huthwelker, G. K. Moortgat, P. J. Crutzen, Th. Peter, Geo. Res. Lett. 25, 3939 (1998)

D. Blake, L. Allamandola, S. Sandford, D. Hudgins, F. Freund, Science **254**, 548 (1991)

J. L. Blanchard, J. T. Roberts, Langmuir **10**, 3303 (1994)

A. Botti, F. Bruni, M. A. Ricci, A. K. Soper, J. Chem. Phys. **121**, 7840 (2004)

D. E. Brown, S. M. George, J. Phys. Chem. **100**, 15460 (1996)

P. Brügeller, E. Mayer, Nature **288**, 569 (1980)

F. Bruni, M. A. Ricci, A. K. Soper, J. Chem. Phys. **114**, 8056 (2001)

E. F. Burton, W. F. Oliver, Proc. Roy. Soc. Lond. A. **153**, 166 (1935)

S. Cerveny, G. A. Schwartz, R. Bergman, J. Swenson, Phys. Rev. Lett. **93**, 245702/1 (2004)

J. C. L. Cornish, N. R Avery, Surf. Sci. **235**, 209 (1990)

J.E. Davis, S.G. Karseboom, P.D. Nolan, C.B. Mullins, J. Chem Phys., **105**, 8362 (1996)

P. G. Debenedetti, *Metastable Liquids: Concepts and Principles* (Princeton University Press, Princeton, NJ, 1996)

P. G. Debenedetti, F. H. Stillinger, Nature **410**, 259 (2001)

P. G. Debenedetti, J. Phys. Cond. Matt. **15**, R1669 (2003)

P. G. Debenedetti, H. E. Stanley, *Physics Today*, June 2003, p. 40

A. H. Delsemme, J. Phys. Chem. **87**, 4214, (1983)

C. Delval, M. J. Rossi, J. Phys. Chem. A. **109**, 7151 (2005)

T. Deshler, Th. Peter, R. Müller, P. Crutzen, Geophys. Res. Lett. **21**, 1327 (1994)

D. B. Dickens, J. J. Sloan, J. Phys. Chem. A. **106**, 10543 (2002)

Z. Dohnálek, R. L. Ciolli, G. A. Kimmel, K.P. Stevenson, R. S. Smith, B. D. Kay, J. Chem. Phys. **110**, 5489 (1999)

Z. Dohnálek, G. A. Kimmel, R. L. Ciolli, K. P. Stevenson, R. S. Smith, B. D. Kay, J. Chem. Phys. **112**, 5932 (2000)

Z. Dohnálek, G. A. Kimmel, P. Ayotte, R. S. Smith, B. D. Kay, J. Chem. Phys. **118**, 364 (2003)

J. M. K. Donev, Q. Yu, B. R. Long, R. K. Bollinger, S. C. Fain Jr., J. Chem. Phys. **123**, 044706/1 (2005)

A. Faraone, L. Liu, C.-Y. Mou, C.-W. Yen, S.-H. Chen, J. Chem. Phys. **121**, 10843 (2004)

W. Fink, E. W. Lang, J. Phys. Chem. **92**, 6440 (1988)

M. Fisher, J. P. Devlin, J. Phys. Chem. **99**, 11584 (1995)

R. A. Friedel, J. L. Schultz, A. G. Sharkey Jr., Anal. Chem. **31**, 1128 (1959)

174

T. Fujitani, I. Nakamura, Y. Kobayashi, A. Takahashi, M. Haneda, H. Hamada, J. Phys. Chem. B. **109**, 17603 (2005)

P. Gallo, F. Sciortino, P. Tartaglia, S-.H. Chen, Phys. Rev. Lett. **76**, 2730 (1996)

J. A. Ghormley, J. Chem. Phys. **48**, 503 (1968)

J. A. Ghormley, C. J. Hochanadel, Science **171**, 62 (1971)

J. Gmehling, U. Oken, *VLE Data Collection Supp. 2: Aqueous Systems*, (Scholium Intl. 1977)

K. Goto, T. Hondoh, A. Higashi, Jpn J. Appl. Phys. **25**, 351 (1986)

K. T. Gillen, D. C. Douglass, M. J. R. Hoch, J. Chem. Phys. **57**, 5117 (1972)

J. Guenster, G. Liu, J. Stultz, S. Krischok, D. W. Goodman, J. Phys. Chem. B. **104**, 5738 (2000)

A. Hallbrucker, E. Mayer, G. P. Johari, J. Phys. Chem. **93**, 4986 (1989)

D. Hanson, K. Mauersberger, J. Phys. Chem. **92**, 6167 (1988)

H. G. Heide, Ultramicroscopy **14**, 271 (1984)

M. Hemmati, C. T. Moynihan, C. A. Angell, J. Chem. Phys. **115**, 6663 (2001)

K. Hofer, G. Astl, E. Mayer, G. P. Johari, J. Phys. Chem. **95**, 10777 (1991)

N. S. Holmes, J. R. Sodeau, J. Phys. Chem. A. **103**, 4673 (1999)

K. Ito, C. T. Moynihan, C. A. Angell, Nature **398**, 492 (1999)

P. Jenniskens, D. F. Blake, Science **265**, 5173 (1994)

P. Jenniskens, D. F. Blake, Planet. Space Sci. **44**, 711 (1996)

P. Jenniskens, D. F. Blake, Astrophys. J. **473**, 1104 (1996)

P. Jenniskens, S. F. Banham, D. F. Blake, M. R. S. Mccoustra, J. Chem. Phys. **107**, 1232 (1997)

G. P. Johari, A. Hallbrucker, E. Mayer, Nature **330**, 552 (1987)

G. P. Johari, A. Hallbrucker, E. Mayer, J. Chem. Phys. **95**, 2955 (1991)

G. P. Johari, A. Hallbrucker, E. Mayer, J. Chem. Phys. **97**, 5851, (1992)

G. P. Johari, J. Chem. Phys. **105**, 7079 (1996)

G. P. Johari, J. Phys. Chem. B. **102**, 4711 (1998)

G. P. Johari, J. Chem. Phys. **116**, 8067 (2002)

G. P. Johari, J. Chem. Phys. **119**, 2935 (2003)

G. P. Johari, J. Chem. Phys. B. **107**, 9063 (2003)

G. P. Johari, J. Chem. Phys. **123**, 016102 (2005)

G. P. Johari, J. Chem. Phys. **122**, 144508 (2005)

G. P. Johari, Phys. Chem. Chem. Phys. **7**, 1091 (2005)

H. Kanno, C. A. Angell, J. Phys. Chem. **81**, 2639 (1977)

W. Kauzmann, Chem. Rev. **43**, 219 (1948)

S. Khatua, G. Held, D.A. King, Surf. Sci. **586**, 1 (2005)

G. A. Kimmel, K. P. Stevenson, Z. Dohnálek, R. S. Smith, B. D. Kay, J. Chem. Phys. **114**, 5284 (2001)

G. A. Kimmel, Z. Dohnálek, K. P. Stevenson, R. S. Smith, B. D. Kay, J. Chem. Phys. **114**, 5295 (2001)

G. A. Kimmel, N. G. Petrik, Z. Dohnálek, B. D. Kay, Phys. Rev. Lett. **95**, 166102/1 (2005)

D. A. King, M. G. Wells, Proc. R. Soc. London Ser. A. **339**, 245 (1974)

J. Klinger, J. Phys. Chem. **87**, 4209 (1983)

B. G. Koehler, A. M. Middlebrook, M. A. Tolbert, J. Geophys. Res. **97**, 8065 (1992)

B. G. Koehler, Int. J. Chem. Kinetics. **33**, 295 (2001)

I. Kohl, L. Bachmann, A. Hallbrucker, E. Mayer, T. Loerting, Phys. Chem. Chem. Phys. **7**, 3210 (2005)

I. Kohl, L. Bachmann, E. Mayer, A. Hallbrucker, T. Loerting, Nature **435**, E1 (2005)

T. Koop, B. Luo, A. Tsias, T. Peter, Nature **406**, 611 (2000)

E. W. Lang, S. Bradl, W. Fink, H. Radkowitsch, D. Girlich,J. Phys. Cond. Matt. **2**, SA195 (1990)

D. Laufer, E. Kochavi, A. Bar-Nun, Phys. Rev. B. **36**, 9219 (1987)

R. Leberman, A. K. Soper, Nature **378**, 364 (1995)

M. Leuchs, G. Zundel, J. Phys. Chem. **82**, 1632 (1978)

L. Liu, S.-H. Chen, A. Faraone, C.-W. Yen, C.-Y. Mou, Phys. Rev. Lett. **95**, 117802/1 (2005)

F. E. Livingston, G. C. Whipple, S. M. George, J. Phys. Chem. B. **101**, 6127 (1997)

F. E. Livingston, S. M. George, J. Phys. Chem. A. **102**, 10280 (1998)

F. E. Livingston, S. M. George, J. Phys. Chem. B. **103**, 4366 (1999)

F. E. Livingston, J. A. Smith, J. Phys. Chem. A. **106**, 6309 (2002)

P. Löfgren, P. Ahlström, D. V. Chakarov, J. Lausmaa, B. Kasemo, Surf. Sci. **367**, L19 (1996)

D. R. MacFarlane, C. A. Angell, J. Phys. Chem. **88**, 759 (1984)

Y. Marcus, *Ion Solvation* (John Wiley and Sons Ltd., Chichester, UK/Great Britain, 1985)

E. A. Mason, A. P. Malinauskas, *Gas Transport in Porous Media: The Dusty-Gas Model* (Elsevier Science Publishers, Amsterdam, The Netherlands, 1983)

S. M. McClure, E. Barlow, M. Akin, D. J. Safarik, T. M. Truskett, C. B Mullins, *in preparation*

S. M. McClure, D. J. Safarik, T. M. Truskett, C. B. Mullins, submitted March 2006

J. A. McMillan, S. C. Los, Nature **206**, 806 (1965)

P. R. McCurdy, W. P. Hess, S. S. Xantheas, J. Phys. Chem. A. **106**, 7628 (2002)

A. M. Middlebrook, M. A. Tolbert, K. Drdla, Geophys. Res. Lett. **23**, 2145 (1996)

G. A. Miller, D. A. Carpenter, J. Chem. Eng. Data **9**, 371 (1964)

A. Minoguchi, R. Richert, C. A. Angell, Phys. Rev. Lett. **93**, 215703-1 (2004)

A. Minoguchi, R. Richert, C. A. Angell, J. Phys. Chem. B. **108**, 19825 (2004)
177

O. Mishima, L. D. Calvert, E. Whalley, Nature **310**, 393 (1984)

O. Mishima, L. D. Calvert, E. Whalley, Nature **314**, 76 (1985)

O. Mishima, H. E. Stanley, Nature **396**, 329 (1998)

H. Miura, H. Ohta, N. Okamoto, T. Kaga, Appl. Phys. Lett. **60**, 2746 (1992)

H. Miura, N. Okamoto, J. Appl. Phys. **75**, 4747 (1994)

L.-A. Näslund, D. C. Edwards, P. Wernet, U. Bergmann, H. Ogasawara, L.G. M. Pettersson, S. Myeni, A. Nilsson, J. Phys. Chem. A. **109**, 5995 (2005)

A. W. Omta, M. F. Kropman, S. Woutersen, H. J. Bakker, J. Chem. Phys. **119**, 12457 (2003)

A. Omta, M. F. Kropman, S. Wouterson, H. J. Bakker, Science **301**, 347 (2003)

D. Patschek, A. Geiger, J. Phys. Chem. B. **103**, 4139 (1999)

T. Peter, R. Müller, P. J. Crutzen, T. Deshler, Geophys. Res. Lett. **21**, 1331 (1994)

P. H. Poole, F. Sciortino, U. Essmann, H. E. Stanley, Nature **360**, 324 (1992)

P. H. Poole, F. Sciortino, T. Grande, H. E. Stanley, C. A. Angell, Phys. Rev. Lett. **73**, 1632 (1994)

D. Prialnik, A. Bar-nun, Astron. Astrophys. **258**, L9 (1992)

D. Prialnik, U. Egozi, A. Bar-nun, M. Podolak, Y. Greenzweig, Icarus **106**, 499 (1993)

W. S. Price, H. Ide, Y. Arata, O. Söderman, J. Phys. Chem. B. **104**, 5874 (2000)

F. X. Prielmeier, E. W. Lang, R. J. Speedy, H.-D. Lüdemann, Phys. Rev. Lett. **59**, 1128 (1987)

H. R. Pruppacher, J. Chem. Phys. **56**, 101 (1972)

N. F. Ramsey, *Molecular Beams*, Cambridge Univ. Press, (1960)

H. Reinhardt, M. Fida, R. Zellner, J. Mol. Structure **661**, 567 (2003)

G. Ritzhaupt, J. P. Devlin, J. Phys. Chem. **95**, 90 (1991)

G. Ritzhaupt, J. P. Devlin, J. Phys. Chem. **81**, 521 (1977)

N. J. Sack, R. A. Baragiola, Phys. Rev. B.: Cond. Matt. **48**, 9973 (1993)

D. J. Safarik, R. J. Meyer, C. B. Mullins, J. Vac. Sci. Technol. A. **19**, 1537 (2001)

D. J. Safarik, R. J. Meyer, C. B. Mullins, J. Chem. Phys. **118**, 4660 (2003)

I. Saika-Voivod, P. H. Poole, F.Sciortino, Nature **412**, 514 (2001)

N. Sartori, J. Bednar, J. Dubochet, J. Micros. **182**, 163 (1996)

K. Satoh, H. Kanno, Bull. Chem. Soc. Jpn. **55**, 1645 (1982)

F. Sciortino, A. Geiger, H. E. Stanley Nature **354**, 218 (1991)

F. Sciortino, A. Geiger, H. E. Stanley, J. Chem. Phys. **96**, 3857 (1992)

F. Sciortino, P. Gallo, P. Tartaglia, H.-S. Chen, Phys. Rev. E. **54**, 6331 (1996)

F. Sciortino, L. Fabbian, H.-S. Chen, P. Tartaglia, Phys. Rev. E. **56**, 5937 (1997)

R. Smoluchowski, Astrophysical J. **244**, L31 (1981)

R. H. Smith, M.-T. Leu, L. F. Keyser, J. Phys. Chem. **95**, 5924 (1991)

R. S. Smith, C. Huang, E. K. L. Wong, B. D. Kay, Surf. Sci. **367**, L13 (1996)

R. S. Smith, C. Huang, E. K. L. Wong, B.D. Kay, Phys. Rev. Lett. **79**, 909 (1997)

R. S. Smith, B. D. Kay, Nature **398**, 788 (1999)

R. S. Smith, Z. Dohnálek, G. A. Kimmel, K. P. Stevenson, B. D. Kay, Chem. Phys. **258**, 291 (2000)

R. Smoluchowski, Astrophysical J. **244**, L31 (1981)

R. Souda, Phys. Rev. Lett. **93**, 235502/1, (2004)

R. Souda, J. Chem. Phys. **121**, 8676 (2004)

R. Souda, J. Phys. Chem. B. **109**, 21879 (2005)

R. Souda, Chem. Phys. Lett. **415**, 146 (2005)

R. J. Speedy, P. G. Debenedetti, R. S. Smith, C. Huang, B. D. Kay, J. Chem. Phys. **105**, 240 (1996)

H. E. Stanley, S. V. Buldyrev, M. Canpolat, O. Mishima, M. R. Sadr-Lahijany, A. Scala, F. W. Starr, Phys. Chem. Chem. Phys. **2**, 1551 (2000)

179

F. W. Starr, F. Sciortino, H. E. Stanley, Phys. Rev. E. **60**, 6757 (1999)

F. W. Starr, S. Harrington, F. Sciortino, H. E. Stanley, Phys. Rev. Lett. **82**, 3629 (1999)

F. W. Starr, C. A. Angell, H. E. Stanley, Physica A. **323**, 51 (2003)

F. W. Starr, C. A. Angell, E. La Nave, S. Sastry, F. Sciortino, H. E. Stanley, Biophys. Chem. **105**, 573 (2003)

K. P. Stevenson, G. A. Kimmel, Z. Dohnálek, R. S. Smith, B. D. Kay, Science **283**, 1505 (1999)

M. Sugisaki, H. Suga, S. Seki, J. Chem. Soc. Jpn. **41**, 2591 (1968)

J. Swenson, J. Phys. Cond. Matt. **16**, S5317 (2004)

P. A. Thiel, T. E. Madey, Surf. Sci. Rep. **7**, 211 (1987)

R. Tisdale, A. M. Middlebrook, A. J. Prenni, M. A. Tolbert, J. Phys. Chem. A, **101**, 2112 (1997)

M. A. Tolbert, A. M. Middlebrook, J. Geophys. Res. **95** 22423 (1990)

T. M. Truskett, K. A. Dill, J. Phys. Chem. B. **106**, 11829 (2002)

T. M. Truskett, K. A. Dill, Biophys. Chem. **105**, 447 (2003)

A. A. Tsekouras, M. J. Iedema, J. P. Cowin, Phys. Rev. Lett. **80**, 5798 (1998)

V. Velikov, S. Borick, C. A. Angell, Science **294**, 2335 (2001)

M. S. Warshawsky, M. A. Zondlo, M. A. Tolbert, Geophys. Res. Lett. **26**, 823 (1999)

M. S. Westley, G. A. Baratta, R. A. Baragiola, J. Chem. Phys. **108**, 3321 (1998)

S. C. Wofsy, R. J. Salawitch, J. H. Yatteau, M. B. McElroy, B. W. Gandrud, J. E. Dye, D. Baumgardner, Geo. Res. Lett., **17**, 449 (1990)

L. Xu, P. Kumar, S. V. Buldyrev, S.-H. Chen, P. H. Poole, F. Sciortino, H. E. Stanley, Proc. Nat. Acad. Sci. **102**, 16558 (2005)

Y. Yue, C. A. Angell, Nature **427**, 717 (2004)

Y. Yue, C. A. Angell, Nature **435**, E2 (2005)

Vita

Sean Michael McClure was born in Des Moines, Iowa on August 6, 1979, the son of Michael and Sandra McClure. After graduation from Ankeny High School in Ankeny, Iowa in 1997, he enrolled at The University of Iowa in Iowa City, Iowa. Sean completed his Bachelor of Science in Chemical Engineering degree in May 2001. In August 2001, he entered the Graduate School at The University of Texas at Austin in the Department of Chemical Engineering, working in the Mullins Research Group.

Permanent address:　 9009 Great Hills Trail #2531, Austin, TX 78759

This dissertation was typed by the author.